S T U D I E S I N

N U C L E A R

P H O T O D I S I N T E G R A T I O N

by

K.H. Lokan.

A Thesis submitted to the Australian National University for the degree of Doctor of Philosophy.

April, 1958.

P R E F A C E.

This Thesis is concerned with experimental studies of nuclear photodisintegration, performed with bremsstrahlung radiation from the Canberra 33 Mev electron synchrotron.

Some of the investigations described have been performed in collaboration with other workers. The measurement of photoneutron activation curves reported in Chapter 2 was made in collaboration with Dr. J.H. Carver, and the method of analysis developed jointly. The experiments described in Chapter 4 on the photodisintegration of tantalum were performed jointly by Dr. J.H. Carver, Dr. R.D. Edge and myself, the experimental work being shared equally amongst us. The remaining experiments were carried out independently.

I am greatly indebted to Dr. J.H. Carver, who has supervised most of these investigations, and given me much assistance and helpful advice in the course of this work.

I wish also to acknowledge the assistance of Mr. A. Bull, and particularly his efficient operation of the electron synchrotron.

I am grateful to the Australian National University for the award of a Scholarship, during the tenure of which

these studies were carried out.

Some of the work described in this Thesis has been reported in the following publications:

(i) "Determination of Photonuclear Cross Sections" (with Dr. J.H. Carver). Australian Journal of Physics 10, 312, (1957).

(ii) "The Integrated Cross Section from Threshold to 30 Mev for the Reaction $Be^{9}(\gamma,2n)Be^{7}$". Proc. Phys. Soc. A70, 836, (1957).

(iii) "Direct Excitation in the Photodisintegration of Tantalum above the Giant Resonance" (with Dr. J.H. Carver and Dr. R.D. Edge). Proc. Phys. Soc. A70, 415, (1957).

No part of this Thesis has been submitted for a degree at any other University.

K. M. Lokan

TABLE OF CONTENTS.

		Page
Preface		(i)
	CHAPTER 1.	
	INTRODUCTION.	
1.1	Introduction	1
1.2	Characteristics of Photonuclear Absorption	2
1.2.1	The Giant Resonance	3
1.2.2	Energy and Angular Distributions	5
1.3	Dipole Sum Rules	8
1.4	Theoretical Models	10
1.4.1	The Collective Models	11
1.4.2	The Single Particle Model	13
1.4.3	The Relationship between the Two Models	18
1.5	Conclusions	19
	CHAPTER 2.	
	THE MEASUREMENT OF EXCITATION FUNCTIONS WITH A BREMSSTRAHLUNG BEAM. THE REACTIONS $^{12}C(\gamma,n)$, $^{16}O(\gamma,n)$ AND $^{54}Fe(\gamma,n)$.	
2.1	Introduction	21

2.2	The Bremsstrahlung Spectrum	23
2.2.1	The Thin Target Spectrum	24
2.2.2	Thick Target Corrections	25
2.3	The Solution of the Integral Equation	26
2.4	Monitoring of the Gamma-Ray Flux	29
2.5	The Reactions $C^{12}(\gamma,n)$, $O^{16}(\gamma,n)$ and $Fe^{54}(\gamma,n)$	30
2.5.1	The Canberra Electron Synchrotron	31
2.5.2	Energy Calibration	32
2.5.3	Yield Curves for the Reactions	33
2.5.4	Results	35
2.6	Discussion	36
2.6.1	Carbon	38
2.6.2	Oxygen	38
2.6.3	Iron	38

CHAPTER 3.

THE INTEGRATED CROSS SECTIONS FOR PHOTO-REACTIONS LEADING TO 53.6-DAY Be^{7}. 40

3.1	Introduction	41
3.2	Experimental Method	42
3.3	Results	44
3.4	Discussion	45

3.5 The Reaction $B^{10}(\gamma,t)Be^{7}$ 48

CHAPTER 4.

DIRECT EXCITATION IN THE PHOTODISINTEGRATION OF TANTALUM. 50

4.1 Introduction 51

4.1.1 Photoreactions in Tantalum 53

4.1.2 Neutron Multiplicity 54

4.2 The Single Neutron Yield 56

4.3 The Total Neutron Yield Measurements 57

4.3.1 The Szilard-Chalmers Reaction 57

4.3.2 Experimental Arrangement 59

4.3.3 Extraction of Mn^{56} 60

4.3.4 The Total Neutron Yield Curve 61

4.4 Detection Efficiency as a Function of Neutron Energy 62

4.4.1 The Use of a Larger Tank 62

4.4.2 Detection of $Ta^{181}(\gamma,2n)$ by Residual Activation 63

4.5 The $(\gamma,3n)$ Cross Section 65

4.6 Analysis of the Yield Curves 65

4.7 Discussion 68

CHAPTER 5.

DIRECT PHOTOPROTONS IN THE PHOTODISINTEGRATION OF SILVER. 72

5.1 Introduction 73

5.2 The Proton Detector 75

5.3 Energy Calibration 77

5.4 Experimental Details 78

5.4.1 The Proton Counter 78

5.4.2 Shielding 80

5.4.3 Measures to Reduce Electron Background 81

5.4.4 Experimental Details 84

5.5 Absolute Yields 87

5.6 Results and Analysis 90

5.6.1 Photoproton Yield Curves 90

5.6.2 Analysis of Spectra 92

5.7 Discussion 93

5.7.1 The Proton Evaporation Spectrum 93

5.7.2 The Shell Model 96

5.7.3 Comparison with the Reaction Mo^{100} (γ,p) 100

5.8 Conclusions 101

CHAPTER 6.

THE ANGULAR DISTRIBUTION OF HIGH ENERGY PHOTOPROTONS FROM SILVER. 102

6.1	Introduction	102
6.2	Experimental Details	103
6.3	Angular Distributions	104
6.3.1	The Angular Distribution from Silver	104
6.3.2	The Angular Distribution from Nickel	105
6.4	Discussion	106

APPENDIX 1.

Tables pertaining to the Schiff spectrum. (i)

REFERENCES. (xiii)

CHAPTER 1.

INTRODUCTION.

Abstract.

The experimental results pertaining to nuclear photodisintegration and the giant resonance are summarised. It is pointed out that although most of the observed nucleon emission is characteristic of a decaying compound nucleus, there generally remains a component which is presumed to arise from direct interactions.

The principal theoretical models proposed to account for the absorption are briefly discussed; the relationship between the collective and independent particle model descriptions is indicated, and it is shown that the latter formulation is able to account for the properties of the direct component as far as they are known.

The points at which some of the experiments described in later chapters provide additional information about direct emission and test the predictions of the single particle theory are indicated.

1.1 Introduction.

Early workers (C7, S10, H7) in the field of nuclear photodisintegration were able to establish that energetic

photons were capable of disrupting the nucleus, but it was not until high energy electron accelerators, which provide a continuously variable, albeit complex, spectrum of gamma rays, were developed that the systematics of nuclear photon absorption could be investigated.

1.2 Characteristics of Photonuclear Absorption.

Since gamma rays are strongly scattered and absorbed by the atom through the processes of Compton scattering, pair production and photoejection of electrons, direct absorption methods of examining photon interactions with the nucleus are not very fruitful*. The absorption cross section is generally obtained, therefore, by adding together the cross sections for the reactions (γ,γ'), (γ,n), (γ,np), $(\gamma,2n)$..... etc., which are determined separately by detection of the reaction products or by measuring the radioactivity of the residual nucleus. Measurements are made using a bremsstrahlung beam of the reaction yield as a function of maximum bremsstrahlung energy, and the

---

* Some direct absorption measurements have been made (K8) by determining with a large sodium iodide crystal the shape of a bremsstrahlung spectrum before and after attenuation through an absorber (carbon). When allowance is made for all extranuclear absorption, there remains a small residue at about the right energy to be attributed to the giant resonance.

excitation function for the reaction inferred from the bremsstrahlung yield curve. A method of analysis is described in detail in Chapter 2. With the exception of the lighter nuclei, ($Z \lesssim 30$), most of the total cross section is accounted for by the photoneutron cross sections, since neutrons are not affected by the increasing Coulomb barrier; most of the results quoted below are therefore derived from photoneutron studies.

1.2.1 The Giant Resonance.

Photonuclear absorption takes place largely through a broad resonance, generally from five to six Mev wide in the region from 15 to 20 Mev. The position of the maximum of this "giant resonance" varies smoothly with atomic mass showing an A dependence close to $\hbar\omega \sim A^{-0.2}$, (B3, M6, N1, N2, F6 and others), the width is found to be substantially constant but appears to show significant variation around closed shells (N2, Y1), and the integrated cross section increases with atomic mass, roughly according to the expression:

$$\int \sigma \, dE = 0.020 \; A \; \text{Mev.barn}^{*}$$

---

* when allowance is made for charged particle emission from light nuclei (M2) and photoneutron yields are corrected

Among the light nuclei, careful examination of bremsstrahlung yield curves shows the presence of discontinuities of slope (K3, G3, P2 etc.) and points to the excitation of sharp levels at least near threshold, and there is some evidence of the same sort for fine structure within the resonance itself (P2). Stronger support for this conclusion comes from studies of the energy distribution of reaction products following bremsstrahlung irradiation of light nuclei. For reactions such as $Li^{7}(\gamma,t)$, $C^{12}(\gamma,3\alpha)$ and $O^{16}(\gamma,4\alpha)$ observed in photographic emulsions, the energy of the photon absorbed can be uniquely determined from the energies of the fragments; the difficulty normally encountered in bremsstrahlung experiments of identifying the photon which has induced the reaction is thus overcome, and excitation functions are obtained which display a number of sharp peaks (T2, G7, G5, G6 and others). The same is found for the bremsstrahlung induced photoproton spectra from Be^{9}, C^{12} and O^{16}, where the low excited states

---

for multiplicity (L5). Yergin and Fabricand (Y1) have also found that the integrated cross section to 24 Mev is significantly less for magic nuclei at N = 50. They show that the pronounced sharpening of the resonance is due to a faster fall in the cross section on the high energy side and that this cannot be accounted for by competition, so that the area under the absorption peak is less.

of the residual nucleus are well-separated and transitions to particular states can be resolved. Well-defined photo-proton lines have been observed (C8) reflecting sharp photon absorption in the giant resonance.

At energies well beyond the giant resonance, the cross section is observed to increase slowly (J5), and in this region neutrons and protons are frequently emitted in coincidence (M8). Nucleon emission is strongly angle-dependent, and appears to be consistent with the break-up of a nuclear sub-unit such as a "quasi-deuteron" (L1).

1.2.2 Energy and Angular Distributions.

In light nuclei excited by mono-energetic quanta, the spectrum of emitted nucleons is expected to show well-resolved energy groups as the decay proceeds to different excited states of the residual nucleus, and this is found to be the case (e.g. T3, W7 etc.). In heavier nuclei this structure disappears as the level spacing becomes too small, and the level densities determine the distribution*. It is

---

* Groups arising from transitions to the ground and low excited states persist, however. For example, the energy distribution of photoprotons from A^{40} disintegrated by 17.6 Mev photons shows groups corresponding to transitions to the ground and first excited states of Cl^{39}, superimposed on an "evaporation" spectrum (W7). The same is found, somewhat surprisingly, for photoprotons from iodine. Wright

assumed that a compound nucleus is formed, and the decay proceeds to all states available to it with statistical weighting factors proportional to the level density in the residual nucleus at the energy of the recipient level. The level density increases more or less exponentially, so that a "Maxwellian" distribution of nucleon energies is expected, peaking at a "nuclear temperature" which is characteristic of the residual nucleus after nucleon emission.

Most of the experimental work on the energy and angular distributions of emitted nucleons has been performed using bremsstrahlung as the exciting radiation. When bremsstrahlung is employed, any fine structure is, of course, smeared out by the continuous nature of the photon flux (except in the special cases cited in 1.2.1), but the general shape of the distribution to be expected following the formation of a compound nucleus can still be calculated*. Experimentally it is observed that the

---

and Ophel (W12) have found proton groups corresponding to transitions to the three lowest states of Te^{126} in studies using thin NaI crystals both as target and detector.

* The shape of the evaporation spectrum is not very sensitive to the excitation energy, since the nuclear temperature is a slowly varying function of the energy. Moreover, most of the photon absorption takes place over a fairly narrow

bulk of nucleons are distributed in this way (W7, D4, B12, C10, P3, Z1 etc.) but that there remains in addition a small but significant higher energy component whose presence is not consistent with this description unless the level density is assumed to increase much more slowly (S5; see also 5.7.1 and footnote to page 95), and this in turn throws the lower energy results out of agreement.

The same feature is evident from a study of angular distributions, which show a large isotropic component consistent with emission from a compound nucleus, and a smaller anisotropic group consisting of the high energy nucleons.

Other results which are related to this aspect are the anomalous proton yields from the heavier nuclei, where it is expected that protons will be strongly suppressed by the Coulomb barrier. It is found (H4) that the experimental yield exceeds that calculated from the decay of a compound nucleus by a factor ranging from a few per cent to thousands.

Carver et al (C2) have measured the ratio $\frac{\sigma(\gamma,n)}{\sigma(\gamma,2n)}$ in

---

range of energies, for which the nuclear temperature may be assumed constant (see 5.7.1).

tantalum at 17.6 Mev, and find that the (γ,n) cross section at this energy is too large to be explained by competition in the decay of a compound nucleus; further evidence of the same nature is provided by the experiments described in Chapter 4.

1.3 Dipole Sum Rules.

Basically, the theory of photonuclear reactions is an application of the quantum mechanical theory for the interaction of charged particles with the electromagnetic field*, where it is established that the strongest interactions are the allowed electric dipole transitions. It is therefore anticipated (and this is supported by the magnitude of the cross section : see below) that absorption into the giant resonance is largely electric dipole.

Levinger and Bethe (L4) have made a very general calculation for the integrated cross section for electric dipole absorption by the nucleus, based on the well-known sum rules for the absorption of electromagnetic radiation, and find:

$$\int \sigma \, dE = 0.060 \; NZ/A \; (1 + 0.8x)$$

---

* A neutron may be considered to have an effective charge, because the force on the remainder of the nucleus pushes it away and leaves the neutron free.

where x is the fraction of the neutron proton force which has an exchange character. The first part of this expression is independent of any nuclear model, and the second, whilst it is derived assuming a Fermi gas model, should be fairly insensitive to the model used (L2). Making the good approximation $N \simeq Z \simeq A/2$ and setting $x \simeq \frac{1}{2}$*, one finds that the integrated cross section reduces to:

$$\int \sigma \, dE = 0.020 \; A \text{ Mev-barn}$$

- a result which must agree with any dipole model which takes into account the effect of exchange forces. They show further that the contribution from the higher order multipoles is small compared with the dipole sum (8% for E_2 absorption is the largest).

The experimental cross section agrees with this result, within the rather large experimental errors (see 1.2.1), confirming that the giant resonance is electric dipole in character**.

---

* A value of $x \simeq \frac{1}{2}$ is indicated by other experimental work. It is found, for example, that high energy n-p scattering data are best interpreted if a Serber interaction of the form $V \simeq \frac{1}{2}(1 + P^m)V(r)$, where P^m is the Majorana exchange operator, is assumed.

** A more fundamental calculation due to Gell-Mann et al (G1) which is "model-independent" yields for the TOTAL integrated

1.4 Theoretical Models.

Theoretical accounts of the dipole giant resonance have taken two forms. These are the collective models (G4, J2, D1, D2, B11, F5, S1 and others) in which the process is discussed as a gross dipole oscillation of all protons against all neutrons, and the independent particle model where the interacting photon is considered to be absorbed by a single nucleon in making an E1 transition between shell model states (W5, W6, C9, B10). Both of these treatments give reasonable results for the main features of the giant resonance, even though they appear to be mutually exclusive. This apparent contradiction is partly resolved by Brink (B9), who shows that for an oscillator potential a particular linear combination of single particle transitions is excited which corresponds exactly to one of the collective oscillations proposed by Goldhaber and Teller (G4). This aspect is considered in greater detail in 1.4.3.

---

cross section including all multipoles:

$$\int_0^\infty \sigma \, dE = 0.060 \; NZ/A \left(1 + 0.1 \frac{A^2}{NZ}\right)$$

which is close to the same value.

1.4.1 The Collective Models.

A number of collective modes of oscillation in which all protons move collectively against all neutrons have been proposed by Goldhaber and Teller (G4). In the model which they analyse in detail, for example, the nucleus is considered as two interpenetrating clouds of protons and neutrons which pass back and forth through one another during the oscillation. For this model, which they analyse classically, it is possible to describe the motion in terms of a single collective co-ordinate representing the separation of the respective centres of mass, and to show that for small distortions this co-ordinate undergoes a simple harmonic oscillation. When reasonable assumptions are made for the nuclear parameters involved, a value is obtained for the frequency (i.e. the energy) in fair agreement with experiment, with an A dependence $\hbar\omega \sim A^{-1/6}$. The integrated cross section agrees with the non-exchange component of the dipole sum, as it must do if the model is to account for all of the dipole absorption. The model has been refined by Fujita (F5), who shows that in a proper quantum mechanical analysis* ex-

---

* c.f. Tomonaga (T4) for conditions under which a quantum mechanical analysis in collective co-ordinates is valid.

change effects appear when a velocity-dependent potential is introduced into the Hamiltonian, increasing the integrated cross section and the resonance energy by a factor $(1+\delta x)$ where δ is a number close to 0.8 (c.f. 1.3 above).

There are other modes of collective motion which have been examined (J2, D1, D2, S1) and whose detailed predictions differ from the model just considered, but by and large their results for the position and magnitude of the absorption peak are similar.

It appears, then, that the broad features of nuclear dipole absorption are adequately explained in terms of the excitation of a single level, corresponding to a collective vibration of all protons against all neutrons. However, when the subsequent de-excitation of the state reached is considered the collective picture is less satisfactory. It is assumed that the ordered vibration induced when a photon is absorbed is quickly broken up through random nucleon collisions, leading to the formation of a compound nucleus which decays in the conventional way. We have already seen, however (c.f. 1.2.2), that part of the emission is not consistent with the decay of a compound nucleus; it is therefore considered that these arise from direct interactions. Unfortunately, there does not appear to be any-

thing inherent in the collective level to account for direct emission*, and it is necessary to propose an independent "direct photo-effect" (J1, C9) to explain the observed excess of high energy anisotropic nucleons. This in turn is somewhat unsatisfactory, since the experiments of Ferrero et al (F2) using threshold (n,p) detectors indicate that the anomalous fast neutron component arises from the same absorption mechanism as the lower energy neutrons from a compound nucleus.

1.4.2 The Single Particle Model.

The single particle model has been developed by Wilkinson (W5, W6) and a more detailed account is given of it in this work, since some of the experiments described later are interpreted in terms of single particle excitation.

One starts from a consideration of the matrix element for E1 transitions by individual nucleons between shell model states. Since the giant resonance is known to exhaust the dipole sum, and this involves all the nucleons in the nucleus, it is apparent that most of the transition

---

* but see 1.4.3 where the collective level can be interpreted as a linear combination of single particle states.

strength must be attributed to nucleons in the closed shells, since this is where most of them lie. Wilkinson shows that transitions involving the disruption of closed shells are much stronger than valence transitions, so that, although a single nucleon makes the transition, its strength is considerably enhanced by the presence of the remaining nucleons which close the shell. Transitions from the deep-lying shells are, of course, strictly forbidden, since the shells above them are already filled, but they still contribute to the dipole sum in that their presence prohibits negative transitions downwards from the shells above.

The strongest transitions occur between shells with the same radial quantum number, for the radial overlap integrals $\int \psi^{*}(r)\, r\, \psi(r) dr$, which largely determine the dipole matrix element, are then greatest. Since for all reasonable shell model potentials the separation between these shells is roughly constant, the strong transitions will have approximately the same energy, and the total absorption cross section will show a peak.

In actual fact when the absorption energy is calculated it is found to be too low - Wilkinson finds 9 Mev in lead, where the observed value is 14 Mev - but there

are reasonable arguments whereby it may be increased. If a velocity-dependent potential is used, or what amounts to the same thing, an effective nucleon mass equal to about half of its free mass*, the energy is increased and agrees satisfactorily with experiment. We have already seen that the same considerations enter into the correct calculation for the dipole sum through the factor $(1 + 0.8x)$ (1.3 and 1.4.1) and in the same way the harmonic mean energy, which may not be very different from the position of the maximum, is increased some fifty per cent.

It is interesting to note that the presence of fine structure in the resonance (c.f. 1.2.1) can be readily accounted for, since the theory does not require a greater density of states at the peak, but only that transitions to them should be enhanced.

The important difference between the collective and single particle models is that in the latter we are presented with an excited state, which need not always decay through a compound nucleus. A single nucleon has been elevated to a high energy shell, from whence it may be

---

* c.f. Weisskopf (W2), who suggests that the experimental position for the peak is evidence for an effective mass equal to half the free nucleon mass.

emitted directly, or, as is more frequently the case, be absorbed into a compound nucleus following inelastic collisions with other nucleons. Moreover, we can make an estimate C_ℓ of the relative likelihood of these two processes, where:

$$C_\ell \approx \frac{3\hbar^2 k P_\ell}{2mR} \Big/ 2W$$

The numerator of this expression is the sum rule limit for the particle width for a nucleon of wave number k in a nucleus of radius R (S2), multiplied by the penetrability, and the denominator is the width for absorption into a compound nucleus, equal to twice the imaginary part of the complex potential.

For neutrons, where the penetrability enters only through the centrifugal barrier, and therefore only affects the direct yield from states of very high angular momentum, it can be expected that the cross section for direct emission will display the same giant resonance as the cross section for those which are evaporated; this is in agreement with Ferrero's results (F2; see 1.4.1 above). Ferrero et al find for the fast neutron component from bismuth a cross section shape very close to that of the giant res-

onance, and a direct yield which agrees with that predicted by the decay of single particle states. Similar conclusions can be drawn from the experiments described in Chapter 4.

For protons the situation is likely to be somewhat different, since the additional Coulomb barrier means that the factor P_ℓ largely determines the behaviour of C_ℓ , and consequently the direct yield from each transition. Since the strongest transitions are those between shells of high angular momentum, and the emission of direct protons from these will be strongly inhibited by the barrier (Coulomb + centrifugal), it is likely that most of the direct proton yield will come from the less strong transitions at higher energy, between shells of low angular momentum. In heavy nuclei direct protons must account for virtually all photo-proton emission, since the Coulomb barrier prohibits proton evaporation; this may mean that the peak of the (γ,p) cross section is shifted to higher energies.

Wilkinson finds excellent agreement between the direct photoproton yields calculated on this basis for 23 Mev bremsstrahlung, and the equivalent experimental yields for elements above about Z = 50. He also determines the energy and angular distributions of direct photoprotons from lead, irradiated with 23Mev bremsstrahlung, and finds again that

they agree very well with the experimental distributions.

The single particle theory is seen, therefore, to account for the giant resonance just as successfully as the collective models, and in addition is fairly successful in explaining, through the decay of single particle states, the relative magnitude of the direct component.

The experiments described in Chapters 5 and 6 report measurements made of the absolute yield, excitation function and angular distribution of direct photoprotons from silver, and the results obtained are compared there with the predictions of the single particle theory.

1.4.3 The Relationship Between the Two Models.

The fact that both the collective and single particle descriptions of dipole absorption predict fairly successfully the properties of the giant resonance leads one to suspect that they may in fact represent similar physical situations. Levinger (L3) and Brink (B9) have indicated how this might occur. Levinger suggests that the wave function for the excited state reached in the absorption might be a linear combination of single particle wave functions, which corresponds to all the protons moving in one direction and all the neutrons moving in the other.

Brink in fact shows that in the special case of an

oscillator potential this is indeed so, and [illegible] that a particular linear combination of single particle excitations is produced which corresponds exactly to a Goldhaber-Teller oscillation. Thus one should be able to calculate the direct yield of nucleons from a particular shell, even on the basis of collective excitation, by selecting the appropriate component of the collective wave function which corresponds to that particular single particle transition.

This exact equivalence disappears if the shell model potential is altered, and the Goldhaber-Teller description no longer contains exactly the same information as its single particle counterpart. When a more realistic nuclear potential is assumed, corresponding more closely to a real nucleus, the single particle formulation becomes superior, since the additional information introduced through refinements to the shell model potential is not contained in the collective account.

1.5 Conclusions.

It has been indicated in the foregoing discussion that while the collective and single particle descriptions of nuclear dipole absorption are related, the latter is probably a closer approximation to reality. It has been

shown that the behaviour of the anomalous direct component can be fairly well accounted for when the situation is examined from this point of view, even though the shell model which was used for this purpose is a somewhat idealised one. It might be hoped that as more detailed information about the direct component is accumulated the shells involved in the transitions might be identified, and specific details about the nuclear potential inferred.

CHAPTER 2.

THE MEASUREMENT OF EXCITATION FUNCTIONS WITH A BREMSSTRAHLUNG BEAM. THE REACTIONS $C^{12}(\gamma,n)$, $O^{16}(\gamma,n)$ AND $Fe^{54}(\gamma,n)$.

Abstract.

The problem of measuring photon excitation functions with the rather awkward bremsstrahlung distribution is discussed. An iterative method for the solution of bremsstrahlung yield curves to obtain excitation functions is presented, and the relevant tables for such solution appended.

The measurement by residual activation of the yield curves for the reactions $C^{12}(\gamma,n)$, $O^{16}(\gamma,n)$ and $Fe^{54}(\gamma,n)$ from their thresholds to 31 Mev is described, and the iterative method applied to derive the excitation functions. These show certain interesting features which are discussed.

2.1 Introduction.

Although synchrotrons and betatrons deliver high fluxes of gamma rays, and indeed have made possible the systematic study of photonuclear reactions, which have such low cross sections, they suffer from the major drawback that the gamma rays are not mono-energetic. This complicates the analysis greatly, for, while it is very easy to induce and

detect photonuclear effects with such sources, it is necessary to disentangle from the observations the effect of having a continuous distribution of photon energies. However, provided that this distribution is known, it is possible to measure excitation functions for such reactions.

Unfortunately, the bremsstrahlung distribution can rarely be precisely specified, since even though the radiation process is fairly well understood the radiating conditions within most machines are not well-defined. However, to within a few per cent the photon spectrum is known, and this is adequate to examine the broader features of photonuclear absorption, such as the giant resonance. Indeed, in certain favourable circumstances, detailed structure within the resonance can be inferred (K3, G3, P2 etc.; see 1.2.1).

To measure the excitation function for a photonuclear reaction the reaction yield $A(k_0)$ is measured as a function of the energy k_0 of the radiating electrons. This is related to the cross section $\sigma(k)$ and the bremsstrahlung distribution $P(k,k_0)$ by the expression:

$$A(k_0) = g \int_T^{k_0} \sigma(k)\, P(k,k_0)\, dk \qquad \ldots.(2.1)$$

where k is the energy of the photon and g is a constant which normalises the expression to unit electron charge.

The problem then reduces to solving this integral equation, given $A(k_0)$ and $P(k,k_0)$, and this has been done in a number of ways (W10, J4, K2, S3). The best-known of these is the "photon difference" method (K2) where the integral is replaced by a sum over a set of narrow intervals and an average cross section for each interval is obtained. This is not, however, the method used in this work; an analytical method is developed in which the integral is transformed into a form amenable to iterative solution, with the aid of certain functions which are tabulated.

2.2 The Bremsstrahlung Spectrum.

The bremsstrahlung arising from fast electrons incident upon a thin radiator is fairly well understood, and has been calculated by Bethe and Heitler (H3). This calculation makes use of the Born approximation, which requires that the quantity Ze/137v should be small compared with unity. For radiators of high atomic number this condition is not at all well fulfilled, but more exact calculations (B6, M4) using proper Coulomb wave functions indicate that the chief error introduced lies in the ab-

solute magnitude of the bremsstrahlung cross section rather than in the shape. The Bethe-Heitler equations, suitably modified by these considerations, have been checked experimentally through the inverse process of pair production (see D3), as has the bremsstrahlung cross section itself (W1, K7) though not to such accuracy, and it is safe to say that the theoretical spectrum applies quite well for thin radiators, even of high Z.

2.2.1 The Thin Target Spectrum.

In the form given by Schiff (S6) the intensity in the forward direction $J(k,k_0)$ in units of energy is proportional to:

$$\Gamma = \left\{1 + (1-z)^2\right\} 2\log_e \alpha - (2-z)^2 \quad \ldots.(2.2)$$

where $z = k / k_0 + u$ and $1 / \alpha^2 = 1 / \alpha_1^2 + 1 / \alpha_2^2$, with:

$$\alpha_1^2 = 2(k_0 + u)(1-z) / uz \quad \text{and} \quad \alpha_2^2 = C / Z^{1/3}$$

and:

k = photon energy in Mev
k_0 = electron energy in Mev
u = rest mass of electron in Mev = 1.02
C = constant = 111.

Then $P(k,k_0)$, the number of photons of energy k, is given by:

$$P(k,k_0) = J(k,k_0) / k.$$

The derivative of $P(k,k_0)$ with respect to k_0 is also required in the analysis which follows, and is:

$$P'(k,k_0) = dP / dk_0$$

$$= \frac{2}{(k_0+u)k}\left\{2z(1-z)\log_e\alpha + \frac{(z-2)(2-z)z}{1-z}(1-\alpha^2/\alpha_2^2)(1+[1-z]^2)\right\} \quad ..(2.3)$$

2.2.2 Thick Target Corrections.

The difficulty lies in relating this thin target result to the more realistic case of electrons striking a thick target, where ionisation losses and multiple scattering within the radiator are certain to produce some modification. Apart from the case of machines with external beams, where the radiator conditions can be chosen at will, and thick target corrections consequently applied (W9), the target parameters are generally not well-known.

Since no sensible corrections for target thickness can be applied for the Canberra machine, it is assumed in the following that the intensity in the forward direction is given by the Bethe-Heitler expression (2.2). There is partial justification for this assumption in that electrons which are strongly scattered within the target will radiate at a lower energy, but not in the forward direction. Those experiments which have been performed to measure the dis-

tribution in comparable situations (W1, K7 etc.) indicate that there is not a great deal of error introduced by this assumption, and that the Bethe-Heitler calculations do approximately represent the experimental distribution.

2.3 The Solution of the Integral Equation.

According to equation (2.1), the reaction yield is given by:

$$A(k_0) = g \int_T^{k_0} \sigma(k)\, P(k,k_0)\,dk.$$

Differentiating with respect to k_0:

$$A'(k_0)/g = \int_T^{k_0} \sigma(k) P'(k,k_0)\,dk + \sigma(k_0) P(k_0,k_0)$$

or:

$$A'(k_0)/g = \int_T^{k_0} \left\{\sigma(k) - \sigma(k_0)\right\} P'(k,k_0)\,dk + \sigma(k_0)\left\{P(k_0,k_0) + \int_T^{k_0} P'(k,k_0)\,dk\right\}.$$

This becomes, on rearranging:

$$\sigma(k_0) = \sigma_0(k_0) + \frac{1}{S(k_0,T)} \int_T^{k_0} \left\{\sigma(k) - \sigma(k_0)\right\} P'(k,k_0)\,dk \qquad \ldots.(2.4)$$

where:

$$S(k_0,T) = P(k_0,k_0) + \int_T^{k_0} P'(k,k_0)\,dk \qquad \ldots.(2.5)$$

and:

$$\sigma_0(k_0) = A'(k_0) / gS(k_0,T) \qquad ....(2.6)$$

The iterations are made on equation (2.4), by inserting in the integral the zero order approximation $\sigma_0(k_0)$ to compute a correction $\sigma_1(k_0)$ which is then inserted in turn in the integral to compute a second order correction, and so on. In general form the complete solution is:

$$\sigma(k_0) = \sum_{n=0}^{n=\infty} \sigma_n(k_0) \qquad ....(2.7)$$

with:

$$\sigma_n(k_0) = \frac{1}{S(k_0,T)} \cdot \int_T^{k_0} \left\{ \sigma_{n-1}(k_0) - \sigma_{n-1}(k) \right\} P'(k,k_0)dk$$

where $\sigma_0(k_0)$ and $S(k_0,T)$ are given by equations (2.6) and (2.5).

In principle, it would be possible to solve this equation with a single set of values of $S(k_0,T)$ computed for a value of T below the threshold of all reactions to be considered, but the convergence of the iterations is greatly improved by choosing T as close to the threshold as possible. Tables of values of $P(k,k_0)$, $P'(k,k_0)$ and $S(k_0,T)$ have been computed at 1 Mev intervals of each variable over the range 6 - 35 Mev, and are appended at the end of this thesis (Appendix 1).

It is interesting to note that if the bremsstrahlung intensity were constant, so that $P'(k,k_0) = \delta(k-k_0) / k$, the zero order approximation (2.6) would be exact. In Figure 2.1 $P'(k,k_0)$ is plotted as a function of k for increasing values of k_0, and it is noticeable that, as k_0 increases, the derivative draws closer to a delta function. This is reflected in the fact that the iterations do indeed converge more sharply the higher the threshold for the reaction.

The procedure for analysing bremsstrahlung yield curves by this method is then the following:

(i) the measured yield curve is numerically differentiated and normalised by the function $S(k_0,T)$ to give the zero order approximation $\sigma_0(k_0)$

(ii) using equation (2.4), improved solutions are obtained with the aid of the tabulated values of $P'(k,k_0)$ and $S(k_0,T)$; the computation of the integral in equation (2.4) is carried out by any of the standard numerical methods.

Figure 2.2 shows an example of such an analysis. The cross section for the reaction ^{63}Cu (γ,n) as measured by Berman and Brown (B5) was assumed, and from it a yield curve was constructed using the Schiff spectrum (Appendix 1,

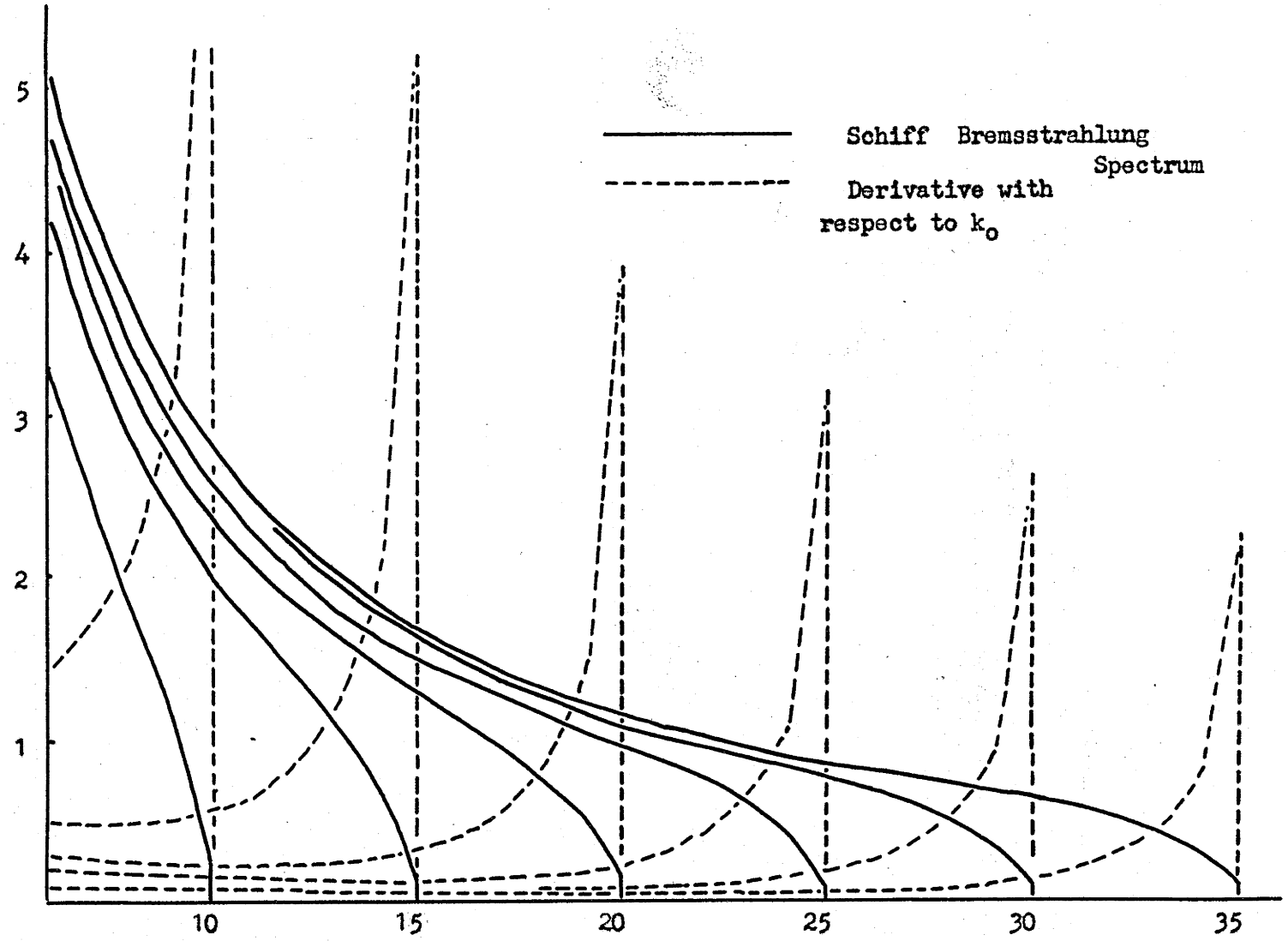
Schiff Bremsstrahlung Spectrum
Derivative with respect to k_o
5
4
3
2
1
10
15
20
25
30
35
Energy in Mev.

Figure 2.1

Table 1). This was analysed by the iterative method just described, and the solution, converging to the original shape as more approximations were taken, is shown.

2.4 Monitoring of the Gamma-Ray Flux.

The measurement of bremsstrahlung intensities and total flux is generally a difficult problem. The most satisfactory method of monitoring is to measure the integrated electron current which produces the bremsstrahlung, but this is not feasible for machines which have internal circulating beams. A popular alternative is to measure the total ionisation produced by the beam in a standard thick-walled ionisation chamber (K2), but this method suffers from the defect that the response of the chamber has to be calculated as a function of maximum bremsstrahlung energy, and such calculations are not very reliable.

This difficulty may be avoided by measuring yields relative to some other well-established reaction. This is the practice adopted in this work, where the cross section measurement of Berman and Brown for the reaction ^{63}Cu (γ,n) is taken as standard. Their measurement was monitored directly by collecting and measuring the total electron charge which gave rise to the bremsstrahlung and the bremsstrahlung itself was properly corrected for target thick-

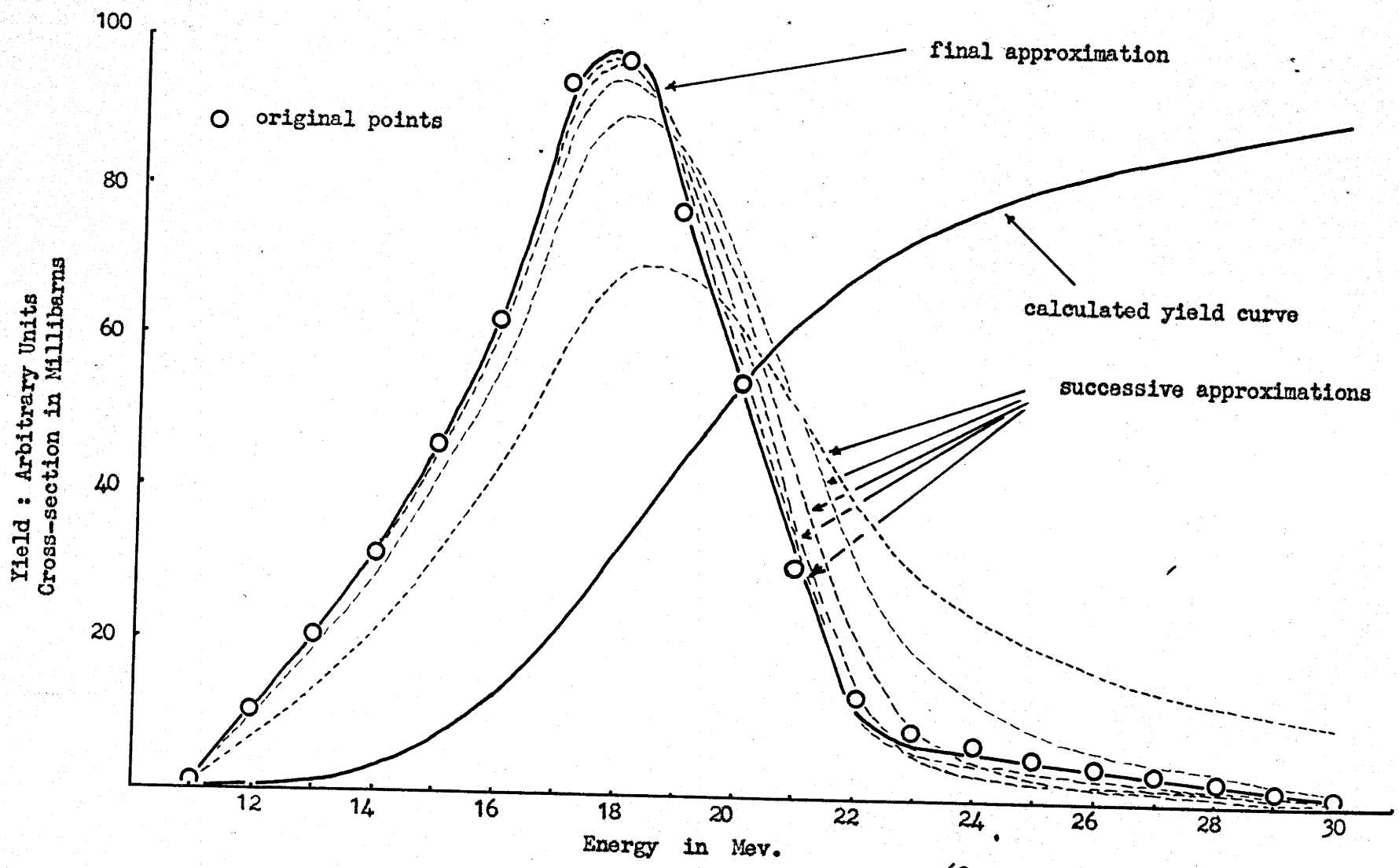

Figure 2.2 : Analysis of calculated $Cu^{63}(\gamma,n)$ yield curve

ness, so that considerable reliance can be placed on their result. From their published excitation function a yield curve has been computed assuming the Schiff thin-target spectrum, and this "theoretical" yield curve is subsequently taken as standard (Fig. 2.2).

Experimentally, the yields from the reaction under study and from the reaction Cu^{63} (γ,n) are measured simultaneously as a function of maximum bremsstrahlung energy. The ratio of these, and the assumption of the above yield curve for copper, then gives directly the required yield, normalised to unit electron charge. Moreover, this procedure compensates in part for any inadequacies in the assumed bremsstrahlung shape and for the neglect of thick-target corrections (c.f. Sagane; S3). For those reactions at least whose excitation functions have shapes similar to that of copper, this form of monitoring will give the correct result for the derived cross section; fortunately, the (γ,n) reaction in copper is fairly typical, and this condition is met approximately in a large number of cases.

2.5 The Reactions C^{12} (γ,n), O^{16} (γ,n) and Fe^{54} (γ,n).

The measurement of the photoneutron excitation functions for the isotopes C^{12}, O^{16} and Fe^{54} was undertaken for a number of reasons. Although the three reactions had

been in part measured before (B4, H1, S4, K4), the energy range 24 - 30 Mev had not been thoroughly investigated, and it was felt that in view of the neutron structure of these isotopes - they all have closed shells or sub-shells for neutrons - interesting effects might be observed on the high energy side of the giant resonance. At the same time, satisfactory reproduction of well-known results up to 24 Mev would give confidence in the energy calibration, monitoring procedure and general technique employed, in preparation for more elaborate studies with a bremsstrahlung beam.

2.5.1 The Canberra Electron Synchrotron.

The Canberra electron synchrotron is a mains frequency (50 c.p.s.) machine with a nominal maximum energy of 33 Mev. Energy control is achieved by varying the peak amplitude of the magnetic field and adjusting the duration of the radio-frequency acceleration so that the electrons strike the tungsten target at the peak of the cycle. This amplitude is controlled by a variable inductance choke in parallel with the resonant magnet-condenser circuit, and is stabilised with the choke against drifts of more than 0.25 Mev. The beam intensity is approximately 5 - 7 roentgens per minute at a metre at an energy of 30 Mev, and is somewhat less at lower energies.

2.5.2 Energy Calibration.

The electron energy was determined as a function of magnet current by measuring the thresholds for the photoneutron reactions listed in Table 2.1.

Table 2.1.

THRESHOLD ENERGIES FOR PHOTONEUTRON REACTIONS.

Reaction	Energy
$^{181}_{63}Ta(\gamma,n)$	7.6 Mev
$^{}_{}Cu(\gamma,n)$	10.6 Mev
$^{16}_{8}O(\gamma,n)$	15.6 Mev
$^{12}_{6}C(\gamma,n)$	18.7 Mev

The relationship between energy and magnet current was assumed to remain linear beyond the range of threshold measurements and the calibration determined is in close agreement with that quoted at three energies (18, 24 and 30 Mev) by the manufacturers of the magnet. An additional secondary check is afforded by the measured ratio between the yields from the reactions $^{12}_{6}C(\gamma,n)$ and $^{63}_{}Cu(\gamma,n)$ as a function of energy. This agrees precisely with the same measurement on the Stanford linear accelerator (B4, B5),

where the energy was measured independently by a magnetic deflection method.

It is believed therefore with some confidence that the energy calibration is known to within 0.3 Mev, and that, for a given setting, the energy can be held to within 0.25 Mev of its nominal value.

2.5.3 Yield Curves for the Reactions.

A cadmium holder, necessary to obviate unwanted slow neutron reactions, containing a disc of iron, oxygen (as boric acid) or carbon (graphite) sandwiched between similar copper discs, was exposed to the synchrotron beam for a known time. The induced positron activities from the reaction under study and from the copper were measured with thin-window Geiger counters (Twentieth Century: Type EW.3H) in a standard geometry, and the ratio of the activities determined as a function of maximum bremsstrahlung energy.

The length of the irradiations was chosen to suit both the half-life of the isotope being produced and the half-life of the activity induced in the copper monitor foils (9.4 minutes). Thus, for carbon and iron, with half-lives of 20.4 minutes and 8.9 minutes respectively, the targets were exposed for ten minutes, whilst oxygen

(half-life 2.1 minutes) was exposed for two minutes.

Since counting rates were quite high, it was necessary to determine dead time corrections for the Geiger counters. A copper disc was irradiated to saturation, and the decay of the induced positron activity was followed at two-minute intervals for some ninety minutes. A semi-log plot of count rate versus time showed, after subtracting a small contribution for a 3.3-hour activity induced in Cu^{66}, a pure 9.4-minute half-life for count rates below 40,000 counts per minute. Accordingly, activities were kept below about 30,000 counts per minute so that no dead time corrections had to be applied.

It was found from the activities of the front and back copper foils that no correction was necessary for attenuation of the beam as it passed through the sample.

The activities were corrected for self-absorption using the expression:

$$N = N(\text{observed}) \frac{(1 - e^{-kx})}{kx}$$

where x is the source thickness in mg./sq.cm. and k is the electron (positron) mass absorption coefficient. Values of k appropriate to the positron end-point energy for each isotope were obtained from the published curve of Baker and

Katz (B2). No geometric corrections were necessary, since all samples were of the same size (7/8" diameter) and were counted in a standard position. The data were finally corrected for isotopic abundances, and reduced to "yield per mole of X per yield per mole of Cu^{63}" as a function of maximum bremsstrahlung energy. This was converted to a bremsstrahlung yield curve in each case with the aid of the copper yield curve of Figure 2.2.

The masses, isotopic abundances and positron end-point energies for each isotope are listed in Table 2.2.

Table 2.2.

ISOTOPIC ABUNDANCES AND DECAY SCHEMES.

Target	Thickness (mg./sq.cm.)	Isotopic Abundance *	Half-life (mins.) **	Positron Energy (Mev) **
C^{12}	279	98.9%	20.4	0.91
O^{16}	173	99.8%	2.1	1.68
Cu^{63}	288	69.1%	9.4	2.91
Fe^{54}	102	5.84%	8.9	2.50 (70%) and 2.13 (30%)

* (H5) ** (D5)

2.5.4 Results.

The three yield curves, shown in Figures 2.3, 2.4 and

2.5, were analysed by the iterative method, and the resultant excitation functions are displayed on the same figures. Parameters estimated from the measured excitation functions are presented in Table 2.3.

Table 2.3.

PARAMETERS OF THE MEASURED (γ,n) CROSS SECTIONS.

Reaction	Peak Energy (Mev)	Width at half maximum (Mev)	Integrated Cross Section to 31 Mev (Mev-millibarn)
$C^{12}(\gamma,n)$	23	4.2	42 ± 7
$O^{16}(\gamma,n)$	24	3.4	46 ± 7
$Fe^{54}(\gamma,n)$	19	6.9	290 ± 50

2.6 Discussion.

The derived cross sections agree substantially with earlier measurements as far as they have been made. The excitation functions for $C^{12}(\gamma,n)$ and $O^{16}(\gamma,n)$ show the sharp resonance generally associated with closed shells (c.f. 1.2.1) though this is not apparent for $Fe^{54}(\gamma,n)$, and all three have pronounced high energy "tails". These tails are no doubt partly due to the fact that the $(\gamma,2n)$ thresholds are high for these isotopes (34, 29 and 26 Mev respect-

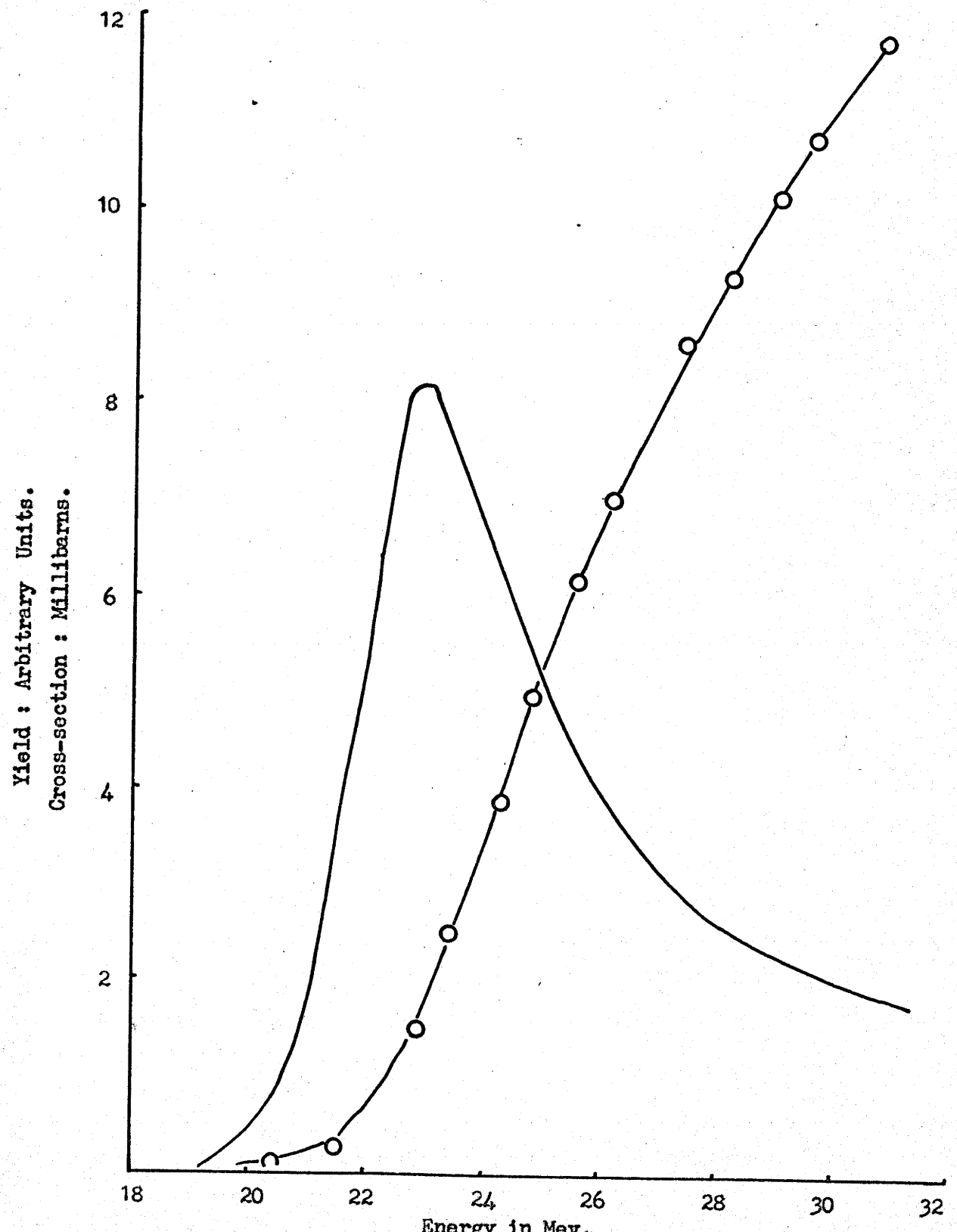

Figure 2.3 : $C^{12}(\gamma, n)$

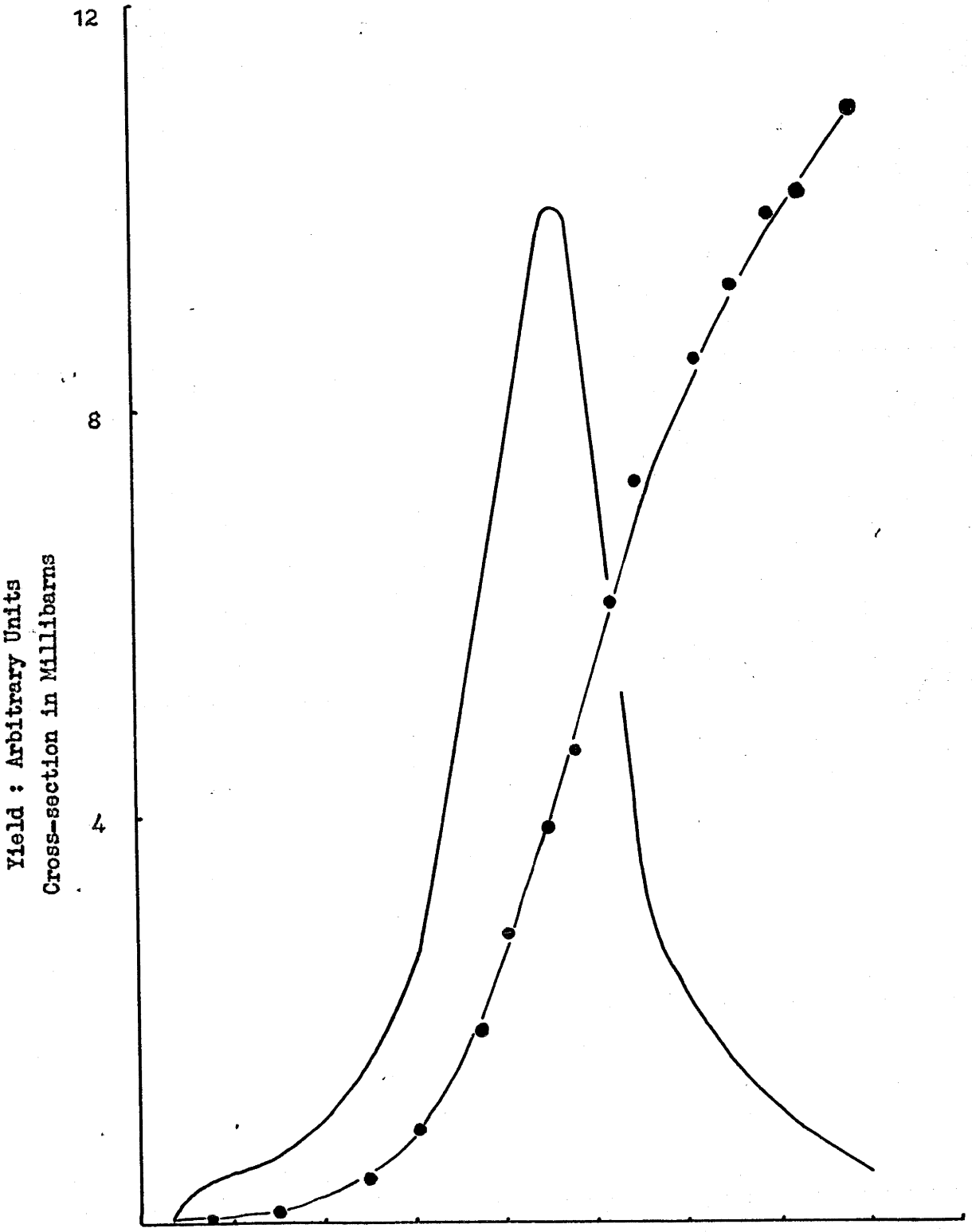

Figure 2.4 : $O^{16}(\gamma,n)$

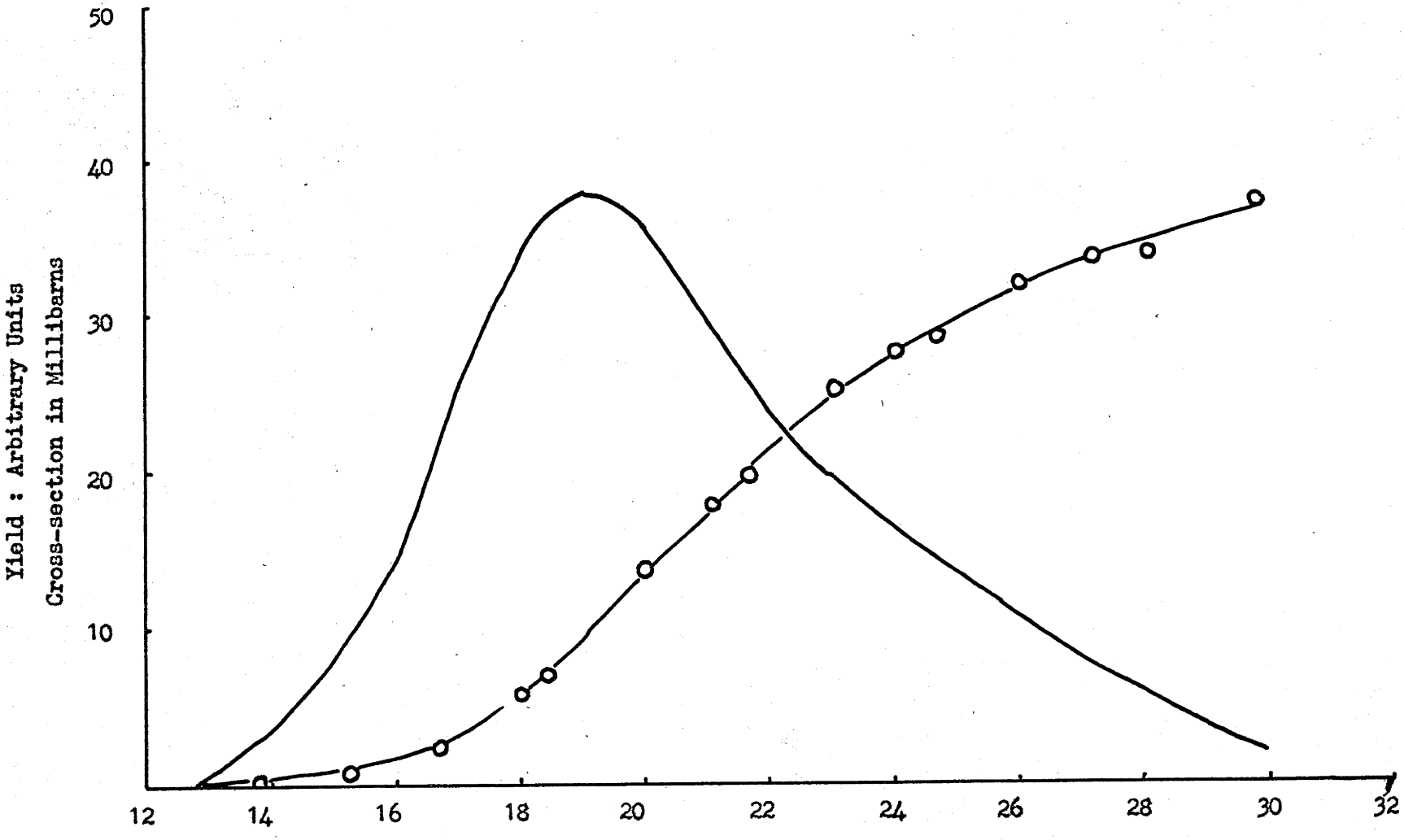

Figure 2.5 : Fe^{54} (, n)

ively: Al and Cu) so that competition from this reaction, which frequently reduces the (γ,n) yield, is not possible over most of the energy range. It is also possible that they may be associated with the closed shells, though it is difficult to envisage the mechanism which would be responsible. This association is suggested by the dipole sum rule for the integrated cross section, since, if the total absorption is to achieve the sum rule limit, and the area under the peak is less (Y1: c.f. footnote to p. 4), the balance of the cross section must appear at higher energies.

It appears that this correlation with the closed shells may be fairly general. Recently Carver and Turchinetz (C11) have measured photoneutron cross sections for a number of elements in the region of N = 82, and find that the cross section shows the same anomalous feature of considerable absorption above the peak for nuclei with N = 82.

The tails in C^{12} (γ,n) and O^{16} (γ,n) have also been reported by Sagane (S4), who interprets them as possible evidence for direct interactions. At higher energies, where competition from multiple reactions becomes more important, this is almost certainly the case, but for photon excitations up to 30 Mev such an inference cannot definitely be drawn.

2.6.1 Carbon.

The measured cross section for carbon agrees closely, both in shape and absolute magnitude, with the results of Barber et al (B4), who report that the high energy tail extends beyond 40 Mev.

2.6.2 Oxygen.

This measurement carries beyond 24 Mev the cross section determination of Horsley et al and Montalbetti et al (H6 and M5). The peak is found to be at 24 Mev rather than at 23 Mev as some earlier results suggest, and is fairly well-determined, since the activation curve was extended well beyond the point of inflection.

The shoulder between 16 and 20 Mev (H6) is well-reproduced. This has been associated with quadrupole absorption (H6: c.f. B8) but Peaslee (P1) has indicated that it can alternatively be explained in terms of incoherent El absorption in this region, as distinct from the largely coherent dipole absorption in the giant resonance.

2.6.3 Iron.

The threshold for the reaction was observed at ~ 12.5 Mev, which is lower than the earlier value of 13.8 Mev (K4). The shape of the cross section is rather unexpected,

since the narrowed absorption frequently found at the magic numbers is not evident, and the absorption is particularly broad.

CHAPTER 3.

THE INTEGRATED CROSS SECTIONS FOR PHOTOREACTIONS LEADING TO 53.6-DAY Be^{7}.

Abstract.

The yield of Be^{7} from the reaction $Be^{9}(\gamma,2n)Be^{7}$, irradiated with 30 Mev bremsstrahlung, has been measured by residual activation. This is converted to an integrated cross section by assuming a reasonable cross section shape, and a value is obtained of:

$$\int_{20.56}^{30} \sigma(\gamma,2n)dE = 1.2 \pm 0.2 \text{ Mev-millibarns}$$

This value is compared with the photoneutron yield measurements of Jones and Terwilliger, and shown to be consistent with the cross section calculated from their result on the basis of competition between the (γ,n) and $(\gamma,2n)$ reactions.

A search has been made for the same activity from the reaction $B^{10}(\gamma,t)Be^{7}$, and an upper limit of 7 Mev millibarns is placed on the cross section for that reaction.

3.1 Introduction.

Photoneutron emission from Be^{9} has been studied extensively at low energies (S8, E1, C4 and others) using radiation from nuclear reactions and radioactive sources, since the neutron binding energy is very low (1.67 Mev: A1). A reasonable theoretical fit to the low energy cross section is found for a model consisting of a loosely bound neutron moving in the field of two alpha particles (G8). The agreement is by no means complete (c.f. the results of Carver et al (C4) which indicate that at 6.13 Mev the break-up sometimes occurs by way of $He^{4} + He^{5}$, the latter then emitting a neutron) but the model appears to explain at least part of the process, and, in particular, predicts the sharp peak in the cross section which is observed just above threshold (c.f. G8).

At higher energies the cross section shows the familiar giant resonance (N3, J5), peaking at 22 Mev, with the same form as the (γ,p) cross section (H2), and presumably involves transitions by the more tightly bound nucleons in the core. It is therefore interesting to look at the $(\gamma,2n)$ cross section, since the emission of two neutrons must also be associated with the latter process. The threshold for this reaction is 20.56 Mev (from mass

values: Al) and the product nucleus Be^{7} has a half-life of 53.6 days, so that the reaction should be amenable to a residual activation measurement.

3.2 Experimental Method.

Be^{7} decays by K-capture to the ground and first excited states of Li^{7}, with 11 per cent of the transitions going to the higher state at 477 Kev (Al). This decays by the emission of a gamma ray; the method therefore chosen to measure the Be^{7} activity was pulse height analysis of its gamma-ray spectrum, detected with a sodium iodide crystal and photomultiplier.

A cubic block of beryllium metal of dimensions 1" x 1" x 1" and weighing 29.57 grammes was irradiated for a total of sixteen hours in a bremsstrahlung beam with a maximum bremsstrahlung energy of 30 Mev. The beam was monitored with 1" x 1" x 0.005" tantalum foils through the 8.15-hour beta activity induced in them through the reaction $Ta^{181}(\gamma,n)Ta^{180m}$, tantalum being chosen for its convenient half-life. The irradiation was broken into three parts, each of about five hours' duration, and for each, fresh monitor foils were taken. As a precaution against possible neutron capture reactions, since the machine generates a considerable flux of thermal

neutrons, the block and monitor foils were enclosed in cadmium foil.

Gamma rays from the beryllium block were detected with a 2" NaI(Tl) crystal and photomultiplier enclosed in a lead castle with 3" walls. Pulses from the photomultiplier were analysed with a Hutchison-Scarrot multi-channel analyser, and a typical spectrum is plotted in Figure 3.1. The gamma ray from the decay of Be^{7} was readily detected, with a measured energy of 475 ± 5 Kev, and its half-life, which was followed for ninety days, was confirmed to be 53 ± 3 days. The observed counting rate in the photopeak, when a background of 9.0 counts per minute was subtracted, was 9.6 counts per minute.

The activity induced in the tantalum monitor foils was measured with the standard beta-sensitive Geiger counters used in the previous experiments (see 2.5.3). Counting rates of the order of 12,000 counts per minute were recorded, and the half-life of each foil was checked and found to be as expected.

Since the Cu^{63} (γ,n) Cu^{62} cross section is taken as standard in this work, a separate short irradiation was made of 1" x 1" copper and tantalum foils, and their induced activities compared to derive a figure for the ac-

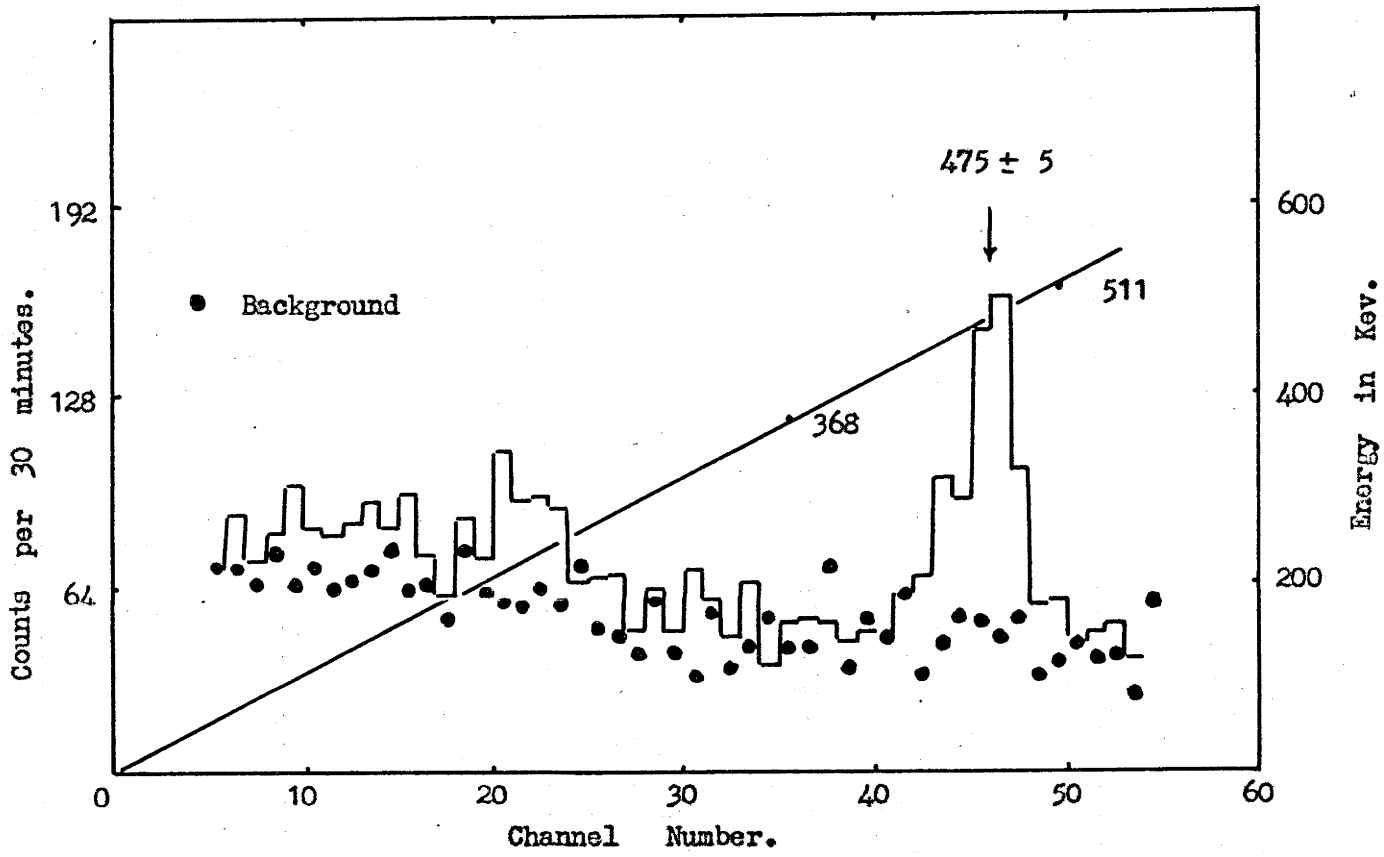

Figure 3.1 : Energy of Gamma-ray from Be^7.

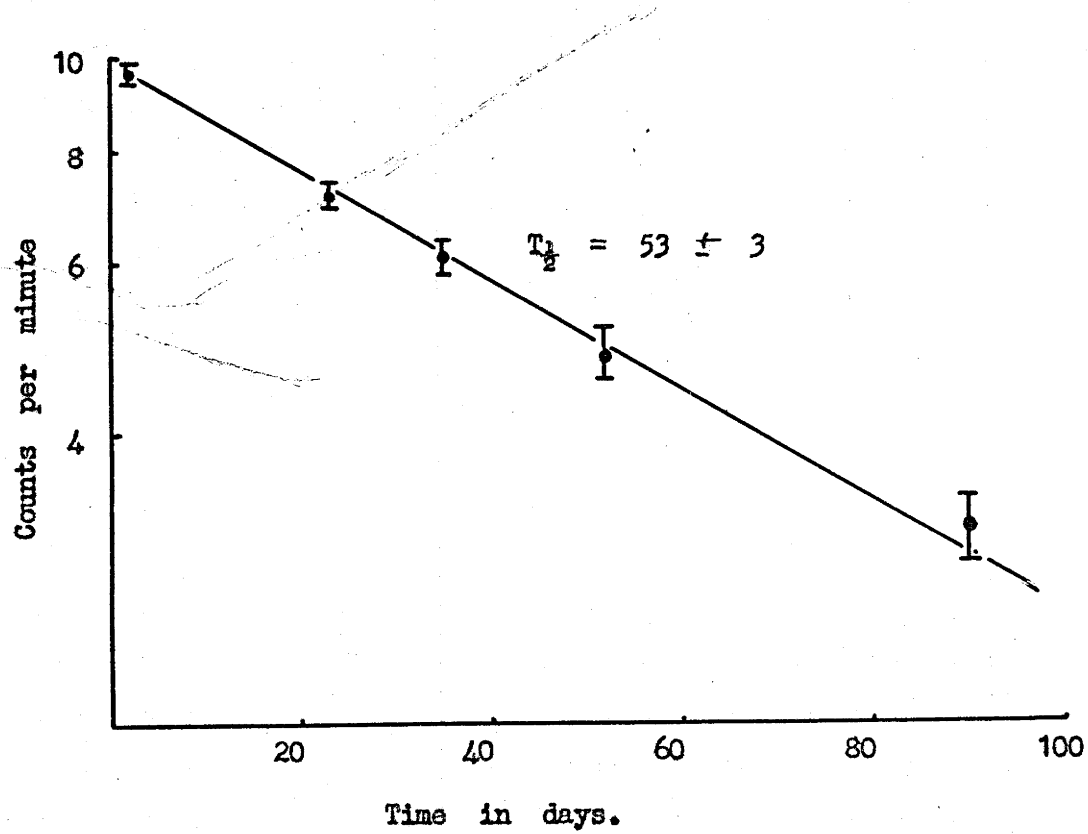

Figure 3.2 : Half-life of Be^7 activity

tivity which would have been induced in copper in the long irradiations. Copper could not be used as the initial monitor, as its half-life is much too short.

Annihilation radiation from the Cu^{62} was also detected with the scintillation counter, so that ultimately the yields of Be^{7} and Cu^{62} were compared in similar geometries with the same detector.

3.3 Results.

The observed activities were corrected to saturated activities per mole of each isotope; small corrections were made to allow for self-absorption of the 477 Kev radiation within the beryllium block (19%: S7) and for the slightly different geometries of the block and foils in the scintillation detector. This latter correction was small (12%) since both were placed at a distance of about 2" from the crystal, so that to a first approximation the geometric efficiency was the same for each.

A ratio was obtained for the relative yields at 30 Mev of:

$$\frac{\text{Yield of } Be^{7} \text{ per mole of } Be^{9}}{\text{Yield of } Cu^{62} \text{ per mole of } Cu^{63}} = (2.56 \pm 0.51) \times 10^{-3}$$

In order to convert this to an integrated cross

section, it is necessary to assume a shape for the cross-section curve, since the experiment has determined only one point, at 30 Mev, on the bremsstrahlung yield curve. It transpires that the integrated cross section is not very sensitive to the shape assumed*, and the integrated cross section derived for an excitation function peaking at 24 Mev is:

$$\int_{20.56}^{30} \sigma(\gamma,2n)\, dE = 1.2 \pm 0.2 \text{ Mev millibarn.}$$

3.4 Discussion.

An estimate of the $(\gamma,2n)$ cross section can be made if the process is thought of from the following point of view. A neutron is emitted from the excited Be^{9} nucleus, leaving Be^{8} in an excited state. If sufficient energy is left in the residual nucleus for the emission of a second neutron to be possible, the probability of this occuring

---

* To check this point excitation functions, six Mev wide and peaking at 22, 24, 26 and 28 Mev, were assumed, and the integrated cross section derived in each case. The values obtained were 1.14, 1.17, 1.34 and 1.53 Mev millibarn respectively. It is easy to see that this will be so, since except at the high energy tip of the bremsstrahlung the photon distribution does not change very quickly over the range 20 to 30 Mev.

is determined by:

(i) the relative likelihood that the first neutron leaves Be^{8} in a state above the threshold for further neutron emission

(ii) the competition between neutron emission and all other modes of decay of the excited Be^{8}.

Equivalent excitations in Be^{8} are reached by the reaction Li^{6} + d (Al), so that (ii) may be estimated from the experimental cross sections for the reactions Li^{6} (d,γ) (Al), Li^{6} (d,d) (Al), Li^{6} (d,p) (W3), Li^{6} (d,t) (M1), Li^{6} (d,α) (W3) and Li^{6} (d,n) (B1). From the measured cross sections for these reactions it is found that, for this order of excitation, about 40 per cent of decays proceed by way of neutron emission to Be^{7}.

The factor (i) is estimated roughly, using for the energy distribution of the first neutron, the expression $I(\varepsilon)d\varepsilon \sim \sigma_C \omega(E_R)$, where ε = neutron energy in Mev, σ_C = cross section for the formation of a compound nucleus in the inverse neutron capture reaction and $\omega(E_R)$ = level density in the residual nucleus at the excitation left to it. σ_C is given by Blatt and Weisskopf (B8, p.348) assuming that there are no selection rules to take into account.

$\omega(E_R)$ is estimated below 20 Mev from the known distribution of levels in Be^8 (Al), and beyond this energy by assuming a level density of the form $\omega(E_R) = 0.05 \exp(0.86E_R)^{\frac{1}{2}}$ Mev^{-1} which gives the correct number of levels below 20 Mev and fits approximately the known level spacing. Using this form for the level density, and the estimate that 40 per cent of decays above the neutron threshold in Be^8 lead to Be^7, the percentage of neutron transitions which are expected to lead to a second neutron are listed as a function of photon energy in Table 3.1.

Table 3.1.

Photon energy	20.56	22	24	26	28	30
Percentage	0	1	5	12	25	40

It must be emphasised, however, that this calculation may be considerably in error, since the statistical assumptions implicit in the use of an exponential level density are not well-founded in a nucleus as light as beryllium.

Using the values listed in Table 3.1, the total photoneutron yield measurements of Jones and Terwilliger (J5) have been corrected for neutron multiplicity, and the cross

section for the emission of two neutrons calculated. The curve of Jones and Terwilliger, the corrected (γ,n) cross section and the calculated $(\gamma,2n)$ cross section are shown in Figure 3.3*. The value obtained in this way for the integrated $(\gamma,2n)$ cross section is 1.8 Mev millibarn, which is in surprisingly close agreement with the direct measurement described above.

3.5 The Reaction $B^{10}(\gamma,t)Be^{7}$.

A search was also made for the Be^{7} activity following a similar irradiation of boron, since the threshold for the reaction $B^{10}(\gamma,t)Be^{7}$ is 18.6 Mev (from mass values: Al). A block of solid boron was made by binding amorphous boron powder with a small quantity (1%) of paraffin dissolved in acetone, and subjecting it to a pressure of 10 tons per sq. inch in a cylindrical former. The mass of boron consolidated in this way in a cylindrical pellet of 1" diameter and approximately 1" long was 12.2 grammes; this was irradiated under the same conditions and for the same length of time as the beryllium.

No radiation was found corresponding to Be^{7} disintegra-

---

* For simplicity, the contribution of the (γ,np) reaction to the total neutron yield has been neglected.

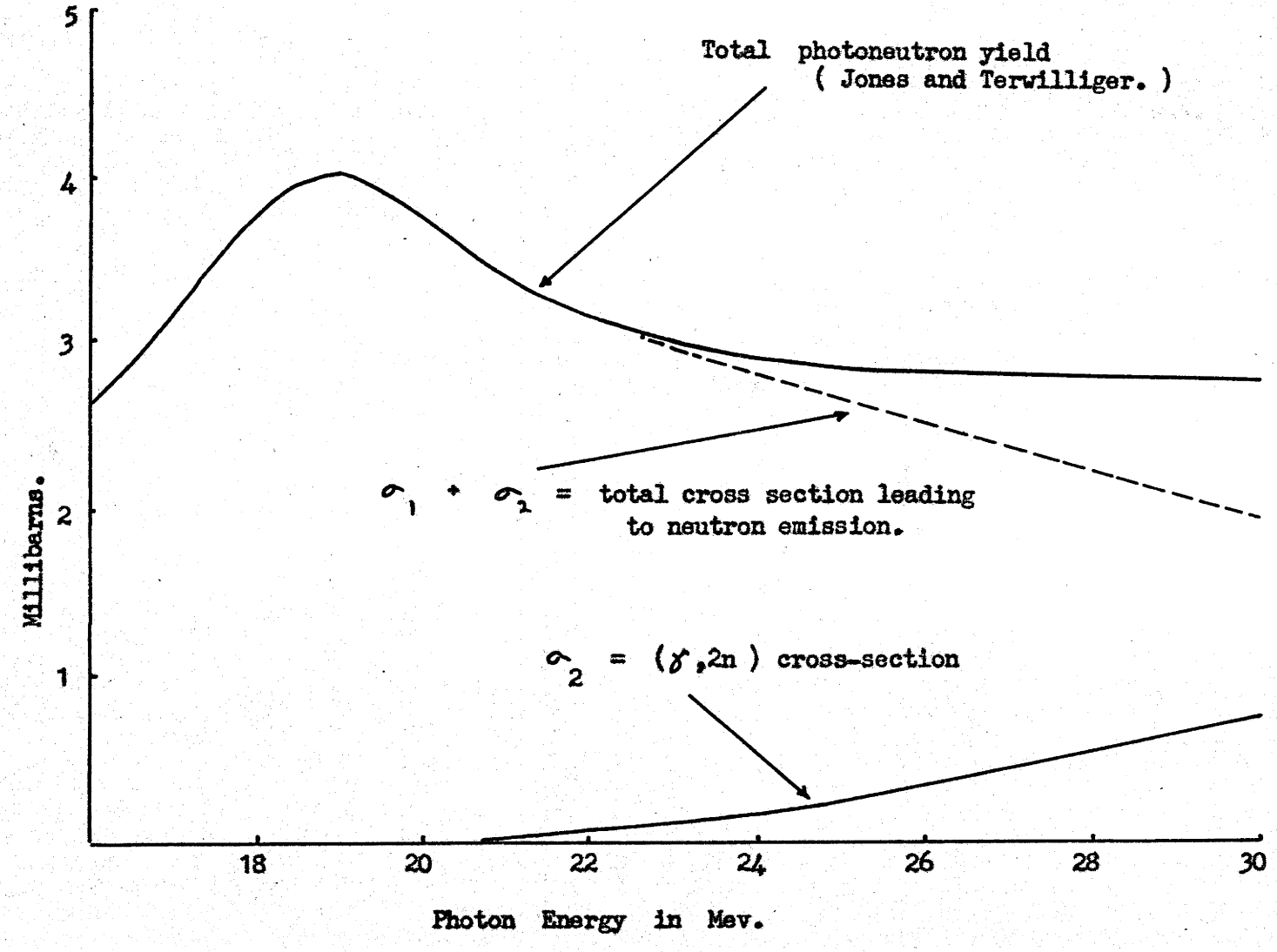

Figure 3.3 : Inferred Cross - sections.

tions, and accordingly an upper limit of 2 counts per minute was estimated for the maximum counting rate which could have been present, but would have been beyond the limits of detection.

The upper limit for the integrated cross section determined from this value, assuming the cross-section shape, is $\sim$7 Mev millibarn. This value is high because the low isotopic abundance of B^{10} (19%) means that only $\sim$ 2.4 grammes of B^{10} were irradiated. No errors are placed on it, since there is no way of estimating reliably the error on the number for the minimum detectable activity.

CHAPTER 4.

DIRECT EXCITATION IN THE PHOTODISINTEGRATION OF TANTALUM.

Abstract.

Single and multiple photoneutron yields from tantalum have been measured as a function of maximum bremsstrahlung energy. The measurements were made by residual activation in the former case, and by subtraction from the total yield, determined with the aid of the Szilard-Chalmers reaction in sodium permanganate, in the latter. The resulting yield curves have been analysed by the iterative method to determine the relative cross sections for single and multiple neutron reactions.

The ratio between the integrated cross sections from threshold to 31 Mev has been determined as:

$$\int_0^{31} \sigma_1 dE \;/\; \int_0^{31} \sigma_2 + \sigma_3 \, dE = 2.6 \pm 0.3$$

It is shown that for excitations beyond 17 Mev, emission of single neutrons arises largely from direct interactions, and the ratio of the integrated cross sections in this region is found to be:

$$\int_{17}^{31} \sigma_1 dE \;/\; \int_{17}^{31} \sigma_2 + \sigma_3 \, dE = 0.86 \pm 0.15$$

It is concluded from these observations that a large part of the photon absorption in the high energy tail above the giant resonance can be accounted for by direct interactions, and it is shown finally that the second experimental ratio is consistent with the ratio calculated for the decay of single particle states.

4.1 Introduction.

It was pointed out in Chapter 1 that in general the energy distributions of nucleons emitted following photon absorption do not agree exactly with the distribution calculated on the basis of the decay of a compound nucleus. It appears that there is generally present an anomalous high energy component which is attributed to direct interaction between the incoming photon and the emitted nucleon without the formation of an intermediate compound state.

The best estimates of the relative cross sections for direct emission and emission through a compound nucleus come from studies of photoproton cross sections in heavy nuclei, where virtually all emitted protons are direct because of the effect of the barrier. For direct protons, Wilkinson

finds reasonable agreement between the observed ratio of the direct cross section to the total absorption and the ratio calculated for the decay of single particle states.

The measurement of single and multiple neutron yields from heavy nuclei excited by high energy photons offers one means of estimating the same ratio for direct photo-neutrons. Among the heavy nuclei a high potential barrier strongly suppresses the emission of evaporated protons, so that a compound nucleus will almost invariably de-excite by "boiling off" a number of neutrons. Moreover, at high excitation, it is far more likely that a compound nucleus will decay by ejecting two or more comparatively low energy neutrons rather than a single one of high energy, and the expected number, the multiplicity, is readily calculable as a function of excitation energy. Thus the cross section for multiple neutron emission, which can be derived from the multiple yield when the multiplicity is known, is a measure of the cross section for the formation of a compound nucleus. Furthermore, since multiple emission is the dominant process at high excitation, any single neutron cross section must arise from direct interactions, and will not involve the formation of a compound nucleus. The details of this argument are developed more closely in the

succeeding paragraphs, in relation to the specific case studied.

4.1.1 Photoreactions in Tantalum.

Tantalum is a heavy nucleus, which is particularly suitable for a measurement of this nature. It meets satisfactorily the requirement of a high coulomb barrier for protons (13 Mev), is practically mono-isotopic, consisting of 99.99% Ta^{181} (W4) and has the advantage that the (γ,n) reaction can be measured simply by residual activation.

Table 4.1.

NEUTRON-PRODUCING REACTIONS IN TANTALUM.

Reaction	Threshold (Mev)	
$Ta^{181}(\gamma,n)$	7.6	*
$Ta^{181}(\gamma,2n)$	14.0	*
$Ta^{181}(\gamma,3n)$	22.2	*
$Ta^{181}(\gamma,np)$	13.4	**

* (L5) ** (c[illegible])

Neutron-producing reactions in tantalum which are energetically possible are listed with their thresholds in

Table 4.1. Of these, the (γ,np) is very unlikely if a compound nucleus is formed, since the high potential barrier will inhibit the evaporation of protons. It is a possible reaction following direct ejection of a proton, however, if the proton leaves sufficient energy in the nucleus to evaporate a second neutron, but again the proton must have sufficient energy itself to surmount the barrier, so that the effective threshold is raised to more than 26 Mev. It seems, therefore, that the (γ,np) reaction can be neglected, and that the only reactions which will contribute significantly to the neutron yield up to 30 Mev are simply emission of one, two or three neutrons.

4.1.2 Neutron Multiplicity.

In order to calculate the neutron multiplicity one must assume:

(i) a compound nucleus is formed, and the energy spectrum of emitted neutrons can be represented by the convential Maxwellian distribution

(ii) if an evaporated neutron leaves sufficient energy in the nucleus for a second neutron to be emitted, this invariably occurs.

The second assumption implies that there is no competition from gamma-ray emission in the decay of the compound nucleus, a condition which is approximately fulfilled except immediately above the threshold (B8). Protons, of course, will not compete because of the effect of the barrier.

Under these assumptions the energy distribution of evaporated neutrons is given by:

$$N(\varepsilon) \sim \text{const.}\, \varepsilon\, e^{-\varepsilon/\theta}$$

where θ, the nuclear temperature, is a function of the excitation energy $\hbar\omega$. This is the conventional peaked distribution with a maximum at $\varepsilon = \theta$, cutting off at a maximum energy $\varepsilon_m = \hbar\omega - B_n$, where B_n is the neutron binding energy (see Figure 4.1).

If a neutron emerges with energy less than $\varepsilon = \hbar\omega - B_{2n}$, there remains sufficient energy for a second neutron to emerge. By assumption (ii) this takes place, and the relative likelihood of one or two neutrons being emitted is proportional to the areas under the energy distribution to the right and to the left of the line $\varepsilon = \hbar\omega - B_{2n}$, from which the multiplicity, which is the mean number of neutrons per disintegration, can readily be obtained. The argument

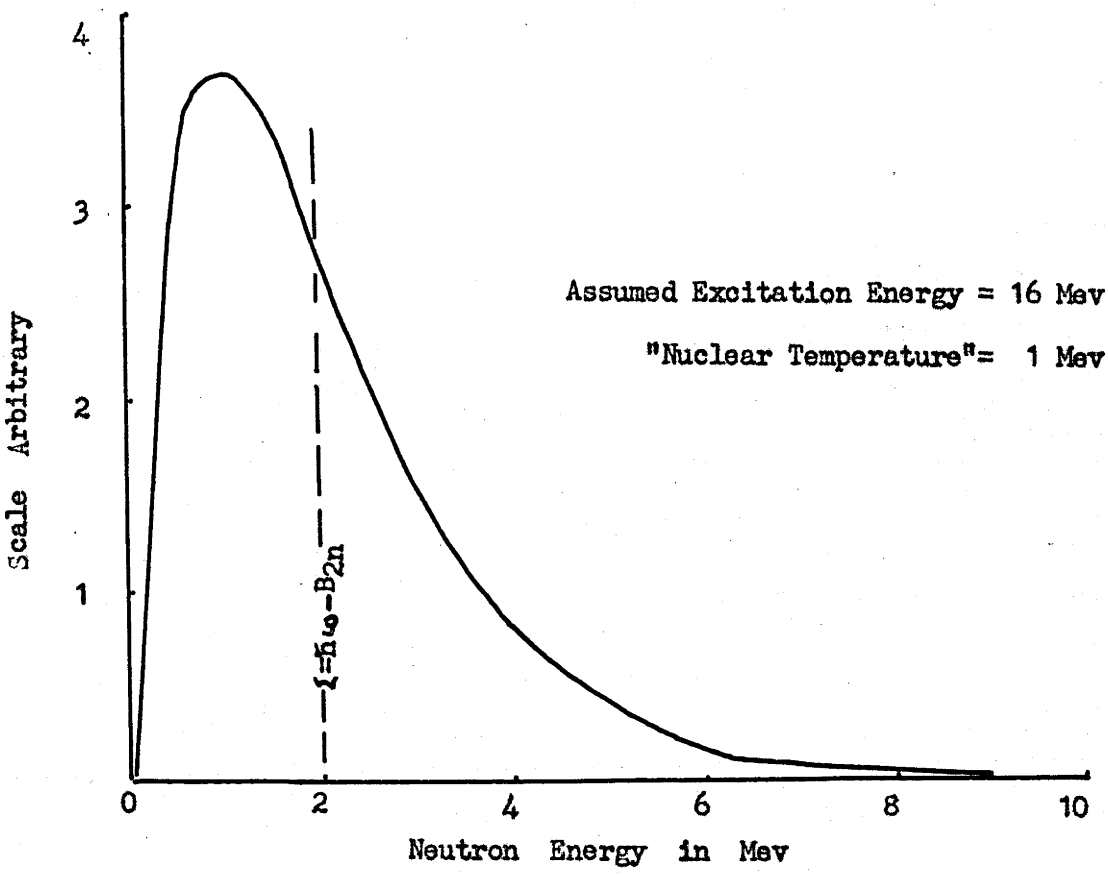

Figure 4.1 : Calculated Neutron Evaporation Spectrum

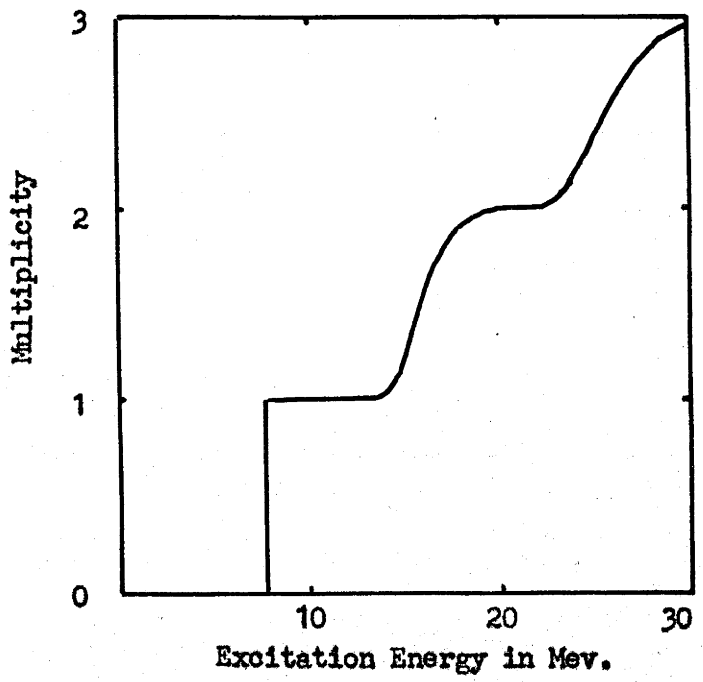

Figure 4.2 Neutron Multiplicity

can be extended beyond the (γ,3n) threshold, though the calculation then becomes a two-step process. The neutron multiplicity, calculated as a function of excitation energy to 30 Mev for tantalum by Levinger and Bethe (L5), is shown in Figure 4.2.

The important point for this experiment is that single emission of neutrons from a compound nucleus is negligible for excitations beyond about 17 Mev.

4.2 The Single Neutron Yield.

The measurement of the single neutron yield as a function of maximum bremsstrahlung energy was made by residual activation, in the same way as the activation measurements described in 2.5.3. Foils of copper and tantalum, enclosed in cadmium, were exposed to the beam for a given time, and the activities from 8.15-hour ^{180m}Ta and 9.4-minute ^{62}Cu were compared in the same Geiger-counting assembly. Below 16 Mev, however, the activity induced in the copper foils became too small to provide an accurate measure of the total dose, and, of course, below 10.7 Mev, the ^{63}Cu (γ,n) threshold, there was no copper activity at all. Thus, at these lower energies, the integrated current from a thick-walled ionisation chamber was taken as a measure of the total beam. The low energy measurements were normalised

to the yields monitored by the copper activity at 16 Mev*.

4.3 The Total Neutron Yield Measurements.

The multiple neutron yield was measured in this experiment by obtaining the total neutron yield and subtracting from it the single neutron yield as determined above (4.2). Of a variety of methods available for a total neutron measurement, the one chosen for its high sensitivity, comparatively uniform energy response in the moderating geometry employed and relative insensitivity to gamma rays, was the Szilard-Chalmers reaction in an aqueous solution of sodium permanganate, surrounded by paraffin moderator.

4.3.1 The Szilard-Chalmers Reaction.

Sodium permanganate is one of a number of unstable complex molecules which has the property that, following

---

* It must be mentioned that the tantalum beta-activity comes from the decay of an 8.15-hour metastable state in Ta^{180}, lying just above the ground state. It is necessary to assume that the ratio between the cross section for neutrons leaving the nucleus in this state and the total (γ,n) cross section does not change with photon energy. Experiments which measure σ_g/σ_m for In^{115} (γ,n) (G2), Br^{81} (γ,n) (K5) and Mo^{92} (γ,n) (K1) show that once sufficient energy is available for the metastable level to be excited, the ratio does not alter with excitation energy. In the present case, the level in Ta^{180} lies so little above the ground state that the ratio is assumed to be constant over the whole range.

(n,γ) absorption by one of its atoms, the recoil is sufficient to disrupt the molecule, so isolating the reacting atom in a different chemical form. In the case of permanganate, Mn^{56} from the reaction $Mn^{55}(n,\gamma)$ separates as manganese dioxide which can be readily extracted and concentrated by simple physical means. Filtration through carrier-laden filter paper suffices as the separation procedure.

The use of this reaction as a neutron detector depends on the fact that Mn^{56} is radioactive, with a half-life of 2.6 hours, and the activity collected on the filter paper is a measure of the neutron flux through the solution. Since the reaction involves thermal neutrons, the detection efficiency varies with neutron energy, and depends ultimately on the efficiency of the solution itself as a neutron moderator. It can be made more uniform either by using very large volumes of solution, so that effectively all neutrons are thermalised, or by the supplementary use of paraffin as a moderator. (c.f. 4.4).

Sodium permanganate was chosen in favour of the more commonly employed potassium salt, since it is possible to attain far higher permanganate concentrations with the former. At the concentration used (650 gr./litre), this

meant an increase in sensitivity of more than a factor of ten over that of a saturated $KMnO_4$ solution.

4.3.2 Experimental Arrangement.

The experimental arrangement for the total neutron yield measurements is shown in Figure 4.3. A strongly collimated bremsstrahlung beam from the electron synchrotron passed through a hole in the lead and concrete shielding to strike a tantalum target at the centre of a two-litre volume of aqueous $NaMnO_4$. This solution was contained in a spherical glass flask with a passage through its diameter for the beam.

The apparatus was aligned with photographic plates, and the beam collimated sufficiently to ensure that no gamma rays struck the solution or its containing flask directly. The solution was surrounded by 15 cm. of paraffin to reflect back neutrons and thus help flatten the energy response of the detector (c.f. 4.4), and a layer of borax and a further 15 cm. of paraffin shielded it from background neutrons produced in the machine room.

The target, consisting of a 1" x 1" x $\frac{1}{2}$" tantalum block placed in the centre of the flask, was irradiated for a period of twenty minutes at maximum bremsstrahlung energies ranging from 14 to 31 Mev. The total brems-

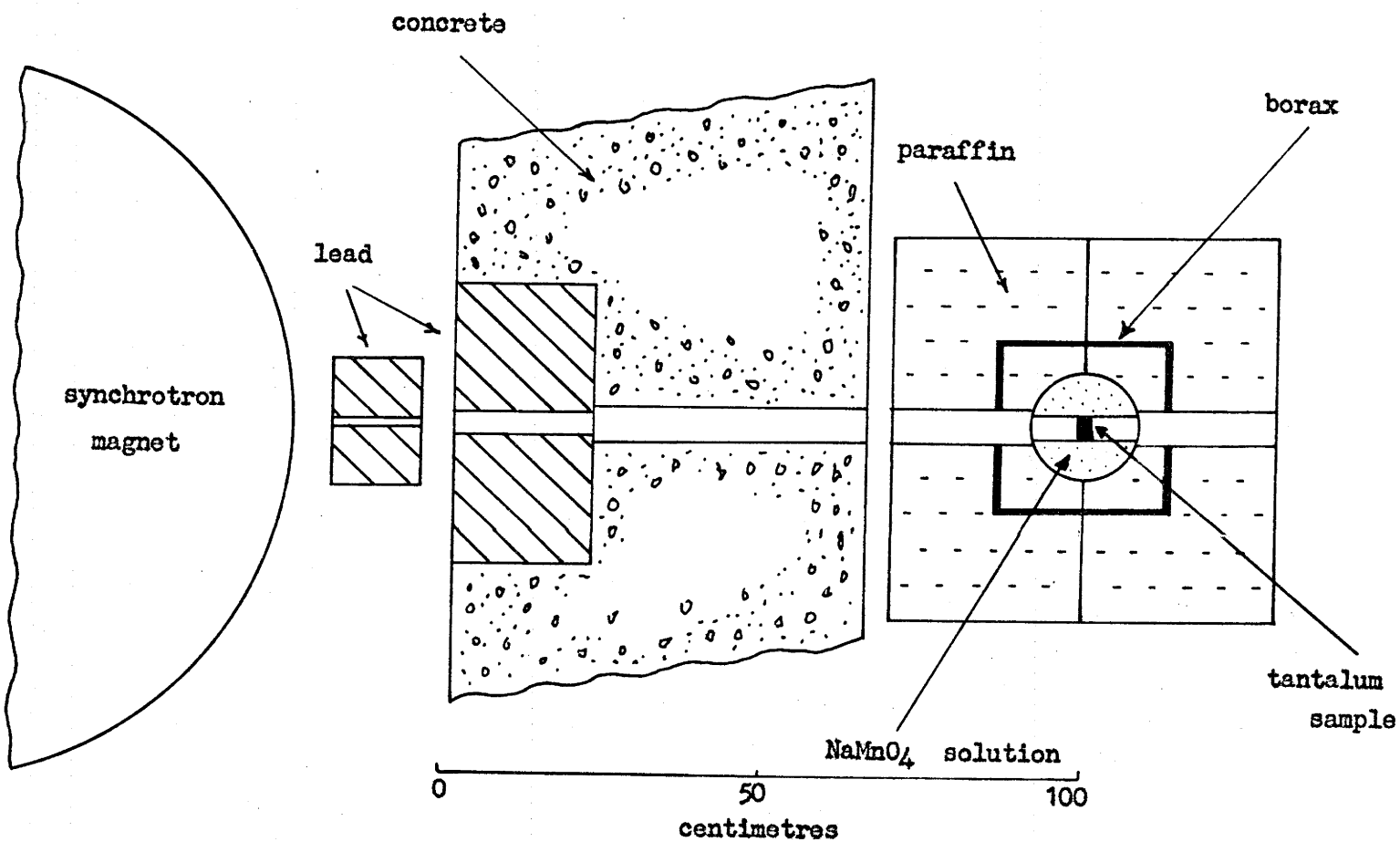

Figure 4.3 : Experimental Arrangement

strahlung dose was measured in the usual way, by the 9.4-minute positron activity induced in thin 1" x 1" copper foils irradiated with the target, and counted immediately afterwards with the standard thin-window Geiger counters (see 2.5.3). In addition, the beam was monitored by a continuously reading thick-walled ionisation chamber, and a few runs which showed large fluctuations in intensity were discarded.

Background runs, made with the copper foils in place but without the tantalum block, showed that the background was not large - less than 5% of the measured yield at 30 Mev - though correction had to be made for it.

4.3.3 Extraction of Mn^{56}.

The active manganese was extracted from the solution by filtering under pressure through No. 54 Whatman filter paper on a sintered glass backing, on which had been distributed 0.1 grammes of MnO_2 as carrier. At the end of the filtration the flask was washed, and the washings filtered and discarded. The pure filtered solution was retained and could be used again in about a day when the residual unextracted Mn^{56} activity had decayed. The filter paper was finally washed with distilled water, acetone and ether, and, when it had dried, the activity collected

on it was measured. The extraction process took about thirty minutes.

To measure the beta activity from the Mn^{56}, the dried filter paper was wrapped about a thin-walled long glass Geiger counter (Twentieth Century: Type B6) and the whole enclosed within two inches of lead. The lead served both to reduce the background from extraneous sources and to increase the count rate from the sample by scattering beta particles back into the counter.

Tests of the extraction and counting procedure with a standard radium-beryllium neutron source showed that the method gave results which were satisfactorily reproducible. A typical decay curve of the extracted activity is shown in Figure 4.4.

4.3.4 The Total Neutron Yield Curve.

The total neutron yield, with the background subtracted, is shown as a function of maximum bremsstrahlung energy from 14 to 31 Mev in Figure 4.5. On the same curve the neutron background is plotted, indicating that it was not large enough to be troublesome. Each point is the mean of at least three determinations, and each is accurate to within about 4 per cent.

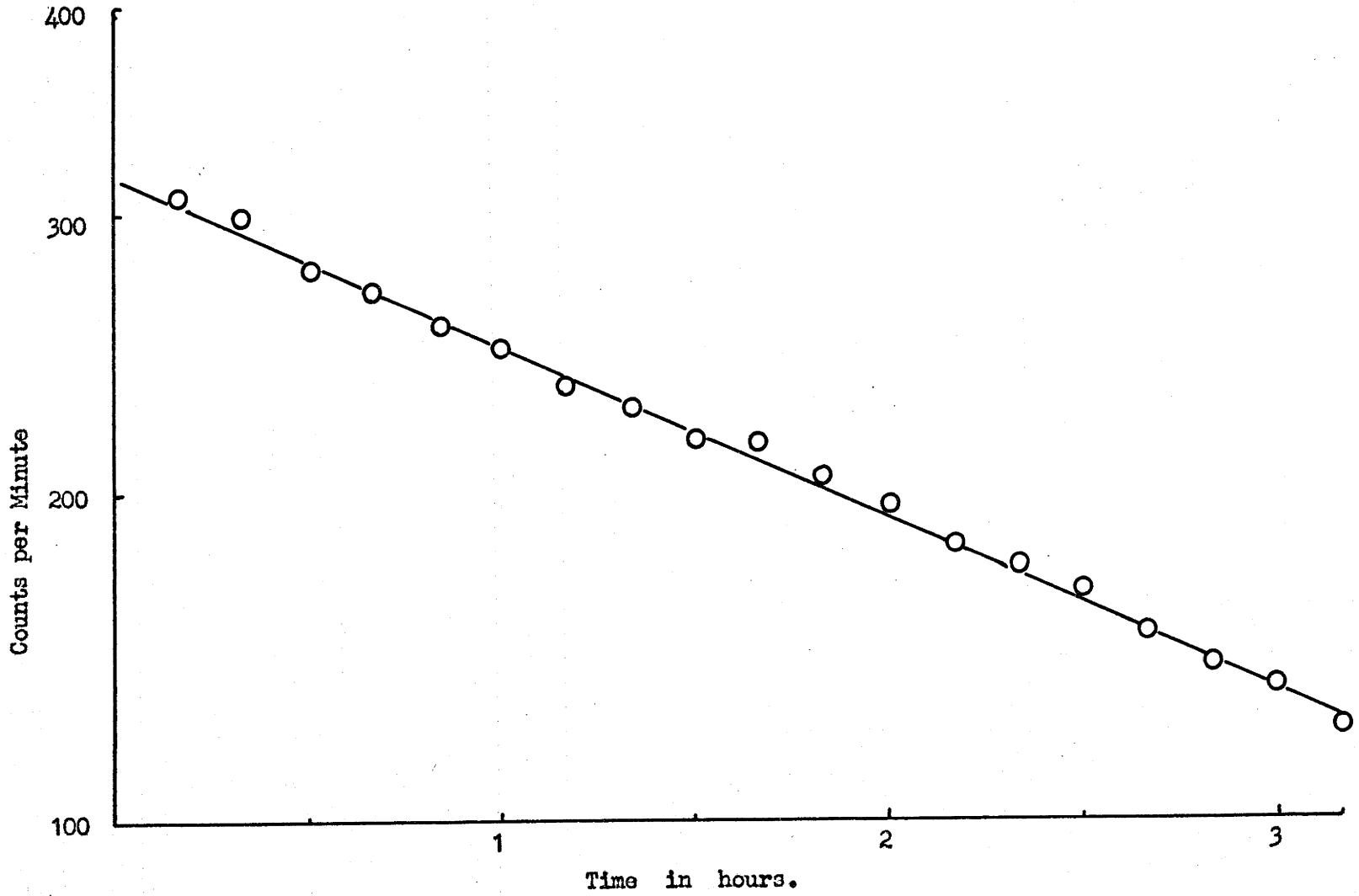

Figure 4.4 : Decay of Mn^{56}

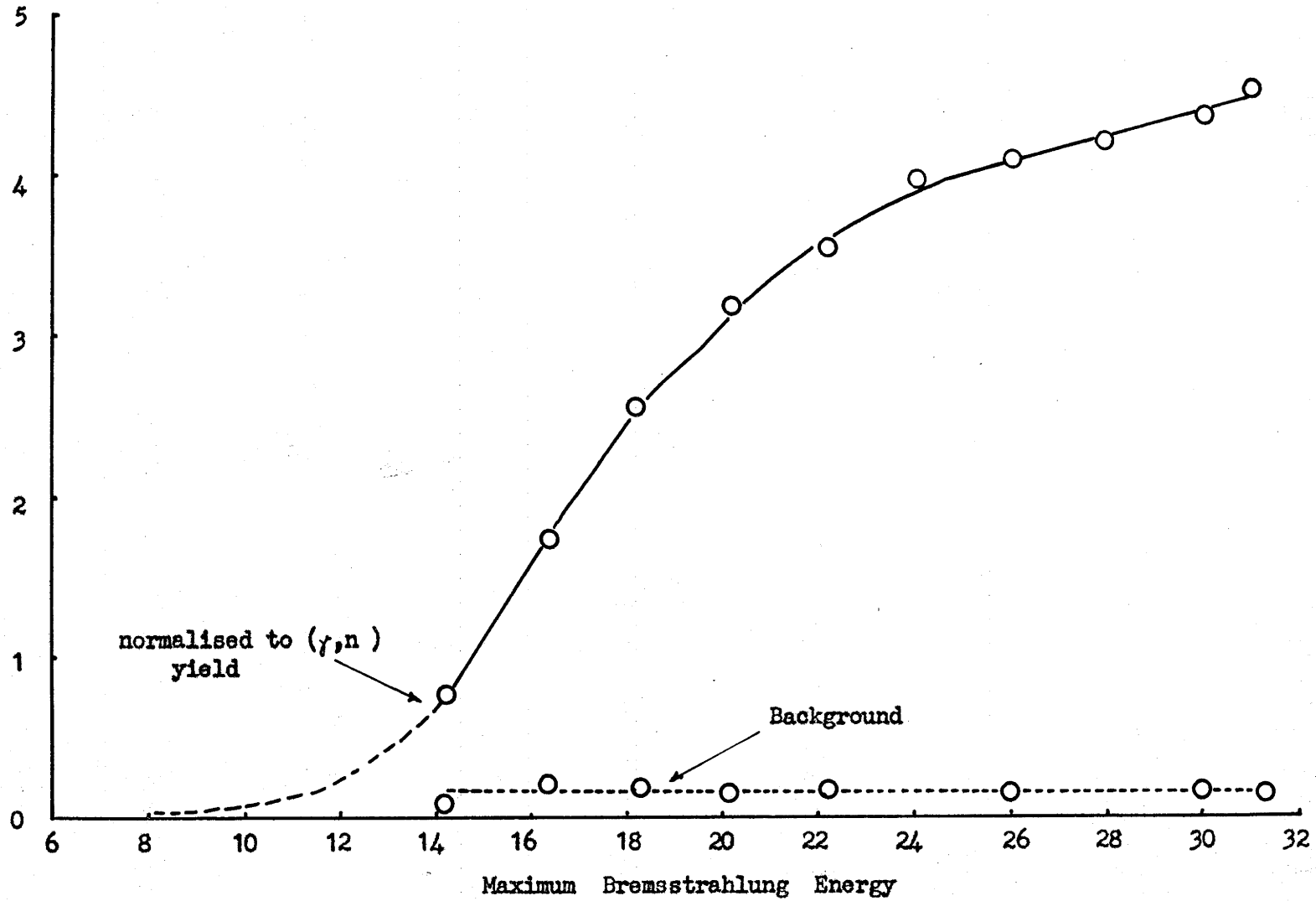

Figure 4.5 : Total Neutron Yield

4.4 Detection Efficiency as a Function of Neutron Energy.

The important assumption in the above determination has been that the efficiency of the Szilard-Chalmers detector remains constant as the maximum bremsstrahlung energy is varied. In the main this is so, since, although the response may not be uniform for all neutron energies, the evaporation spectrum of neutrons does not change much with excitation energy and most of the neutrons are evaporated. However, in this experiment, it is the neutrons which are not evaporated which are of the most importance.

4.4.1 The Use of a Larger Tank.

Accordingly, to determine whether the efficiency did change appreciably with excitation energy, the experiment was repeated at two energies, 18 Mev and 30 Mev, under much improved moderating conditions. A conical flask, with its apex directed at the target and filled with $NaMnO_4$, sampled a 700-litre volume of water moderator with the tantalum block at its centre. The water was contained in a large perspex tank with a passage through the centre for the beam, and a wood and cadmium lid to shield the solution from neutrons coming in from the top (see Figure 4.6). The water itself provided some shielding on the remaining sides, but because of the great size of the assembly, it

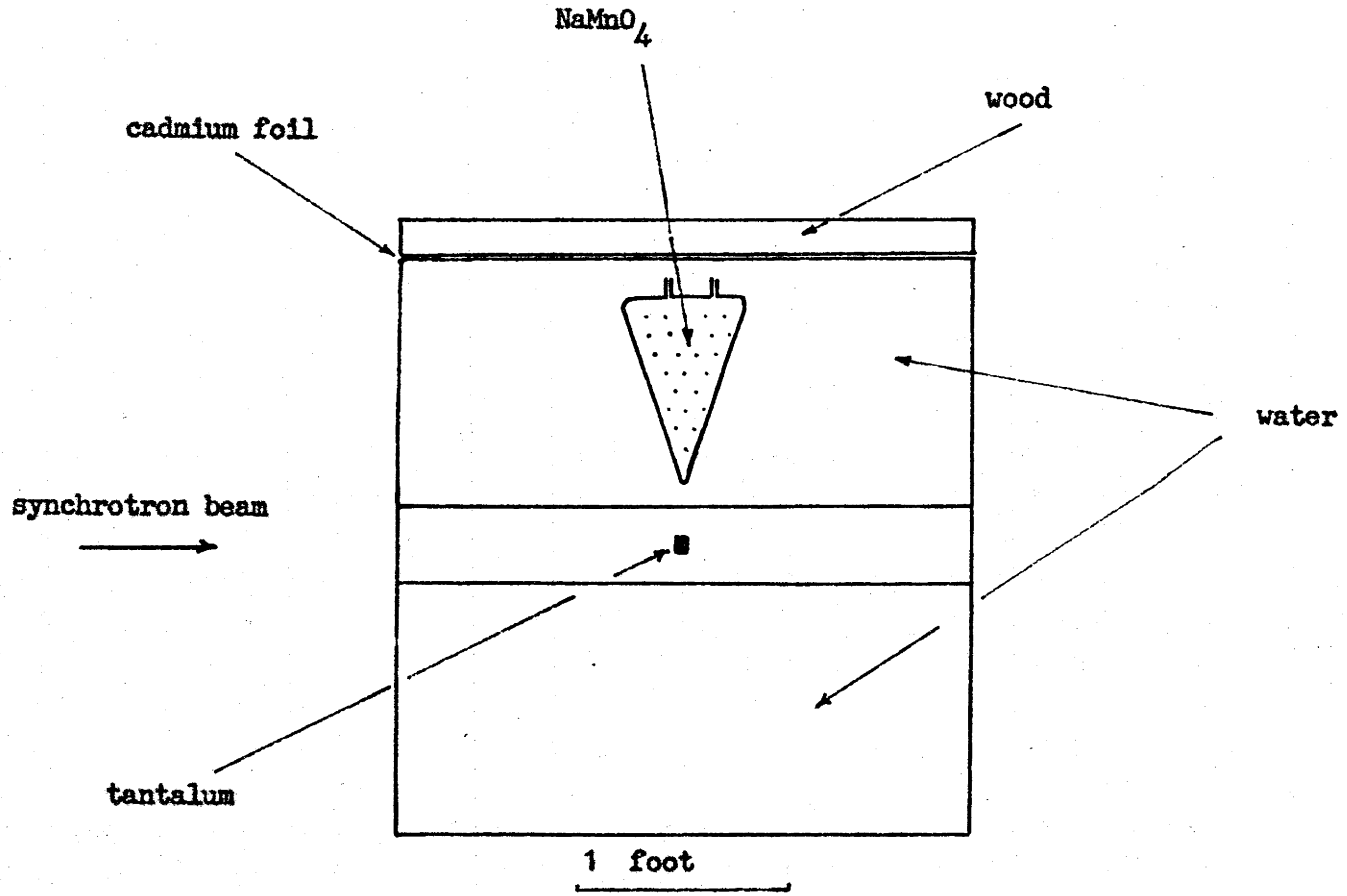

Figure 4.6 : The Large Tank

was not feasible to shield the solution as adequately as it had been in the smaller tank.

The ratio of the yields at 30 Mev and 18 Mev, as measured with the smaller detector, had been found to be 1.69 ± 0.08. The same ratio determined with the larger tank was 1.60 ± 0.14, indicating that no large errors had been introduced through the use of the two-litre flask.

4.4.2 Detection of ^{181}Ta $(\gamma,2n)$ by Residual Activation.

An independent method of confirming the same point, at least in part, was afforded by direct detection of the $(\gamma,2n)$ reaction through the 600-day activity (W8) of ^{179}Ta. Fresh tantalum foils, enclosed in cadmium, were irradiated for some six hours at maximum bremsstrahlung energies of 18 and 30 Mev. The total dose was monitored with the 8.15-hour activity in ^{180m}Ta, observed in this instance by pulse height analysis of its gamma-ray spectrum using a thallium-activated sodium iodide crystal and photomultiplier.

A single channel analyser, attached to a fast scaling circuit, was set to enclose the photopeak of the 55 Kev K-capture X ray of ^{180}Hf, and the decay of this line followed for about seven days. When the 8.15-hour activity had decayed (see Figure 4.7) there remained a single very

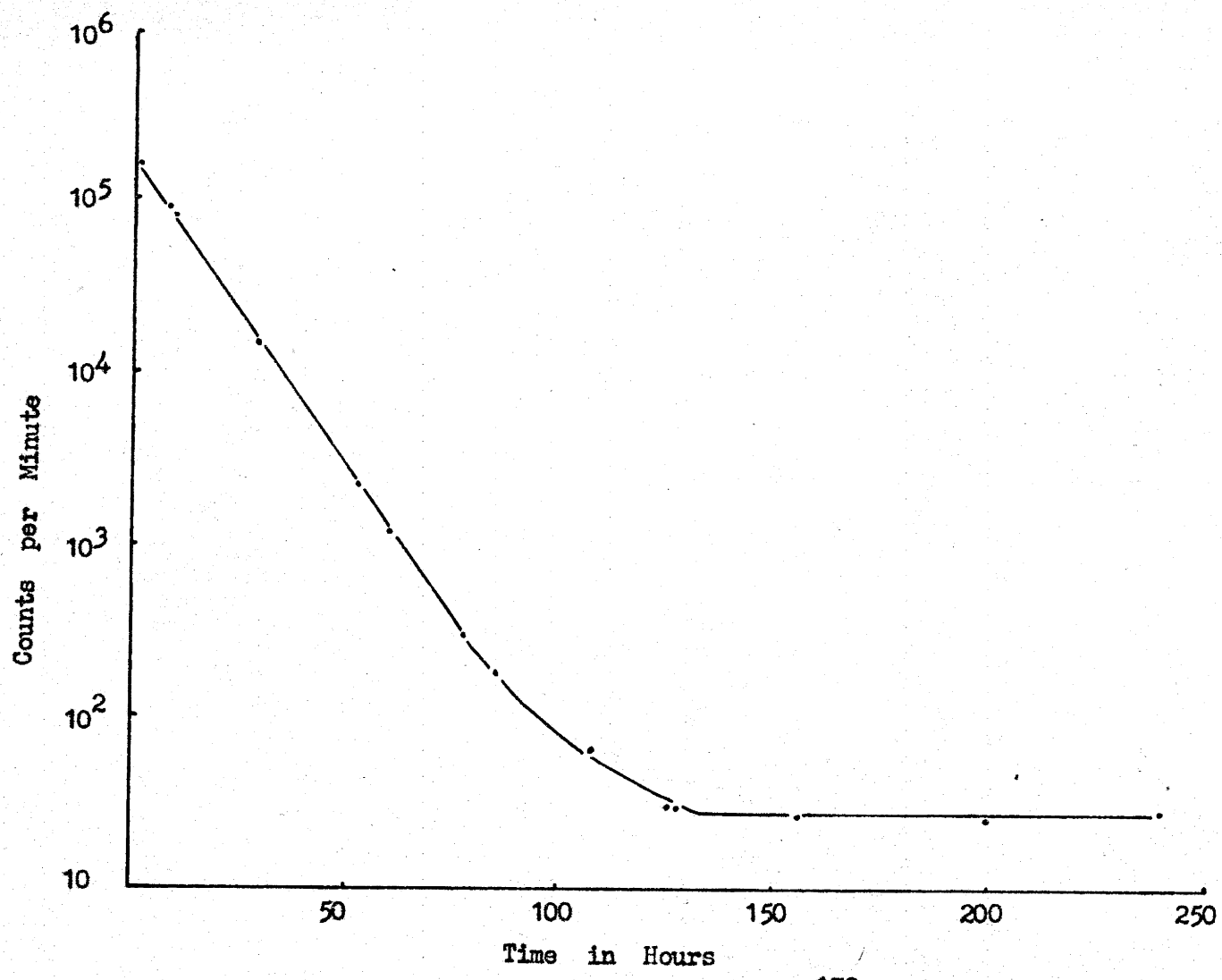

Figure 4.7 : Decay of Ta^{179}

long-lived line of the same energy, which was attributed to ^{179}Ta. The assignment of this activity could be made quite confidently, since ^{179}Ta emits no other radiations apart from its conversion X rays (W8, B7). The only other possibility would have been ^{182}Ta, formed by neutron capture, and, fortunately, this displays a considerably more complicated decay spectrum. In any case, this reaction would have been unlikely, since the tantalum was well-shielded by cadmium from thermal neutrons.

From the ratios of the $(\gamma,2n)$ and (γ,n) yields at 30 Mev and 18 Mev, and assuming no contribution to the total yield from the $(\gamma,3n)$ reaction, the ratio of the total yields at these two energies is 1.87 ± 0.2. This figure is to be compared with those quoted at the end of 4.4.1. Since the $(\gamma,3n)$ reactions can make some contribution to the total yield, this suggests that the total yield at 30 Mev probably lies slightly above that obtained by the Szilard-Chalmers measurement, though the discrepancy lies within the errors of that determination.

It is worth pointing out that this discrepancy does not affect the determination of the (γ,n) cross section, since this was made independently by residual activation.

A possible source of error in the total neutron

measurement could arise if the gamma-ray beam contained a large contamination of fast neutrons, since some of these could be scattered into the solution by the tantalum target. A calculation based on the number of fast neutrons known to be present in the beam (T1) showed this effect to be negligible.

4.5 The $(\gamma,3n)$ Cross Section.

An attempt was made to observe the $(\gamma,3n)$ activity by residual activation, in a careful study of the decay curves with the Geiger counters, following irradiation at a maximum bremsstrahlung energy of 30 Mev. These showed a pure decay of 8.15 hours, and no suggestion of any activities of half-life ten minutes or two hours (W8) corresponding to Ta^{178}. From this, an upper limit could be placed on the integrated $(\gamma,3n)$ cross section of less than about 5% of the (γ,n) cross section. This has been confirmed in a recent study of the $(\gamma,3n)$ cross section, using scintillation counters to examine the gamma radiation from Ta^{178} (C12).

4.6 Analysis of the Yield Curves.

The total and single neutron yields were normalised to the same value at 14 Mev, the $(\gamma,2n)$ threshold, and are shown, with the multiple yield which is the difference

between them, in Figure 4.8. The single and multiple yield curves were analysed by the iterative method, to give the cross section curves a (σ_1) and b (σ_m) of Figure 4.9.

The cross section σ_m is made up of σ_2, the (γ,2n) cross section, and σ_3, the (γ,3n) cross section, since the (γ,np) cross section has been shown to be insignificant (c.f. 4.1.1). Thus:

$$\sigma_m = 2\sigma_2 + 3\sigma_3.$$

To determine the cross section for absorption leading to the formation of a compound nucleus, it is necessary to divide σ_m between σ_2 and σ_3. Below 22.2 Mev, the (γ,3n) threshold, σ_3 is zero, so that:

$$\sigma_m = 2\sigma_2$$

exactly, and beyond this energy the cross section is divided between them assuming the multiplicity derived by Levinger and Bethe (c.f. 4.1.2 and Figure 4.2). This is an extreme assumption, which over-estimates σ_3, since the compound nucleus formed may follow a direct interaction between a photon and a nucleon, in which the emitted nucleon makes an inelastic collision with the nucleus

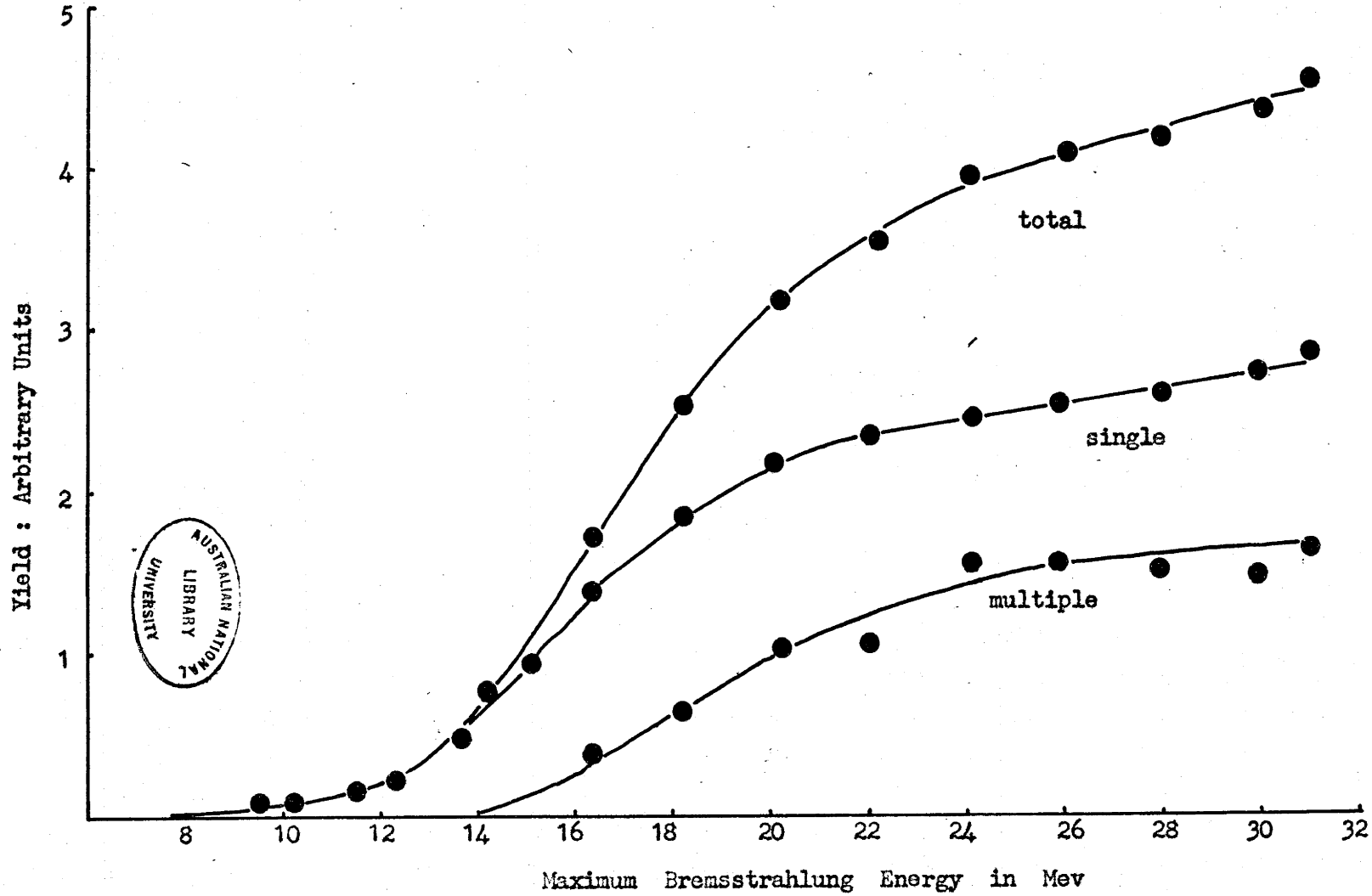

Figure 4.8 : Neutron Yield Curves

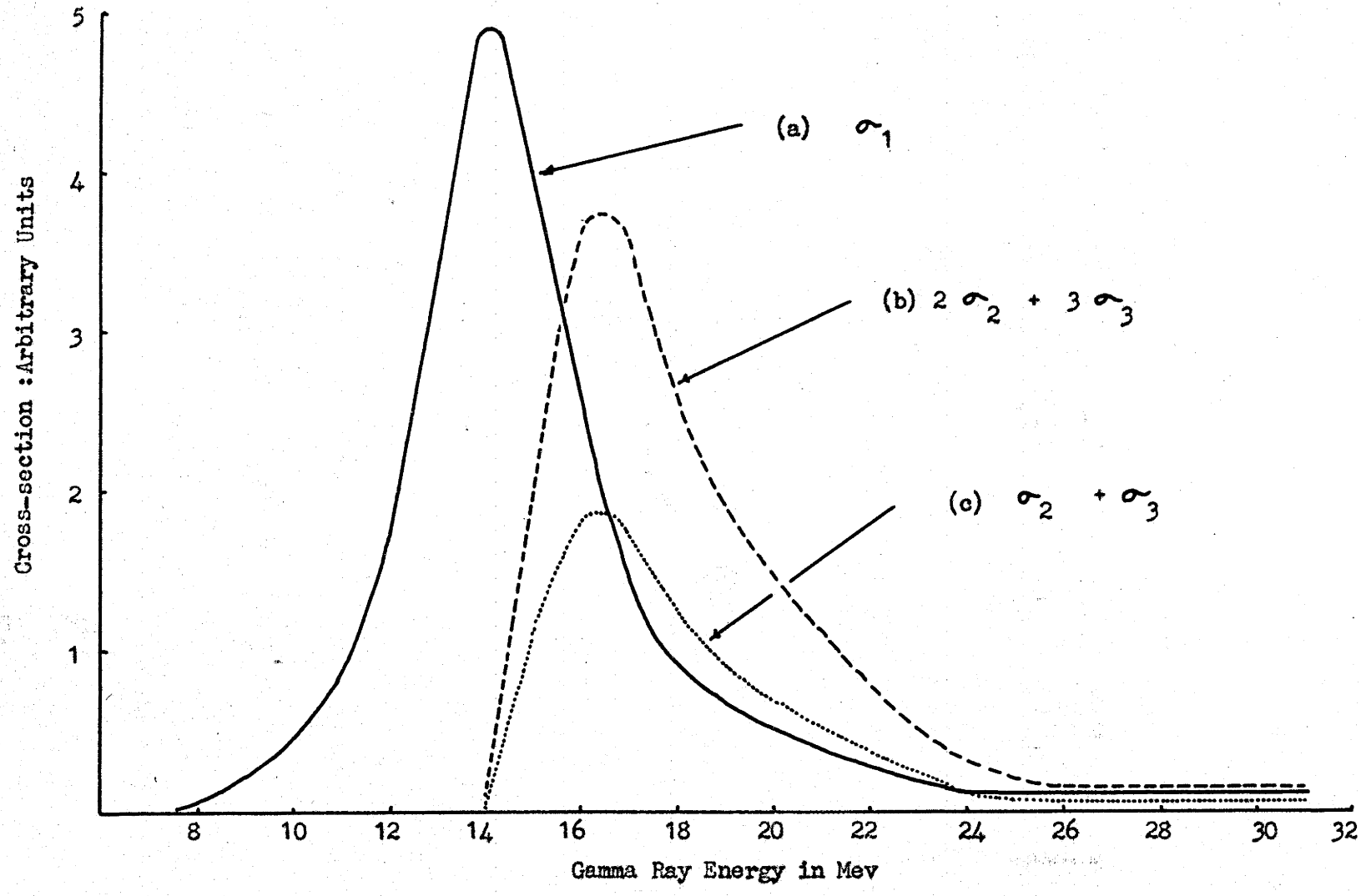
Cross-section :Arbitrary Units
5
4
3
2
1
8
10
12
14
16
18
20
22
24
26
28
30
32
Gamma Ray Energy in Mev
(a) σ_1
(b) $2\sigma_2 + 3\sigma_3$
(c) $\sigma_2 + \sigma_3$

Figure 4.9

before it escapes. Alternatively, a neutron may be ejected from a deep-lying shell, leaving sufficient energy in the nucleus to evaporate a second neutron. The other extreme is to assume that σ_3 is zero, in which case the curve c $(\sigma_2 + \sigma_3)$ of Figure 4.9 would be multiplied by a factor which is unity below 22 Mev and increases to 1.5 at 31 Mev. The uncertainty involved in the division of σ_m between σ_2 and σ_3 is, however, not very serious in the interpretation of these results (see below).

According to the above assumption the curves a (σ_1) and c $(\sigma_2 + \sigma_3)$ represent the cross sections for absorption leading to single and multiple emission respectively. By numerical integration, the ratio of the integrated cross sections for these two modes of decay is found to be:

$$\int_0^{31} \sigma_1 \, dE \Big/ \int_0^{31} \sigma_2 + \sigma_3 \, dE = 2.65 \pm 0.3$$

and from 17 Mev, beyond which energy single emission is unlikely from a compound nucleus:

$$\int_{17}^{31} \sigma_1 \, dE \Big/ \int_{17}^{31} \sigma_2 + \sigma_3 \, dE = 0.86 \pm 0.15.$$

The errors quoted on these ratios are derived from the errors on the measured yield curves, since to quite a good approximation the bremsstrahlung yield is a measure of the integrated cross section. As is indicated above, there is some additional uncertainty, depending on how the cross section σ_m is shared between σ_2 and σ_3. This amounts to 7 per cent for the second ratio, between the two extremes of all or no σ_3 at 31 Mev, and about 3 per cent for the first.

These results may be compared with the measurements made at 17.6 Mev using the $Li^7(p,\gamma)$ radiation (C2, C3) in which the ratio of the cross sections at 17.6 Mev was found to be $\sigma_1/\sigma_2 = 0.9 \pm 0.4$.

4.7 Discussion.

Because of the uncertainty in the shape of the bremsstrahlung, and the errors in the experimental yield curves, it would be unwise to place too much reliance on the detailed shapes of the cross-section curves far beyond their respective peaks, apart from observing that they appear to be of the same order of magnitude over the range 17 to 31 Mev. The ratios of the integrated cross sections, however, subject to their quoted errors, are better determined, and the second ratio is of particular interest.

When it is recalled that in this region single neutron emission should have given way almost entirely to multiple emission in the decay of a compound nucleus, it is apparent that much of the absorption must take place without the formation of a compound state. Furthermore, the cross section for decay via a compound nucleus may still be over-estimated, since it has been assumed that all multiple emission derives from a compound nucleus. As is indicated above (c.f. 4.6), some multiple emission may occur following direct interactions.

If the absorption is thought of from the point of view of single particle transitions from closed shells, the relative probabilities of direct emission and absorption into a compound nucleus may be estimated in the way suggested in 1.4.2 (p. 16). The width without barrier for a neutron in tantalum excited by a gamma ray of $\sim$ 18 Mev (say a neutron energy of 10 Mev) is:

$$\Gamma \approx \frac{3}{2}\frac{\hbar^2 k}{mR} = 6.3 \text{ Mev.}$$

The transitions responsible for photon absorption in this energy region are almost certainly between shells of lower angular momentum than the strong $1h_{9/2}$ - $1i_{11/2}$ and

$1h_{11/2}$ - $1i_{13/2}$ transitions which account for the resonance at 14 Mev, and the neutron width from them will not, therefore, be much affected by the centrifugal barrier*. Thus it is considered that the above width is close to the width for direct emission.

The width for absorption into a compound nucleus is equal to twice the imaginary part of the complex potential, and may be estimated from the model of Feshbach, Porter and Weisskopf (F4). For low energy neutrons, they find a good fit to average neutron cross sections with a complex potential $V = 42(1 + 0.03i)$ Mev, and a width for absorption therefore of $2 \times 0.03 \times 42 = 2.5$ Mev. Cini and Fubini (C13) suggest that this increases rapidly with energy, according to the expression $(E + B)^2 / B^2$, where E is the neutron energy and B is the binding energy of the last neutron; this would imply in this case a value of $2W \approx 10$ Mev. There is thus considerable uncertainty in the value of the width for absorption into a compound nucleus, though these two values probably represent reasonable

---

* The centrifugal barrier height for neutrons in an i-shell ($l = 6$) is ~ 13 Mev; for neutrons in the next worst circumstance ($l = 5$) the barrier is ~9 Mev and it is likely that the transitions involve shells of lower angular momentum than this.

limits *.

Using these estimates, the fraction of neutron transitions which lead to direct emission is 6.7 / 6.7 + 2.5 = 70% (2W = 2.5 Mev) or 6.7 / 6.7 + 10 = 40% (2W = 10 Mev). Since neutron transitions account for only half of the total absorption, and none of the proton transitions can yield direct neutrons, this suggests that about 20 to 35 per cent of the total absorption above 17 Mev results in direct emission of neutrons.

The measured ratio for the integrated cross sections above 17 Mev for direct emission, and for the formation of a compound nucleus, is 0.86. This ratio is largely determined by the cross sections between 17 and 20 Mev, where direct proton transitions are negligible since the potential barrier is still important. Thus the fraction of the total absorption leading to direct neutron emission is close to 0.86/1.86 = 45%, and agrees remarkably well with the estimate above; it is therefore concluded that the observed direct emission can be satisfactorily accounted for in terms of the decay of single particle transitions.

---

* In studies of the fast neutron component from bismuth, Ferrero et al (F2) have found reasonable agreement with experiment using a value of 2W = 10 Mev.

CHAPTER 5.

DIRECT PHOTOPROTONS IN THE PHOTODISINTEGRATION OF SILVER.

Abstract.

A thin-crystal proton spectrometer has been used to measure the energy distributions and yields of high energy photoprotons from thin silver foils as a function of maximum bremsstrahlung energy. From the measured yield curves and the proton energy distributions the cross section for protons which can be identified as direct is inferred, and is shown to display a resonance in the region of 22 Mev. The integrated cross section for emission of protons of energy greater than 10 Mev is found to be 36 ± 10 Mev millibarn.

The absolute yield and the cross-section shape are discussed, and indicate that it is not necessary to propose a separate absorption mechanism for the direct cross section in this case; in particular, it is demonstrated that the results are consistent with a single particle theory of photonuclear absorption, and it is suggested that much of the direct photoproton cross section in silver arises from a strong single particle transition between the 2p and 2d shells.

5.1 Introduction.

In studies of the energy distributions of photoprotons it has been established that a substantial number of protons is emitted with more energy than is expected if a compound nucleus is invariably formed (C10, D4, B12 etc.). Energy distributions generally show a broad "evaporation" peak at an energy determined by the height of the Coulomb barrier, and an anomalous tail of high energy protons which extends out to the maximum proton energy possible for a given excitation.

It is generally presumed that this high energy component is a consequence of direct interactions, and does not involve the formation of a compound nucleus.

This experiment was undertaken to determine the variation with energy of the "direct" cross section in silver, with a view to deciding whether it exhibits the same behaviour as the giant resomance, or whether it must be accounted for by some independent absorption mechanism. It is shown later (see 5.7.1) that there should be no significant yield of photoprotons from silver with energies greater than ~ 10 Mev if the protons are evaporated from a compound nucleus, so that protons of higher energy are almost certainly direct; the cross section for emission of

protons in this energy range can thus be taken as a measure of the cross section for direct interactions with protons. It is by no means a complete measure, of course, since some of the lower energy protons are certain to come from direct interactions with lower energy photons in the bremsstrahlung spectrum and from transitions from deeper lying shells, and there is unfortunately no way of distinguishing these from protons which are emitted following the formation of a compound nucleus.

To determine the cross section for fast photoproton emission it is necessary to measure both the absolute yields and the energies of protons as a function of maximum bremsstrahlung energy. Knowledge of the energy then serves to identify direct protons in the distribution, and a bremsstrahlung yield curve can be constructed for this component. This may be analysed in the normal way to derive a cross-section curve for emission of protons of greater than a specified energy, though some caution is necessary in its interpretation, since the threshold of the bremsstrahlung yield curve does not reflect the threshold for direct emission. Silver is a good choice for this type of experiment, since its low proton binding energy (approximately 6 Mev in both Ag^{107} and Ag^{109} : D4) means that "direct" photoprotons may be detected at photon energies

as low as 16 Mev.

Seen in this light, the experiment is the equivalent of the fast neutron measurements of Ferrero et al (F2) who used threshold (n,p) detectors to measure bremsstrahlung yields of anomalous high energy neutrons. However, the method promises more information than is available when a simple threshold detector is used. A modified "photon difference" analysis can be applied to the difference between proton spectra taken at successive energies, to give immediately the cross section for direct protons which remove all the excitation energy from the nucleus (see 5.6.2).

5.2 The Proton Detector.

The design of the scintillation detector used to measure the energies of photoprotons is shown in Figure 5.1. A 1" x 1" square crystal of thallium-activated caesium iodide sufficiently thick to stop protons of energy up to 24 Mev* (0.100") was cemented edgewise onto a ¼" thick

---

* The range of protons in caesium iodide was estimated by interpolation of published range energy tables (R1) to determine the proton ranges in caesium and iodine, and weighting these according to the expression:

$$1 / R_{CsI} = 1 / R_{Cs} + 1 / R_{I}$$

circular glass plate with clear araldite casting resin, and enclosed within a spherical reflecting shell of aluminium. The inside surface of the aluminium was electrolytically polished to produce an extremely clean matte surface, ideal for diffuse reflection with low loss; this arrangement meets satisfactorily the requirement that the amount of light collected and transmitted through the glass plate should be independent of the position within the crystal at which a scintillation event occurs. A thin (4 mg./sq.cm.) window, one inch square, of polished aluminium foil in one side of the reflector admitted protons to the crystal without significant energy loss (~ 50 Kev for a 10 Mev proton), and since the detector was operated in vacuo, a number of small holes was drilled about the base of the aluminium reflector to evacuate it along with the experimental apparatus. As these holes were small (1/32"), it was not anticipated that their presence would affect materially the amount of light collected.

Scintillation pulses from the crystal were detected with an E.M.I. Type 6097E photomultiplier, which was optically bonded to the glass base with silicone oil. Voltage pulses from the photomultiplier were shaped and amplified in the usual way and fed finally to a Hutchison-Scarrot 80-channel

pulse height analyser.

The performance of the scintillator was assessed by measuring the alpha particle spectrum from ThC''; a typical spectrum, taken in vacuo with an uncollimated source, is shown in Figure 5.2. The two alpha particles, of initial energies 8.8 and 6.9 Mev, but somewhat degraded by the aluminium window, are cleanly separated, with an energy resolution of approximately 6 per cent. Some of this spread may be ascribed to variations in energy lost by alpha particles in passing through the aluminium window at differing angles, since the window was relatively thick for alpha particles (an 8.8 Mev alpha particle at normal incidence loses about 1.7 Mev in passing through this thickness of aluminium). The resolution for protons was probably somewhat better than this, and certainly more than adequate for the experiment performed.

5.3 Energy Calibration.

In connection with another experimental programme in this laboratory the proton response relative to the response for the 8.8 Mev ThC'' alpha particle was determined for a piece of caesium iodide from the same batch by measuring the relative response for known proton groups from the reaction $B^{10}(d,p)B^{11}$. The measurement was performed in-

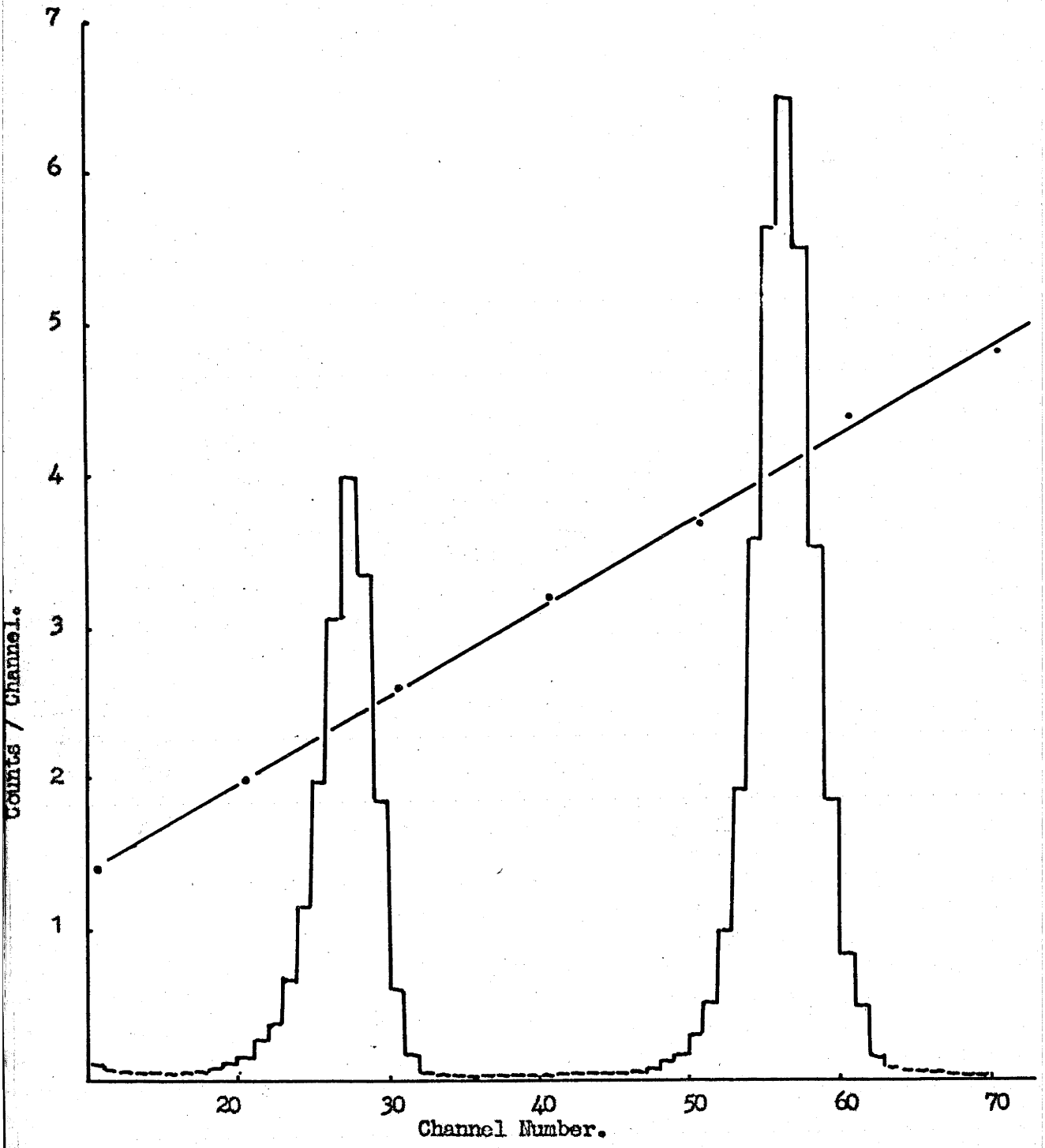

Figure 5.2 : Alpha Particle Spectrum.

dependently by Mr. I. F. Wright (W11) and no further description is given therefore in this thesis.

For this batch of caesium iodide, the light output from the 8.8 Mev alpha particle after it had passed through the aluminium window was the same as that from a proton of energy 5.4 ± 0.2 Mev. This figure was taken to determine the proton energy scale, and was found to agree very well with the figure derived from the maximum energy expected for photoprotons from silver irradiated with 30 Mev bremsstrahlung (~ 24 Mev).

5.4 Experimental Details.

5.4.1 The Proton Counter.

So that protons would not lose energy in passing from the foil target to the crystal, the counter was maintained at a pressure of about 100 microns with the aid of a rotary pump. A diagram of the experimental assembly is given in Figure 5.3. Bremsstrahlung from the synchrotron passed through a 3/8" lead collimator, to produce a well-defined pencil of gamma rays of diameter ~ ½" at the target. The beam, cleared of electrons by a strong permanent magnet placed behind the collimator, entered the target tube through a thin aluminium window. Beyond this, a further magnet was mounted to deflect out of the beam

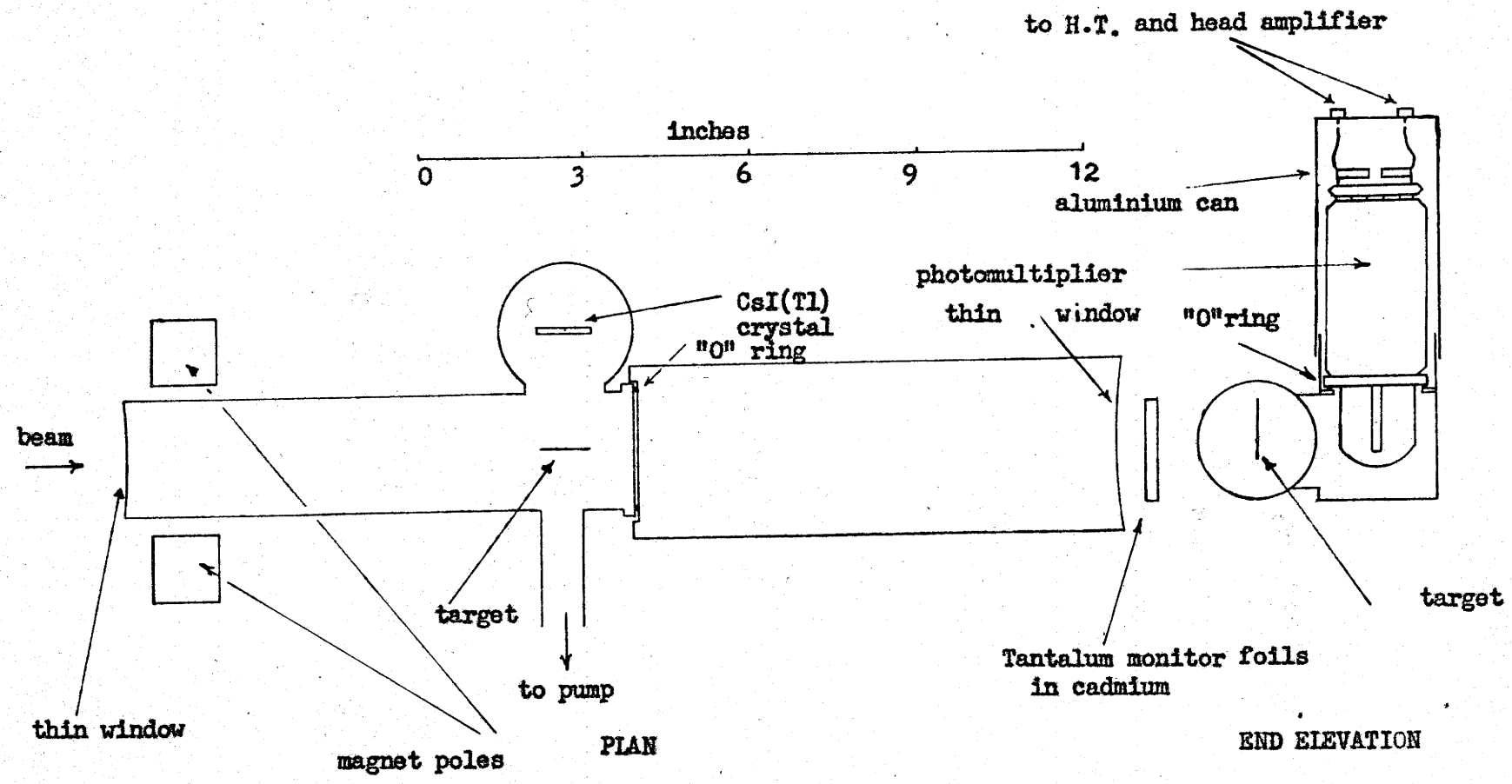

Figure 5.3 The Counter

electrons produced in the window, so that a relatively "clean" bremsstrahlung flux irradiated the target of thin silver foil.

The target tube could be broken just beyond the foil to facilitate the interchange of target and standard alpha particle source, and the diameter of the tube beyond this point was increased to 2½" to ensure that the beam, which was slightly divergent, did not strike the thick side walls; the beam emerged again through a similar thin window of aluminium.

The crystal detector described in 5.2 was mounted as shown in Figure 5.3, with the crystal parallel to and directly opposite the target, to detect photoprotons emerging at ninety degrees. A short 1½" diameter tube connected the target tube to a 2½" diameter brass cylinder, which housed the crystal and photomultiplier. The glass plate to which the crystal was attached rested on an "O" ring on a ledge inside the cylinder, to make a vacuum seal, and the photomultiplier was enclosed in an aluminium can fixed over the brass with black "scotch" tape.

Leads to provide H.T. for the phototube, and to take out pulses from the last dynode, were soldered from the appropriate lugs on the photomultiplier base to light-tight

Belling-Lee plugs on the aluminium can; standard co-axial cables connected these to the H.T. supply and the head amplifier.

5.4.2 Shielding.

Since a crystal of the dimensions used would detect gamma rays with high efficiency, it was imperative that it be thoroughly shielded from both the direct beam and scattered low energy radiation in the research room. Accordingly, the counter was enclosed in lead, so that there were at least three inches of lead shielding the crystal from every direction. In addition, permanent shielding around the machine provided about twelve inches of concrete, lead and steel between the crystal and the bremsstrahlung source, and steel walls about three inches thick shielded the counter from scattered radiation from either side. The beam was finally caught in a "beam trap" at the end of the room, so that scattered radiation should have been at a minimum. The complete lay-out of the shielding is indicated in Figure 5.4.

That the shielding was generally effective was indicated by the fact that when the machine was run without the target in the proton counter, no pulses were recorded corresponding to energies greater than about 6 Mev, and the

counting rate below this energy was less than a tenth of the counting rate with the target in position.

5.4.3 Measures to Reduce Electron Background.

The chief difficulty in this experiment, and one which is encountered whenever electronic counting devices are used to detect photoprotons, was the problem of discriminating against electrons, since photon interactions which produce electrons are orders of magnitude greater than photoproton cross sections. The problem is aggravated further when bremsstrahlung is used as the source of gamma rays, since:

(i) there is a huge flux of low energy gamma rays, which can produce electrons, but which are below the threshold for photoproton emission

(ii) electron accelerators are pulsed machines, so that all of the bremsstrahlung output arrives virtually simultaneously, and large fluxes of low energy electrons scattered from the target may "pile up" to produce big pulses indistinguishable from protons.

The first difficulty can be partly overcome by filtering the beam through a suitable thickness of carbon, which strongly absorbs low energy photons (say $<$ 1 Mev) without

attenuating high energy gamma rays too severely. Accordingly, in a first attempt to reduce the electron "noise", the beam was filtered through six inches of graphite, a thickness which reduces the flux of 0.5 Mev gamma rays by a factor of 10^3, but cuts the intensity of 20 Mev gamma rays to only about 60 per cent (S7). It was found, however, that this made no detectable difference to the electron background, and, since it was felt that any sacrifice of intensity was not worthwhile unless accompanied by a real improvement in the discrimination against electrons, the carbon was ultimately discarded.

More success was met with, however, when parameters influencing pile up were varied. Every effort was made to make pulses from the photomultiplier as short as possible, consistent with linearity. The cable from the photomultiplier to the head amplifier was made short to keep the pulse rise time small, and pulses were straight away clipped with a short time constant R-C network to have a total length of just less than a microsecond. They were then passed through a biassed diode with the bias level set to cut off pulses representing energies of less than $\sim$ 5 Mev, and fed straight to the grid of a cathode follower. In this way small electron pulses were biassed out before

stray capacities increased their length and allowed them to pile up.

In addition, the duration of the bremsstrahlung output pulse could be increased on this machine by decreasing the rate of collapse of the radio frequency amplitude. The duration of the bremsstrahlung output was increased by this method to ~ 200 microseconds, and helped further to control pile up. The problem was not, of course, completely overcome, since many gamma rays were still bunched within each microsecond, but some improvement was made in this way.

In order to discriminate between proton and electron pulses, 150 mg./sq.cm. of aluminium absorber was placed between the target and the detector, and the spectrum obtained after an irradiation at 30 Mev compared with an identical irradiation without any absorber. This thickness of absorber was chosen as the best compromise between an absorber which would stop all protons, and one which would not alter the electron background too seriously.

The result of these runs is shown in Figure 5.5. It is seen that the end-point of the spectrum is reduced from 24 Mev to about 22 Mev, and that the yield of protons with a net energy greater than 8 Mev is the same as the yield above 13 Mev from the run without absorber. Since 150 mg./sq.cm.

of aluminium reduces the energy of a 13 Mev proton to 8 Mev, this indicates that all pulses above 13 Mev are due to protons, and if the absorber does not distort the electron edge too severely then most pulses above 8 Mev also indicate protons. As is expected, the electron background is only shifted downwards in energy by one or two channels.

5.4.4 Experimental Details.

To minimise random background arising from activities induced in the counter, and to eliminate pulses arising from the residual betatron output, which is coincident in time and therefore more prone to pile up, the multichannel analyser was gated to accept pulses only during the time when the full energy synchrotron output was produced. The gating pulse, timed from the mains, and the output from a scintillation counter which monitored the bremsstrahlung were displayed simultaneously on the screen of a double-beam oscilloscope, and the timing and width of the gating pulse adjusted to bracket comfortably the bremsstrahlung output. A schematic diagram of the electronics is given in Figure 5.6.

Proton spectra were taken for maximum bremsstrahlung energies ranging from 16 to 32 Mev at 2-Mev intervals. Individual runs were of two hours' duration, and between

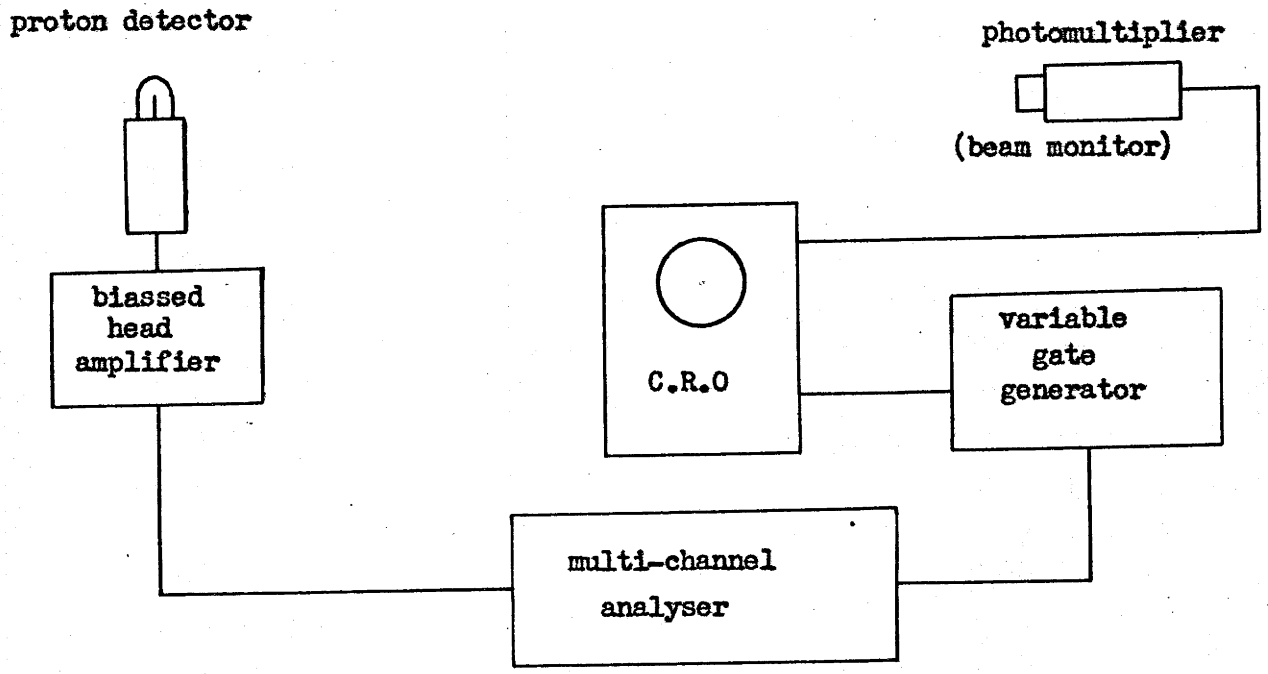

Figure 5.6 : Schematic Diagram of Electronic Circuit

runs the gain of the counter was checked by measuring the thorium alpha particle spectrum; it was found that the gain remained stable, though slight adjustment had to be made occasionally to the photomultiplier volts to correct for small drifts.

The total bremsstrahlung dose was monitored by the activity induced in tantalum foils. Foils were wrapped in cadmium and placed behind the counter in the position shown in Figure 5.3, and the 8.15-hour Ta^{180m} activity was measured by detecting the 55 Kev K-capture X-ray with a scintillation spectrometer. After each run the foils were left for an hour before the activity was measured to allow any 10-minute activity from Ta^{178} (see Carver and Turchinetz: C6) from the reaction Ta^{181} $(\gamma,3n)$ to decay away.

In order to achieve the highest possible count rates, the target was made as thick as possible, consistent with protons not being too severely degraded in energy within the foil itself. Since it was not anticipated that the spectra would exhibit any fine structure, a target which removed $\sim$ 1 Mev from a 10 Mev proton was considered satisfactory, and accordingly a foil thickness of 40 mg./sq.cm. was decided upon*. Even so, the fastest counting rates,

---

* It should be noted that the distributions are therefore

which were recorded when the machine was run at its top energy of 32 Mev, were still of the order of only two to three per minute for protons of energy greater than 8 Mev. At lower machine energies they were less, partly because lower points on the bremsstrahlung yield curve were being measured, but also because the output from the machine falls considerably as the end-point energy is reduced.

Thus, sufficient statistics to determine the yield curves adequately could only be accumulated over a number of runs, which were added together. The spectrum taken at a maximum bremsstrahlung energy of 30 Mev, for example, is the sum of five two-hour runs, and contains 1200 pulses corresponding to protons of energy greater than 8 Mev. The set of spectra shown in Figure 5.7, for which channels have been added together in groups of three, represent a total running time of about a hundred hours; they have been normalised to the same value of integrated electron current, but with an arbitrary scale factor, with the aid of the ^{181}Ta (γ,n) yield curve of Figure 4.8.

---

slightly distorted at the low energy end, since on average protons pass through about 20 mg./sq.cm. of silver before emerging from the foil. In this application the effect has little significance apart from raising proton energies slightly above their apparent values.

5.5 Absolute Yields.

The absolute yield of protons of energy greater than 8 Mev was determined relative to the known Cu^{63} (γ,n) cross section. A square foil of copper of the same dimensions as the silver target, and weighing 1.946 grammes, was placed in the target position and irradiated with 30 Mev bremsstrahlung for twenty minutes, with the same tantalum monitoring procedure.

Annihilation radiation from the 9.4-minute positron activity was detected in a known geometry with the sodium iodide scintillation counter, and the absolute neutron yield per mole of Cu^{63} per unit monitor activity calculated. This was related to the photoproton yield through the monitor activity and led to a value of the ratio:

$$\frac{Y(Ag_p)}{Y(Cu_n)} = \frac{\text{"Yield of photoprotons above 8 Mev per mole of Ag"}}{\text{Yield of photoneutrons per mole of Cu}}$$

$$= 0.066 \pm 0.02 \qquad \ldots.(5.5.1)$$

The method is not entirely free from objection, since the detection efficiency for both the proton counter and the scintillation counter had to be calculated from the respective geometries. The rather generous errors quoted include uncertainties arising from this source. In addition,

the photoproton yield may have been over-estimated, since it was assumed that protons were emitted isotropically; if the angular distribution were pure $\sin^2\theta$, this would mean that the yield had been over-estimated by a factor of two. However, the results of Diven and Almy (D4), using 20.8 Mev bremsstrahlung, indicate that most of the protons below 10 Mev are emitted isotropically, and this includes a fair proportion of all photoprotons above 8 Mev, so that the error introduced by assuming isotropy is probably not too serious.

So that the photoproton yield could be compared directly with the data of Diven and Almy, the ratio between the photoproton and photoneutron yields from silver at 21 Mev was also found. Silver and copper foils of the same dimensions and weighing respectively 22.9 mg. and 95.6 mg. were enclosed in cadmium and exposed to 21 Mev bremsstrahlung for ten minutes. The 24.5-minute (D5) and 9.4-minute positron activities from Ag^{106} and Cu^{62} were compared in the same geometry, using the scintillation counter, and corrected for isotopic abundance and decay schemes to determine the ratio between the respective (γ,n) yields.

The value obtained:

$$\frac{Y(Ag_n)}{Y(Cu_n)} = \frac{\text{"Yield of neutrons per mole of Ag"}}{\text{Yield of neutrons per mole of Cu}}$$

$$= 3.56 \pm 0.15 \qquad \ldots.(5.5.2)$$

is about 30 per cent higher than the figure of 2.80 reported by Diven and Almy for virtually the same bremsstrahlung energy.

The relative yield at 21 Mev of photoprotons above 8 Mev and photoneutrons from silver is determined from:

(i) the ratio $Y(Ag_p) / Y(Cu_n)$ at 30 Mev = 0.066 (expression 5.5.1)

(ii) the ratio $Y(Ag_n) / Y(Cu_n)$ at 21 Mev = 3.56 (expression 5.5.2)

(iii) the ratio between the respective photoproton yields at 21 and 30 Mev = 82/325 (from the photoproton yield curve: see Figure 5.8).

These combine to give a figure:

$$\frac{0.066}{3.56} \cdot \frac{82}{325} = 0.0054 \pm 0.0015$$

That is, there are 5.4 ± 1.5 protons of energy greater than 8 Mev for every thousand photoneutrons from silver

excited by 21 Mev bremsstrahlung. This result is to be compared with that given by Diven and Almy, who find approximately 8 ± 2 * protons of energy greater than 8 Mev per thousand photoneutrons. The discrepancy between these two values arises mainly from the difference between the two measurements of the silver photoneutron yields. Variations of this magnitude are not uncommon in absolute determinations of photonuclear yields; in this instance it is likely that the difference has come about through the use of different monitoring procedures.

5.6 Results and Analysis.

5.6.1 Photoproton Yield Curves.

The results obtained are summarised by the family of yield curves shown in Figure 5.8. These have been drawn for counter thresholds increasing in steps of 2 Mev from 8 Mev to 22 Mev. They have been normalised to the absolute determination at 30 Mev, and the scale is such that an iterative analysis using the tables of Appendix 1 yields directly the absolute cross section in millibarns.

The curves drawn for thresholds of 8, 10 and 12 Mev

---

* This was obtained from their "total photoproton yield per 10^3 neutrons" (23 ± 8) by determining from their published distribution the fraction of protons (~1/3) above 8 Mev.

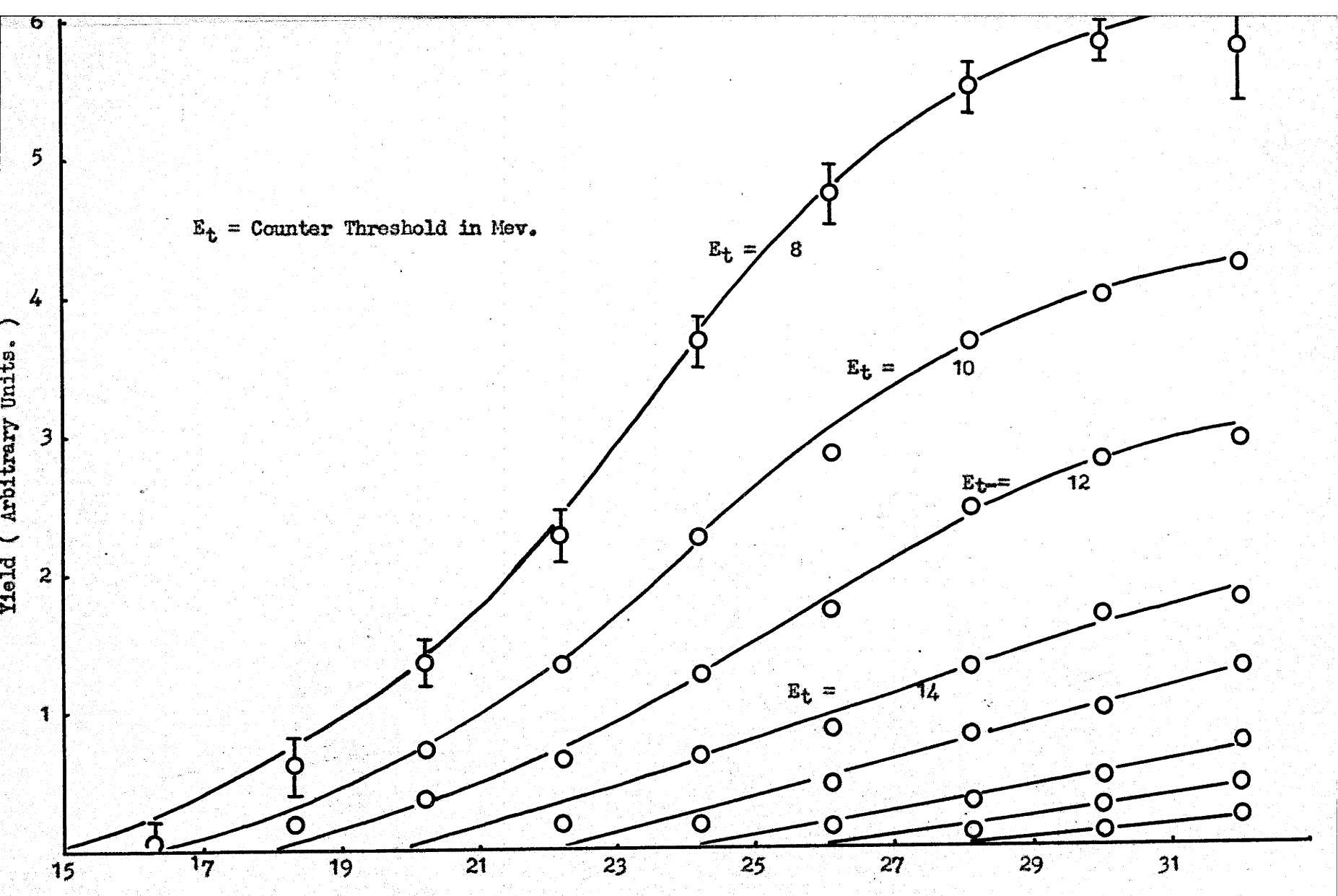

Figure 5.8 : Yield Curves

indicate a peak in the cross section for emission of protons of more than these energies in the region of 22 Mev. This is somewhat surprising, since the maximum of the giant resonance for neutrons occurs at 17 Mev (D4). Beyond these counter thresholds the inaccuracies of the points on the yield curves preclude any definite conclusions being drawn, though the typical inflected shape of the curves would be destroyed, as it appears to be, as the yield curve threshold approached and moved beyond 22 Mev.

The yield curve drawn for a counter threshold of 10 Mev has been analysed completely by the iterative method, and the derived cross section is plotted in Figure 5.9. The integrated cross section for the emission of protons of energy greater than 10 Mev is:

$$\int_{16}^{32} \sigma \, dE = 36 \pm 9 \text{ Mev millibarn.}$$

This value has been obtained assuming an isotropic angular distribution for the protons, and the errors quoted are derived only from the uncertainties in the measurements. It is therefore an upper limit for the integrated cross section, and may be in error by as much as a factor of two, depending on how great the anisotropy is.

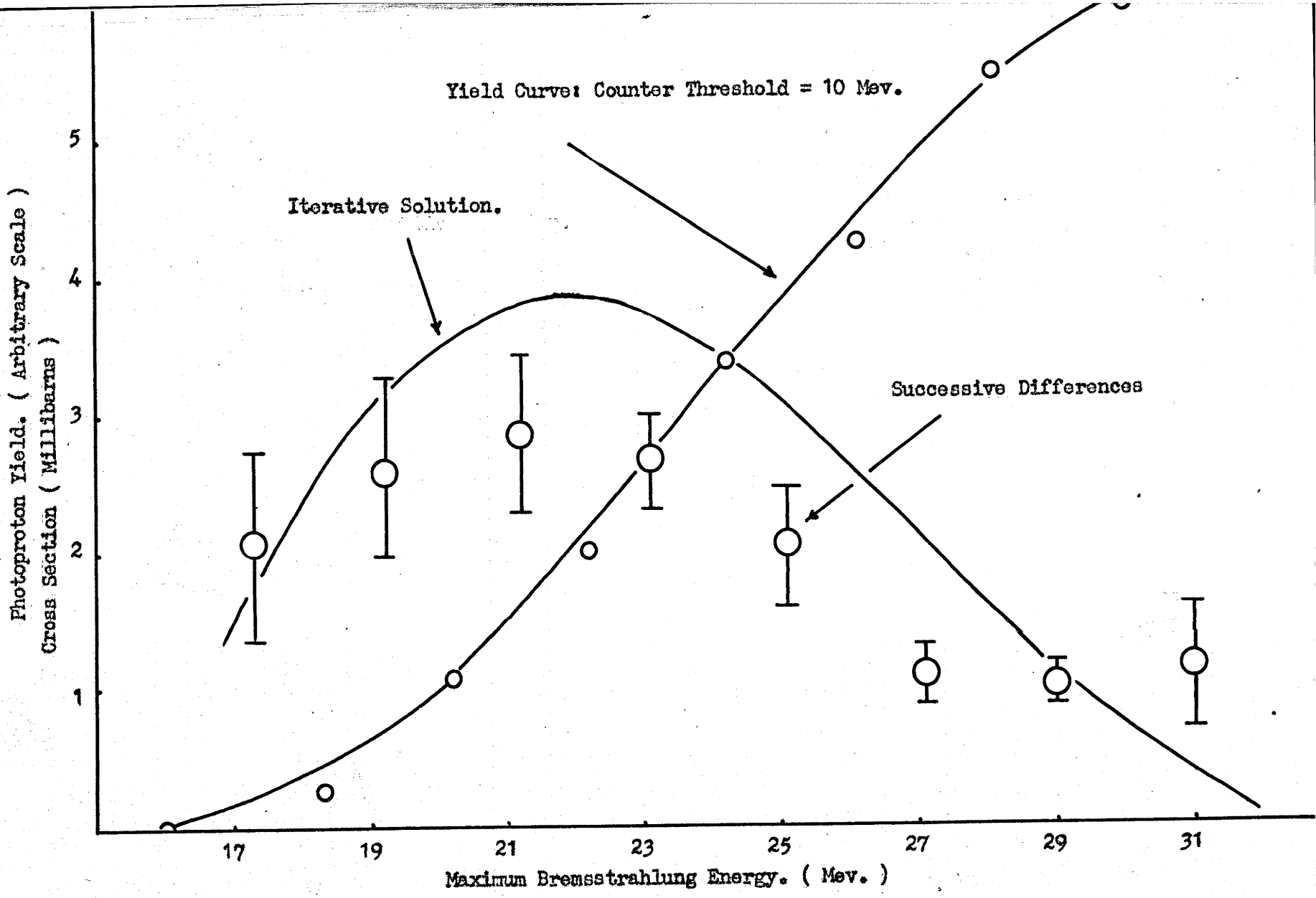

Figure 5.9 : Analysis of Yield Curve

5.6.2 Analysis of Spectra.

In principle, if one takes the difference between spectra recorded at successive bremsstrahlung energies, this difference will be the photoproton spectrum for a gamma-ray distribution which is itself the difference between successive bremsstrahlung spectra. If the interval is made fairly small, this will correspond to something approaching monochromatic radiation, since the smaller the interval the closer the difference will look to the derivative curves $P'(k,k_0)$ of Figure 2.1. Unfortunately, to make effective use of this means of analysis successive spectra would have to be determined extremely accurately, since it is the difference which would be significant, and this is scarcely feasible where total counting rates are of the order of only a few per minute.

Nevertheless, a simplified analysis can be applied in the following way. The proton spectra from 30 Mev and 28 Mev bremsstrahlung cut off at approximately 24 Mev and 22 Mev respectively. Those protons which have energies between these limits can have come only from interactions with gamma rays between 28 Mev and 30 Mev, and must, moreover, leave the residual nucleus close to its ground state. Since the number of photons in the tip of the bremsstrahlung spectrum

is known, an average cross section for these protons over the energy interval can be obtained directly.

This has been done with the measured spectra, and the average cross section obtained by taking successive differences is shown in Figure 5.9. The errors on the lower energy points are large, since the bremsstrahlung yield from the synchrotron falls off quite severely as its energy is lowered, but the curve shows the same general shape. The cross section rises as the photon energy is reduced from 32 Mev, and appears to pass through a peak in the region of 20 Mev; the integrated cross section from 16 to 32 Mev derived from this curve is 30 ± 10 Mev millibarn, close to the value obtained from the iterative analysis.

5.7 Discussion.

5.7.1 The Proton Evaporation Spectrum.

The distribution of "evaporated" protons following the absorption of a photon of given energy is given by the Maxwellian distribution of protons within the nucleus appropriate to the excitation energy, multiplied by the barrier penetrability. To determine the distribution expected following bremsstrahlung excitation, the spectrum corresponding to each photon energy within the bremsstrahlung distribution must be calculated. The set of these

spectra is then weighted according to the content of the bremsstrahlung beam and the absorption cross section, and summed over energy.

Figure 5.10 shows the result of such a calculation for bremsstrahlung of 30 Mev, assuming a barrier height of 9 Mev, a nuclear temperature of 1 Mev and an absorption cross section peaking at 17 Mev, and similar in shape to the (γ,n) giant resonance in silver. The calculation has been performed for s-wave protons only, for which there is no centrifugal barrier, and no allowance has been made for variation of nuclear temperature with excitation, since most of the absorption takes place over a fairly narrow range of photon energies. A value of 1.30×10^{-13} . $A^{1/3}$ was taken for the nuclear radius to determine the Coulomb penetrability (M7).

It is seen that the evaporation spectrum shows a peak at~6 Mev, and that beyond 10 Mev the proton yield is negligible. Moreover, it is not easy to alter these conclusions without taking rather extreme and somewhat unrealistic liberties with the nuclear parameters involved. (S5). Diven and Almy have calculated the distributions expected from 20.8 Mev bremsstrahlung for four sets of

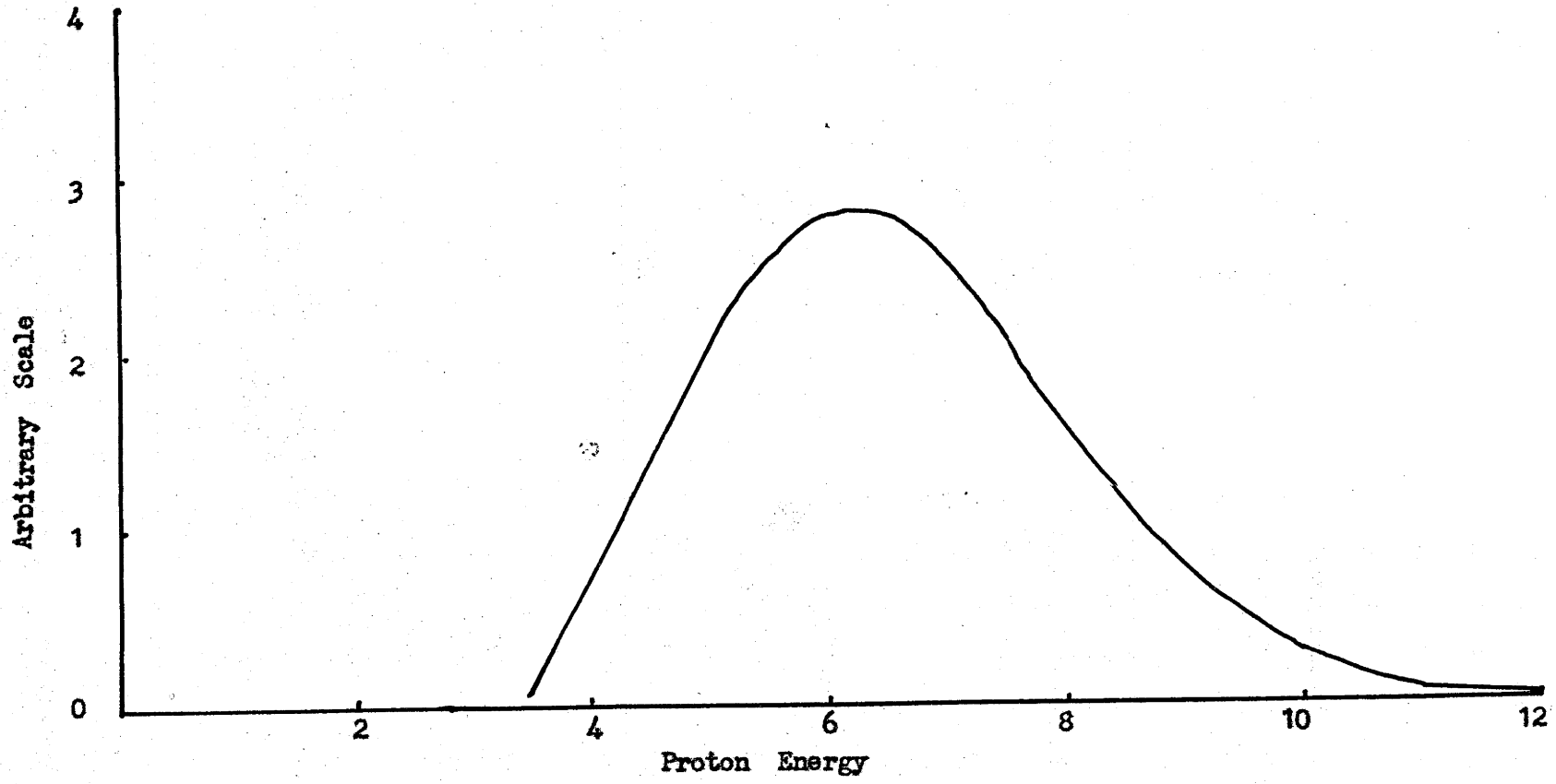

Figure 5.10 : Calculated Evaporation Spectrum

nuclear parameters*, and find reasonable agreement, both in shape and absolute magnitude, with their observed spectrum at low energies (less than 8 Mev) for values close to those assumed in the above calculation.

It is considered, therefore, that protons observed beyond 10 Mev are not evaporated from a compound nucleus, but arise from direct interactions. This conclusion is supported by the fact that the cross section for all protons of energy greater than 10 Mev (see Figure 5.9) agrees reasonably well with the "direct" cross section determined by successive subtraction of spectra. It is apparent that most of the increase in yield of protons above 10 Mev can be attributed to the extra protons emerging with approximately full energy when the bremsstrahlung end-point energy

---

* These were:

(i) θ = 1 Mev (i.e. level density $\sim \exp(aE)^{\frac{1}{2}}$, $a = A/5$)
$r_0 = 1.42 \cdot 10^{-13}$ cm.

(ii) θ = 1.3 Mev (i.e. level density $\sim \exp(aE)^{\frac{1}{2}}$, $a = 1.6(A - 40)^{\frac{1}{2}}$)
$r_0 = 1.30 \cdot 10^{-13}$ cm.

(iii) θ as in (ii)
$r_0 = 1.50 \cdot 10^{-13}$ cm.

(iv) assuming level density proposed by Schiff (S5), namely $\sim \ln(E + b) / b$, $b = 20/A$. This increases much more slowly with energy than the above.
$r_0 = 1.42 \cdot 10^{-13}$ cm.

is increased; over the energy range 16 to 32 Mev, then, the yield of protons above 10 Mev measures fairly well the direct photoproton cross section.

5.7.2 The Shell Model.

The striking feature of the experimental cross section is that it shows a maximum shifted upwards in energy by several Mev from the (γ,n) resonance, which peaks at 17 Mev. The second important feature is its absolute magnitude. The integrated cross section for the (γ,n) reaction in silver is 1650 Mev millibarn (D4) and the integrated cross section for direct photoprotons is 36 Mev millibarn (c.f. 5.6.1), so that 36/1650, or about 2 per cent, of the total absorption is accounted for by direct emission of protons. It is shown in this section that both of these results are in reasonable agreement with the shell model theory of photonuclear absorption proposed by Wilkinson (W5, W6).

In the shell model formulation the giant resonance is thought to arise from enhanced dipole transitions from closed shells (c.f. 1.4.2). In the silver nucleus most of the transition strength is found in the 1f - 1g proton transitions, and the $1f_{5/2}$ - $1g_{7/2}$ and $1g_{9/2}$ - $1h_{11/2}$ neutron transitions, the energies of which tend to cluster to produce the observed peak in the absorption at 17 Mev.

The important proton transitions, determined from the radial overlap integrals and angular wave function weighting factors listed by Wilkinson (W6) for an infinite square well, are presented in Table 5.1.

Table 5.1.

PROTON TRANSITIONS IN SILVER *.

Transition	Transition Strength	
$2p_{3/2} - 3s_{1/2}$	0.080	(3%)
$2p_{3/2} - 2d_{3/2}$	0.037	(14%)
$2p_{3/2} - 2d_{5/2}$	0.336	
$1f_{7/2} - 1g_{9/2}$	0.840	
$1f_{7/2} - 1g_{7/2}$	0.031	(78%)
$1f_{5/2} - 1g_{7/2}$	1.089	

These account for about 95 per cent of all proton transitions in silver.

* In Mayer-Jensen coupling the $2p_{1/2}$ shell is not filled until Z = 48, so that the nuclear configuration is $(1s_{1/2})^2 (1p_{3/2})^4 (1p_{1/2})^2 (1d_{5/2})^6 (2s_{1/2})^2 (1d_{3/2})^4 (1f_{7/2})^8 (2p_{3/2})^4 (1f_{5/2})^6 (2p_{1/2})^2 (1g_{9/2})^8$ (S2).

The direct yield of photoprotons may be estimated in the same way as the direct neutron yield from tantalum was estimated in the previous chapter (c.f. 4.7). The width for direct emission is again given by:

$$\Gamma \approx \frac{3}{2}\frac{\hbar^2 k}{mR} \cdot P_\ell = 7.6\, P_\ell \text{ Mev}$$

(for a 10 Mev proton)

but in this case P_ℓ, the penetrability through the barrier (Coulomb + centrifugal), is the dominant factor which may severely curtail emission from the 1f - 1g transitions, and increase the importance of transitions between shells of lower angular momentum. The calculation in this instance is much more uncertain, however, since the penetrabilities are very sensitive to the proton energies assumed.

The observed cross section peaks at ~ 22 Mev, and the experiment indicates that the energy of the protons emitted following absorption in this region is ~ 16 Mev. Accordingly, as a first estimate, the direct yield has been calculated assuming a proton energy of 16 Mev for each transition, setting limits of 4 Mev and 10 Mev on 2W, the width for absorption into a compound nucleus (c.f. 4.7)

and using penetrabilities given by Morrison (M7). The result is given in Table 5.2.

Table 5.2.

DIRECT YIELD OF PROTONS (E_p 16 MEV).

Transition	Strength	P_ℓ	Net Yield 2W = 4	Net Yield 2W = 10
1f - 1g	78%	.41	22%	18%
2p - 2d	14%	.8	8%	5%
2p - 3s	3%	1	2%	1%
Totals	95%		32%	24%

Thus, for these assumptions, direct proton emission accounts for 24% to 32% of the proton transitions, or 12% to 16% of the total absorption. This is much higher than the experimental yield of 2% of the total absorption, largely because of the contribution of the 1f - 1g transitions to the direct yield, and indicates, therefore, that the 1f - 1g transitions are not likely to be associated with the direct photoproton peak at 22 Mev.

It is, in fact, a more natural step to associate the 1f - 1g transitions, which are the strongest and account for about 40 per cent of the total photon absorption from closed shells*, with the giant resonance at 17 Mev, and the weaker 2p - 2d transitions with the 22 Mev peak. If this is done, and a proton energy of ~ 11 Mev is assumed,** the yield from the 1f - 1g transitions is reduced by a factor of twenty, and the calculated direct emission is 3% to 6% of the total absorption, depending on the value chosen for 2W; this agrees fairly well with the experimental value.

5.7.3 Comparison with the Reaction Mo^{100} (γ,p).

It is relevant to compare this experiment with a recent measurement by residual activation of the (γ,p) cross section in a nearby element Mo^{100} $(Z = 42)$. Ferrero

---

* This may not be strictly correct, since no allowance has been made in the calculation of transition strengths for the number of protons which are already in the shell to which the transition is made. It is possible in this case that the 1f - 1g transition strength is over-estimated, since part of it comes from the $1f_{7/2}$ - $1g_{9/2}$ transition, and the $1g_{9/2}$ shell already contains eight protons. This, of course, does not imply that the integrated cross section is less, since presumably transitions upwards from the almost filled $1g_{9/2}$ shell are correspondingly stronger. The direct proton yield from a 1g - 1h transition is negligible, however, since protons in the 1h shell must surmount an even higher barrier.

** This probably still over-estimates the yield from the 1f - 1g transitions, since the 1f shell almost certainly lies several Mev below the least bound shells.

et al (F3) have observed a peak in the total cross section at 22 Mev, and an integrated cross section of about 6 per cent of the total absorption. They have performed a somewhat similar analysis, determining the direct yield from each transition for an assumed proton energy of 10 Mev in each case, and a value of 2W = 10 Mev. On this basis they have found that the 1f - 1g and 2p - 2d transitions are both responsible for most of the proton yield, with the 1f - 1g the more important. Their calculated yield agrees with experiment, though they point out that the theoretical estimate depends critically on the energies and widths assumed.

5.8 Conclusions.

The initial aim of this experiment was to determine whether it is necessary to propose an independent absorption mechanism to account for direct photoproton emission. The experimental result that the cross section passes through a maximum several Mev above the photoneutron peak, and accounts for 2 per cent of the total absorption, has been shown to be consistent with individual proton transitions being excited between closed shells, and indicates further that the most important transitions are those between the 2p and 2d shells with an energy of 22 Mev.

CHAPTER 6.

THE ANGULAR DISTRIBUTION OF HIGH ENERGY PHOTOPROTONS FROM SILVER.

Abstract.

The angular distribution of fast photoprotons from silver has been measured for a maximum bremsstrahlung energy of 30 Mev and found to be strongly anisotropic. For comparison the same measurement has also been made for nickel, and the angular distribution confirmed to be isotropic.

It is concluded that the high energy protons from silver are emitted from shells of low angular momentum, in agreement with the conclusions of the previous chapter.

6.1 Introduction.

Irrespective of the detailed shape of the nuclear potential, the angular distribution of photoprotons depends only on their angular momentum before and after photon absorption. In general* (C9) they are proportional to:

(i) for a transition $l \rightarrow l+1$

$$l(l+1) + \tfrac{1}{2}(l+1)(l+2)\sin^2\theta$$

---

* These expressions assume no contribution to the absorption of higher multipolarity than E1.

(ii) for a transition $\ell \rightarrow \ell - 1$

$$\ell(\ell+1) + \tfrac{1}{2}\ell(\ell-1)\sin^2\theta$$

Thus the angular distributions are of the form $A + B\sin^2\theta$, where the ratio B/A is determined by the angular momentum of the protons involved; in certain circumstances, when the transitions are not too complex, they may help to identify the shells from which the protons emerge.

Accordingly, the thin crystal detector described in 5.2 was used to measure the angular distribution of high energy protons from silver, to decide whether the 1f - 1g transitions contribute significantly to the direct yield.

6.2 Experimental Details.

The crystal was mounted on a perspex light pipe as shown in Figure 6.1, through the lid of a circular chamber. The lid rested on an "O" ring and could be rotated with respect to the chamber to set the angle of the detector. Also supported by the lid was a perspex foil holder, which could be moved independently, so that the orientation of the foil target to the beam could be preserved as the angle of the detector was changed. The beam entered and left the chamber, which was evacuated, through extended tubes with thin aluminium ends, and was monitored with tantalum foils as in the previous experiment.

The chamber was shielded on all sides by 2 inches of lead, but the shielding was not as effective as in the previous experiment since the crystal itself was not closely surrounded with lead; this meant that the background edge was shifted upwards in energy, and only protons with energy greater than 13 Mev could be reliably identified. When this condition had been established, the multi-channel analyser was replaced by a single channel analyser and scalar, set to accept all pulses corresponding to proton energies above 13 Mev. In this case, since there was no gating facility on the single channel analyser, pulses were passed through a gated amplifier, with the gating conditions determined in the same way as for the previous experiment (c.f. 5.4.4).

6.3 Angular Distributions.

The proton yield at 30 Mev, normalised to unit monitor activity, was measured as a function of angle at intervals of 20°, since the angle subtended by the crystal at the centre of the target was just greater than this (22°).

6.3.1 The Angular Distribution from Silver.

Since the counter threshold was set so high, the counting rate from the silver foil was extremely low. To offset this, the target thickness was increased to 100 mg./sq.cm.,

a thickness for which the energy lost by a 13 Mev proton emitted from the centre of the foil is ~ 1 Mev. For all angles measured the foil was maintained parallel to the axis of the beam.

The measured angular distribution, which is markedly anisotropic, is shown in Figure 6.2. The errors shown are root mean square deviations determined from the statistics, and the horizontal bars indicate the angular resolution of the counter; no correction has been applied to the data for variations in energy loss within the target as a function of angle.

6.3.2 The Angular Distribution from Nickel.

The angular distribution of fast protons from nickel has been measured previously at 30 Mev by Leiken et al (L6) using photographic emulsions, and found to be almost isotropic. To make certain that the angular distribution for silver was not affected by some systematic error in the method, this measurement was repeated using a nickel target of thickness ~100 mg./sq.cm. The angular distribution found, which is fairly flat, and certainly greatly different from the distribution for silver, is shown in Figure 6.3.

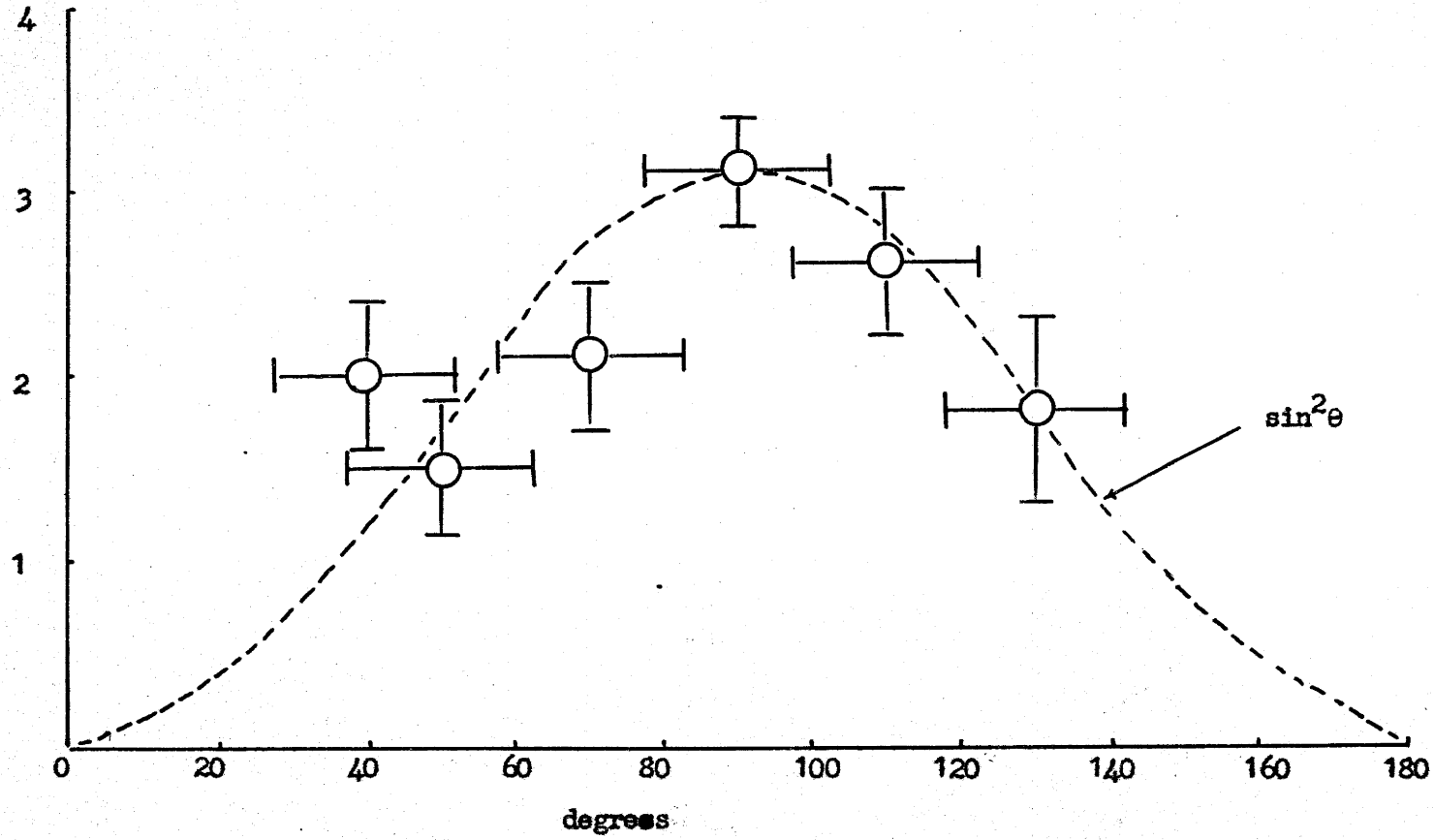

Figure 6.2 : Angular Distribution of protons from Silver

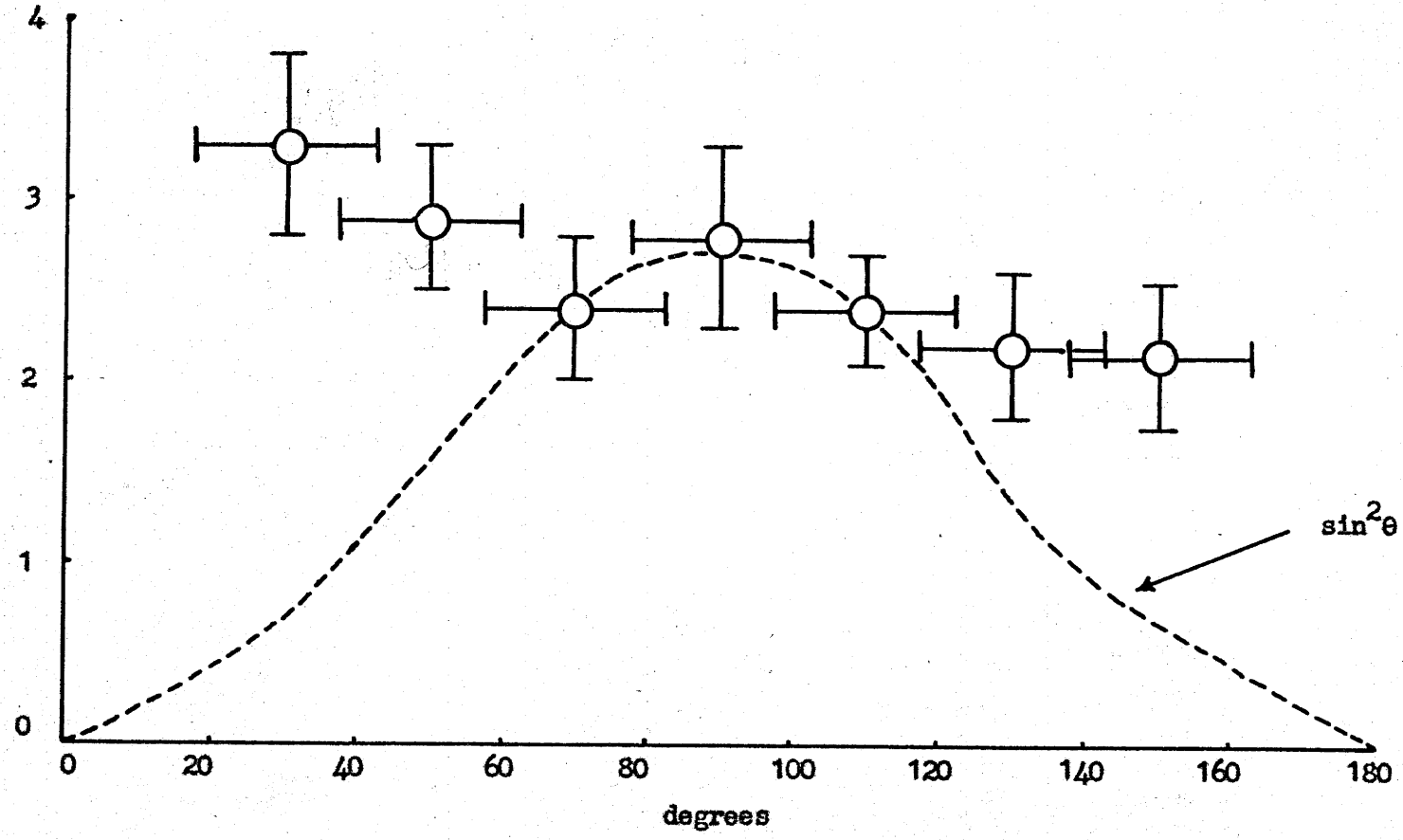

Figure 6.3 : Angular Distribution of protons from Nickel

6.4 Discussion.

In the previous chapter it was suggested that the main contribution to the yield of direct photoprotons > 10 Mev from silver comes from the 2p - 2d transitions. The angular distribution of protons from these transitions is proportional to $1 + 1.5\sin^2\theta$ (c.f. 6.1), whilst that from the 1f - 1g transitions is proportional to $1 + 0.83 \sin^2\theta$ and contains a much larger isotropic component.

The angular distribution found in this experiment appears to be even stronger than would be expected from the 2p - 2d transitions, though the errors on the points are comparatively large, and the distribution $1 + 1.5 \sin^2\theta$ is not excluded. One may certainly draw the conclusion, therefore, that the observed angular distribution of protons above 13 Mev is not consistent with their coming from the 1f - 1g transitions, in agreement with the conclusions of the previous chapter.

APPENDIX 1.

The Schiff spectrum $P(k,k_o)$, its derivative with respect to k_o, $P'(k,k_o)$, and the normalising function $S(k_o,T)$, used for the solution of bremsstrahlung yield curves, are tabulated at 1 Mev intervals of k, k_o and T from 6 to 35 Mev.

TABLE 1.

THEORETICAL SCHIFF BREMSSTRAHLUNG SPECTRUM: 100 x $P(k,k_o)$.

k_o Mev / k Mev	35	34	33	32	31	30
35	2.0					
34	7.6	2.0				
33	10.6	7.8	2.0			
32	12.6	11.0	8.0	2.0		
31	14.2	13.0	11.2	8.4	2.0	
30	15.2	14.6	13.6	11.6	8.6	2.2
29	16.6	16.0	15.2	14.0	12.0	9.0
28	17.8	17.2	16.6	15.8	14.4	12.4
27	19.0	18.6	18.0	17.2	16.2	15.0
26	19.8	19.6	19.2	18.6	18.0	17.0
25	21.0	20.8	20.4	20.0	19.4	18.4
24	22.2	21.8	21.6	21.2	20.8	20.2
23	23.4	23.2	23.0	22.6	22.2	21.8
22	25.0	24.8	24.4	24.0	23.6	23.4
21	26.6	26.4	26.0	25.8	25.2	25.0
20	28.2	28.0	27.8	27.6	27.2	26.8
19	30.2	30.0	29.8	29.4	29.0	28.6
18	32.4	32.2	32.0	31.6	31.4	30.8
17	35.0	34.6	34.4	34.2	33.8	33.2
16	38.2	37.8	37.4	36.8	36.6	36.2
15	41.2	41.0	40.8	40.4	39.8	39.4
14	45.2	44.8	44.4	44.4	43.6	43.2
13	50.0	49.6	48.8	48.4	48.0	47.6
12	55.4	55.0	54.6	54.2	53.8	53.0
11	61.6	61.2	60.8	60.0	59.6	59.2
10	69.4	69.0	68.4	68.0	67.4	67.0
9	79.4	78.8	77.8	77.8	77.2	76.6
8	91.2	90.6	90.6	90.0	89.2	88.6
7	107	106	106	106	105	104
6	128	128	127	127	126	125

Table 1 (continued).

k_o Mev / k Mev	29	28	27	26	25	24
29	2.2					
28	9.2	2.2				
27	13.0	9.6	2.4			
26	15.6	13.4	10.0	2.4		
25	17.8	16.2	14.0	10.4	2.6	
24	19.6	18.6	17.0	14.6	10.8	2.6
23	21.0	20.4	19.4	17.8	15.4	11.2
22	22.8	22.0	21.4	20.2	18.6	16.2
21	24.6	24.0	23.4	22.4	21.2	19.6
20	26.2	25.8	25.2	24.4	23.6	22.2
19	28.4	27.8	27.4	26.8	26.0	24.8
18	30.6	30.0	29.6	28.8	28.2	27.6
17	33.0	32.4	32.0	31.4	30.8	29.8
16	35.6	35.2	34.6	34.4	33.8	33.2
15	39.0	38.4	38.0	37.4	37.0	36.4
14	42.8	42.2	41.8	41.0	40.6	40.0
13	47.2	46.6	46.2	45.4	44.6	44.2
12	52.4	51.6	51.2	50.4	50.0	49.2
11	58.8	58.2	57.2	56.8	56.0	55.0
10	66.0	65.6	65.0	64.0	63.6	62.6
9	76.0	75.0	74.4	73.4	72.8	71.6
8	88.0	87.2	86.2	85.2	84.4	83.6
7	104	102	101	101	100	99.2
6	124	123	122	122	121	120

Table 1 (continued)

k_o Mev / k Mev	23	22	21	20	19	18
23	2.8					
22	11.8	2.8				
21	17.0	12.4	3.0			
20	20.4	17.8	13.0	3.2		
19	23.4	21.8	18.6	13.6	3.4	
18	26.2	25.0	23.0	19.6	14.4	3.6
17	29.2	27.8	26.2	23.6	20.6	15.2
16	32.2	31.2	29.6	28.2	26.0	22.2
15	35.8	34.4	33.6	32.0	30.0	27.8
14	39.2	38.2	37.2	36.0	34.2	32.4
13	43.6	42.6	41.6	40.4	39.2	37.2
12	48.4	47.6	46.8	45.4	44.2	42.4
11	54.6	53.2	52.4	51.4	50.0	48.8
10	61.6	61.0	59.6	58.6	57.6	56.0
9	71.0	70.0	68.8	67.2	66.0	64.8
8	82.6	81.8	80.6	79.2	77.4	76.2
7	98.6	97.0	95.8	94.2	93.0	91.2
6	118	117	116	114	112	111

k_o Mev / k Mev	17	16	15	14	13	12
17	3.8					
16	16.2	4.0				
15	23.8	17.4	4.2			
14	30.0	25.4	18.6	4.6		
13	35.4	32.2	27.2	20.0	5.0	
12	40.8	38.4	35.0	29.6	21.6	5.4
11	47.2	45.0	42.4	38.6	32.4	23.6
10	54.6	52.6	50.0	47.0	42.6	36.0
9	63.2	61.6	59.4	56.8	52.8	47.8
8	75.0	73.2	70.8	68.0	65.0	60.0
7	89.2	87.8	85.4	82.8	79.2	75.6
6	109	107	105	103	99.0	95.8

Table 1 (continued)

k_o Mev / k Mev	11	10	9	8	7	6
11	5.8					
10	26.0	6.4				
9	40.6	29.4	7.2			
8	54.4	46.4	33.2	8.0		
7	70.0	63.6	52.8	37.8	9.2	
6	90.8	85.0	75.0	62.4	44.2	11.0

TABLE 11.

THE SCHIFF BREMSSTRAHLUNG DISTRIBUTION, DIFFERENTIATED WITH RESPECT TO PEAK ENERGY: 100 x $P'(k,k_0)$.

k_0 Mev / k Mev	35	34	33	32	31	30
35	11.144					
34	3.742	11.468				
33	2.104	3.848	11.874			
32	1.366	2.172	3.966	12.194		
31	0.944	1.418	2.256	4.086	12.586	
30	0.682	0.978	1.462	2.330	4.216	12.998
29	0.512	0.706	1.018	1.528	2.408	4.354
28	0.400	0.532	0.738	1.052	1.578	2.488
27	0.332	0.422	0.558	0.766	1.096	1.634
26	0.290	0.352	0.448	0.582	0.806	1.142
25	0.266	0.308	0.378	0.476	0.710	0.836
24	0.258	0.282	0.330	0.402	0.498	0.642
23	0.254	0.278	0.306	0.356	0.428	0.522
22	0.260	0.280	0.304	0.336	0.392	0.452
21	0.270	0.284	0.304	0.332	0.366	0.416
20	0.282	0.294	0.310	0.332	0.360	0.398
19	0.296	0.308	0.322	0.340	0.362	0.392
18	0.314	0.326	0.338	0.354	0.374	0.394
17	0.332	0.344	0.358	0.372	0.388	0.406
16	0.352	0.362	0.380	0.394	0.412	0.430
15	0.372	0.384	0.402	0.420	0.436	0.456
14	0.394	0.408	0.426	0.450	0.460	0.486
13	0.416	0.430	0.450	0.470	0.488	0.514
12	0.438	0.456	0.476	0.496	0.518	0.542
11	0.460	0.480	0.502	0.526	0.550	0.576
10	0.484	0.504	0.528	0.554	0.582	0.610
9	0.504	0.528	0.554	0.584	0.610	0.646
8	0.530	0.554	0.584	0.616	0.646	0.682
7	0.554	0.582	0.610	0.646	0.680	0.718
6	0.576	0.608	0.640	0.676	0.714	0.754

Table 11 (continued).

k_o Mev / k Mev	29	28	27	26	25	24
29	13.452					
28	4.510	13.920				
27	2.586	4.678	14.438			
26	1.704	2.692	4.862	15.008		
25	1.192	1.784	2.816	5.060	15.598	
24	0.876	1.250	1.870	2.948	5.276	16.262
23	0.676	0.920	1.314	1.962	3.064	5.510
22	0.552	0.714	0.972	1.362	2.038	3.216
21	0.488	0.592	0.754	1.032	1.456	2.152
20	0.444	0.526	0.640	0.808	1.094	1.550
19	0.408	0.484	0.562	0.684	0.866	1.164
18	0.402	0.464	0.526	0.612	0.736	0.928
17	0.432	0.470	0.514	0.572	0.668	0.802
16	0.454	0.482	0.518	0.566	0.632	0.728
15	0.480	0.502	0.534	0.568	0.626	0.696
14	0.508	0.532	0.562	0.596	0.638	0.694
13	0.538	0.564	0.598	0.626	0.670	0.716
12	0.572	0.602	0.632	0.666	0.704	0.762
11	0.608	0.638	0.674	0.708	0.750	0.802
10	0.644	0.676	0.714	0.754	0.800	0.856
9	0.682	0.720	0.758	0.804	0.852	0.906
8	0.724	0.760	0.804	0.854	0.908	0.968
7	0.758	0.808	0.852	0.906	0.966	1.032
6	0.798	0.848	0.900	0.960	1.024	1.098

Table 11 (continued).

k_o Mev / k Mev	23	22	21	20	19	18
23	16.958					
22	5.766	17.742				
21	3.380	6.046	18.588			
20	2.280	3.560	6.360	19.522		
19	1.648	2.400	3.748	6.708	20.546	
18	1.250	1.756	2.556	3.976	7.090	21.700
17	1.006	1.242	1.876	2.724	4.238	7.456
16	0.878	1.100	1.448	2.012	2.922	4.526
15	0.802	0.968	1.196	1.594	2.174	3.162
14	0.776	0.896	1.056	1.322	1.736	2.384
13	0.782	0.880	0.994	1.192	1.466	1.920
12	0.826	0.890	0.984	1.130	1.332	1.638
11	0.876	0.952	1.006	1.126	1.276	1.504
10	0.934	0.990	1.070	1.160	1.292	1.440
9	0.974	1.060	1.126	1.224	1.344	1.514
8	1.048	1.116	1.208	1.292	1.422	1.580
7	1.106	1.186	1.280	1.394	1.522	1.666
6	1.178	1.268	1.370	1.486	1.620	1.844

k_o Mev / k Mev	17	16	15	14	13	12
17	22.972					
16	8.016	24.426				
15	4.858	8.576	26.048			
14	3.428	5.252	9.228	27.912		
13	2.600	3.764	5.724	9.988	30.074	
12	2.132	2.886	4.136	6.260	10.880	32.600
11	1.910	2.390	3.236	4.524	6.904	11.976
10	1.736	2.120	2.708	3.666	5.182	7.802
9	1.714	2.004	2.464	3.140	4.226	5.968
8	1.756	2.016	2.352	2.878	3.682	4.936
7	1.878	2.078	2.394	2.818	3.426	4.386
6	1.960	2.160	2.494	2.830	3.850	4.156

Table 11 (concluded).

k_0 Mev / k Mev	11	10	9	8	7	6
11	35.590					
10	13.292	39.182				
9	8.882	14.948	43.602			
8	6.972	10.300	17.140	49.148		
7	5.932	8.292	12.168	20.020	56.382	
6	5.356	7.200	10.200	14.884	24.140	66.104

TABLE 111.

THE FUNCTION $100\,S(k_o,T) = 100\left\{ P(k_o,k_o) + \int_T^{k_o} P'(k,k_o)\,dk \right\}$.

k_o Mev / T Mev	35	34	33	32	31	30
35	0.93					
34	7.29	0.96				
33	9.79	7.52	0.98			
32	11.8	10.1	7.74	1.02		
31	13.1	12.2	10.4	7.96	1.05	
30	14.0	13.5	12.6	10.7	8.21	1.08
29	14.7	14.5	14.0	12.9	11.0	8.48
28	15.2	15.2	14.9	14.4	13.4	11.4
27	15.6	15.7	15.7	15.4	14.9	13.8
26	15.9	16.1	16.2	16.2	15.9	15.3
25	16.2	16.4	16.6	16.7	16.8	16.5
24	16.5	16.7	17.0	17.2	17.3	17.2
23	16.7	17.0	17.3	17.6	17.8	17.9
22	17.0	17.3	17.6	17.9	18.2	18.4
21	17.2	17.6	18.0	18.3	18.6	18.9
20	17.5	17.9	18.3	18.6	19.0	19.2
19	17.8	18.2	18.6	19.0	19.3	19.7
18	18.1	18.5	18.9	19.2	19.7	20.0
17	18.4	18.8	19.2	19.7	20.1	20.5
16	18.7	19.2	19.6	20.0	20.5	20.8
15	19.1	19.5	20.0	20.4	20.9	21.3
14	19.5	19.9	20.4	20.8	21.3	21.7
13	19.9	20.3	20.8	21.3	21.8	22.3
12	20.3	20.8	21.3	21.8	22.3	22.7
11	20.7	21.2	21.8	22.3	22.8	23.3
10	21.2	21.7	22.3	22.8	23.4	23.8
9	21.7	22.2	22.8	23.4	23.9	24.5
8	22.2	22.7	23.3	24.0	24.6	25.1
7	22.7	23.3	23.9	24.6	25.2	25.9
6	23.3	23.9	24.6	25.2	25.9	26.6

Table 111 (continued)

k_o Mev / T Mev	29	28	27	26	25	24
29	1.11					
28	8.75	1.15				
27	11.7	9.15	1.20			
26	14.3	12.3	9.48	1.24		
25	15.9	14.9	12.8	9.84	1.29	
24	17.0	16.6	15.5	13.3	10.3	1.35
23	17.9	17.8	17.3	16.1	13.8	10.7
22	18.5	18.6	18.5	18.0	16.7	14.3
21	19.1	19.4	19.5	19.3	18.5	17.2
20	19.5	20.0	20.2	20.3	20.1	19.5
19	20.1	20.5	20.9	21.1	21.2	21.1
18	20.5	21.0	21.4	21.8	22.1	22.4
17	20.9	21.5	21.9	22.4	22.8	23.1
16	21.4	22.0	22.5	23.0	23.4	24.1
15	21.9	22.4	23.0	23.5	24.1	24.9
14	22.3	23.0	23.5	24.1	24.7	25.5
13	22.9	23.5	24.1	24.7	25.4	26.3
12	23.4	24.1	24.7	25.3	26.0	27.0
11	23.9	24.7	25.3	26.0	26.7	27.9
10	24.6	25.3	26.0	26.7	27.5	28.5
9	25.2	26.0	26.7	27.5	28.3	29.0
8	25.9	26.7	27.5	28.3	29.2	30.3
7	26.7	27.5	28.3	29.2	30.1	31.4
6	27.4	28.3	29.2	30.1	31.1	32.4

Table III (continued)

k_o Mev / T Mev	23	22	21	20	19	18
23	1.41					
22	11.1	1.47				
21	14.9	11.7	1.54			
20	18.2	15.6	12.2	1.62		
19	20.4	19.3	16.6	12.8	1.70	
18	22.3	21.4	20.2	17.4	13.6	1.80
17	23.3	23.5	22.7	21.3	18.4	14.3
16	24.6	24.5	24.5	23.8	22.6	19.2
15	25.2	26.0	26.0	25.9	25.3	23.9
14	26.3	26.7	27.1	27.3	27.5	26.7
13	26.9	27.9	28.2	28.8	29.2	30.0
12	27.9	28.5	29.1	29.8	30.7	30.9
11	28.5	29.7	30.2	31.1	31.9	32.8
10	29.9	30.4	31.2	32.1	33.3	34.0
9	30.3	31.7	32.3	33.4	34.5	35.8
8	31.5	32.4	33.4	34.5	36.0	37.1
7	32.3	33.9	34.7	35.9	37.3	38.9
6	33.7	34.8	35.9	37.2	38.9	40.4

k_o Mev / T Mev	17	16	15	14	13	12
17	1.91					
16	15.0	2.02				
15	20.5	16.1	2.16			
14	25.2	21.9	17.4	2.31		
13	28.6	27.2	23.5	18.4	2.49	
12	31.1	30.6	29.3	25.5	20.0	2.70
11	33.3	33.7	33.0	31.6	25.9	21.8
10	35.1	35.8	36.5	36.0	34.5	30.1
9	36.8	38.2	38.9	39.6	38.9	38.2
8	38.8	39.9	41.7	42.7	43.8	43.5
7	40.4	42.2	43.7	45.6	47.0	48.9
6	42.3	44.1	46.5	48.4	51.0	52.9

Table III (concluded).

k_o Mev / T Mev	11	10	9	8	7	6
11	2.94					
10	24.7	3.23				
9	32.5	26.2	3.60			
8	43.3	36.8	29.4	4.05		
7	48.1	47.6	43.6	33.1	4.53	
6	56.1	55.2	54.4	49.9	37.9	5.42

REFERENCES.

REFERENCES.

A1	Ajzenberg, F. and Lauritsen, T.	Rev. Mod. Phys. 27, 77, (1955)
B1	Baggett, L.M. and Bame, S.J.	Phys. Rev. 85, 434, (1952)
B2	Baker, R.G. and Katz, L.	Nucleonics 11, 14, (1953)
B3	Baldwin, G.C. and Klaiber, G.S.	Phys. Rev. 70, 289, (1946)
B4	Barber, W.C., George, W.D. and Reagan, D.D.	Phys. Rev. 98, 73, (1955)
B5	Berman, A.I. and Brown, K.L.	Phys. Rev. 96, 83, (1954)
B6	Bethe, H.A. and Maximon, L.C.	Phys. Rev. 93, 768, (1954)
B7	Bisi, A., Zappa, L. and Zimmer, E.	Nuovo Cimento 4, 307, (1956)
B8	Blatt, J.M. and Weisskopf, V.F.	"Theoretical Nuclear Physics", 1952. John Wiley & Sons, Inc.
B9	Brink, D.M.	Nuc. Phys. 4, 215, (1957)
B10	Burkhardt, G.	Phys. Rev. 91, 420L, (1953)
B11	Businaro, U.L. and Gallone, S.	Nuovo Cimento 1, 1285, (1955)
B12	Byerly, P.R. Jr. and Stephens, W.E.	Phys. Rev. 83, 54, (1951)

C1	Carver, J.H., Edge, R.D. and Lokan, K.H.	Proc. Phys. Soc. A70, 415, (1957)
C2	Carver, J.H., Edge, R.D. and Wilkinson, D.H.	Phil. Mag. 44, 404, (1953)
C3	Carver, J.H. and Hay, H.J.	Phil. Mag. 44, 1191L, (1953)
C4	Carver, J.H., Kondaiah, E. and McDaniel, B.D.	Phil. Mag. 45, 948, (1954)
C5	Carver, J.H. and Lokan, K.H.	Aust. J. Phys. 10, 312, (1957)
C6	Carver, J.H. and Turchinetz, W.E.	Proc. Phys. Soc., in the press
C7	Chadwick, J. and Goldhaber, M.	Nature 134, 237, (1934)
C8	Cohen, L., Mann, A.K., Patten, B.J., Reibel, K., Stephens, W.E. and Winhold, E.J.	Phys. Rev. 104, 108, (1956)
C9	Courant, E.D.	Phys. Rev. 82, 703, (1951)
C10	Curtis, N.W., Hornbostel, J., Lee, D.W. and Salant, E.O.	Phys. Rev. 77, 290L, (1950)
C11	Carver, J.H.	Reported at Nuclear Physics Conference, Canberra, 1958
C12	Carver, J.H. and Turchinetz, W.E.	Proc. Phys. Soc., in the press
C13	Cini, M. and Fubini, S.	Nuovo Cimento 2, 75, (1955)
C14	Cameron, A.G.W.	"A Revised Semi-empirical Atomic Mass Formula". Atomic Energy of Canada Ltd., Report No. A.E.C.L. 443.

D1	Danos, M.	Ann. d. Phys. 10, 265, (1952)
D2	Danos, M. and Steinwedel, H.	Z.f. Naturforschung, 6a, 217, (1951)
D3	Davies, H., Bethe, H.A. and Maximon, L.C.	Phys. Rev. 93, 788, (1954)
D4	Diven, B.C. and Almy, G.M.	Phys. Rev. 80, 407, (1950)
D5	Dzelepov, V.S. and Peker, L.K.	Atomic Energy of Canada Ltd., Report No. A.E.C.L. 457
E1	Edge, R.D.	Nuc. Phys. 2, 485, (1956)
F1	Ferguson, G.A., Halpern, J., Nathans, R. and Yergin, P.F.	Phys. Rev. 95, 776, (1954)
F2	Ferrero, F., Hanson, A.O., Malvano, R. and Tribuno, C.	Nuovo Cimento 4, 418, (1956)
F3	Ferrero, F., Hanson, A.O., Malvano, R. and Tribuno, C.	Nuovo Cimento 6, 585, (1957)
F4	Feshbach, H., Porter, C.E. and Weisskopf, V.F.	Phys. Rev. 96, 448, (1954)
F5	Fujita, J.	Prog. Theor. Phys. 16, 112, (1956)
F6	Fuller, E.G. and Hayward, E.	Phys. Rev. 101, 692, (1956)
G1	Gell-Mann, M., Goldberger, M.L. and Thirring, W.E.	Phys. Rev. 95, 1612, (1954)
G2	Goldemberg, J. and Katz, L.	Phys. Rev. 90, 308, (1953)

G3	Goldemberg, J. and Katz, L.	Phys. Rev. 95, 471, (1954)
G4	Goldhaber, G. and Teller, E.	Phys. Rev. 74, 1046, (1948)
G5	Goward, F.K., Titterton, E.W. and Wilkins, J.J.	Proc. Phys. Soc. A62, 460, (1949)
G6	Goward, F.K. and Wilkins, J.J.	Proc. Phys. Soc. A65, 671L, (1952)
G7	Goward, F.K. and Wilkins, J.J.	Proc. Roy. Soc. A217, 357, (1953)
G8	Guth, E. and Mullin, C.J.	Phys. Rev. 76, 234, (1949)
H1	Haslam, R.N.H., Johns, H.E. and Horsley, R.J.	Phys. Rev. 82, 270L, (1951)
H2	Haslam, R.N.H., Katz, L., Crosby, E.H., Summers-Gill, R.G. and Cameron, A.G.W.	Can. J. Phys. 31, 210, (1953)
H3	Heitler, W.	"The Quantum Theory of Radiation". 2nd. Ed. Oxford University Press. (1944)
H4	Hirzel, O. and Wäffler, H.	Helv. Phys. Acta. 20, 373, (1947)
H5	Hollander, J.M., Perlman, I. and Seaborg, G.T.	Rev. Mod. Phys. 25, 469, (1953)
H6	Horsley, R.J., Haslam, R.N.H. and Johns, H.E.	Can. J. Phys. 30, 159, (1952)
H7	Huber, O., Lienhard, O., Scherrer, P. and Wäffler, H.	Helv. Phys. Acta. 15, 312, (1942)
J1	Jensen, P.	Naturwiss 35, 190, (1948)

J2	Jensen, J.H.D. and Jensen, P.	Z.f. Naturforschung 5a, 343, (1950)
J3	Johns, H.E., Baker, R.G., Haslam, R.N.H. and Douglas, R.A.	Phys. Rev. 82, 271L, (1951)
J4	Johns, H.E., Katz, L., Douglas, R.A. and Haslam, R.N.H.	Phys. Rev. 80, 1062, (1950)
J5	Jones, L.W. and Terwilliger, K.W.	Phys. Rev. 91, 699, (1953)
K1	Katz, L., Baker, R.G. and Montalbetti, R.	Can. J. Phys. 31, 250, (1953)
K2	Katz, L. and Cameron, A.G.W.	Can. J. Phys. 29, 518, (1951)
K3	Katz, L., Haslam, R.N.H., Horsley, R.J., Cameron, A.G.W. and Montalbetti, R.	Phys. Rev. 95, 464, (1954)
K4	Katz, L., Johns, H.E., Baker, R.G., Haslam, R.N.H. and Douglas, R.A.	Phys. Rev. 82, 271L, (1951)
K5	Katz, L., Pease, L. and Moody, H.	Can. J. Phys. 30, 476, (1952)
K6	King, A.M. and Voigt, A.F.	Phys. Rev. 105, 1310, (1956)
K7	Koch, H.W. and Carter, R.E.	Phys. Rev. 77, 165, (1950)
K8	Koch, H.W.	Proc. 1954 Glasgow Conf. 155, (1955)
L1	Levinger, J.S.	Phys. Rev. 84, 43, (1951)
L2	Levinger, J.S.	Phys. Rev. 97, 122, (1955)

L3	Levinger, J.S.	Rev. Mex. Fis. 5, 177, (1956)
L4	Levinger, J.S. and Bethe, H.A.	Phys. Rev. 78, 115, (1950)
L5	Levinger, J.S. and Bethe, H.A.	Phys. Rev. 85, 577, (1952)
L6	Leiken, S., Osokina, R.M. and Ratner, B.S.	Supp. Nuovo Cimento 3, 105, (1956)
M1	Macklin, R.L. and Banta, H.E.	Phys. Rev. 95, 302A, (1954)
M2	Mann, A.K. and Halpern, J.	Phys. Rev. 82, 733, (1951)
M3	Mann, A.K., Halpern, J. and Rothman, M.	Phys. Rev. 87, 147, (1952)
M4	Maximon, L.C. and Bethe, H.A.	Phys. Rev. 87, 156L, (1952)
M5	Montalbetti, R. and Katz, L.	Can. J. Phys. 31, 798, (1953)
M6	Montalbetti, R., Katz, L. and Goldemberg, J.	Phys. Rev. 91, 659, (1953)
M7	Morrison, P.	"Experimental Nuclear Physics", Vol. 2, p. 193. Edited by E. Seyre. (1953) John Wiley & Sons, Inc.
M8	Myers, H., Odian, A., Stein, P.C. and Wattenberg, A.	Phys. Rev. 95, 576L, (1954)
N1	Nathans, R. and Halpern, J.	Phys. Rev. 92, 207L, (1953)
N2	Nathans, R. and Halpern, J.	Phys. Rev. 93, 437, (1954)
N3	Nathans, R. and Halpern, J.	Phys. Rev. 92, 940, (1953)

O1	Osokina, R.M. and Ratner, B.S.	J. Expt. Theor. Phys. (USSR) 32, 20, (1957). (American translation)
P1	Peaslee, D.C.	Phys. Rev. 88, 812, (1952)
P2	Penfold, A.S. and Spicer, B.M.	Phys. Rev. 100, 1377, (1955)
P3	Price, G.A.	Phys. Rev. 93, 1279, (1954)
R1	Range-Energy Tables	U.C.R.L. Report (Aron, W.A., Hoffmann, B.G. and Williams, F.C.)
S1	de Sabbata, V. and Sugie, A.	Nuovo Cimento 3, 16, (1956)
S2	Sachs, R.G.	"Nuclear Theory". Addison-Wesley Publishing Coy Inc. (1953)
S3	Sagane, R.	Phys. Rev. 84, 586L, (1951)
S4	Sagane, R.	Phys. Rev. 84, 587L, (1951)
S5	Schiff, L.I.	Phys. Rev. 73, 1311, (1948)
S6	Schiff, L.I.	Phys. Rev. 83, 252, (1951)
S7	Siegbahn, K.	"Beta- and Gamma-Ray Spectroscopy". North Holland Publishing Company, 1955.
S8	Snell, A.H., Barker, E.C. and Sternberger, R.L.	Phys. Rev. 80, 637, (1950)
S9	Steinwedel, H. and Jensen, J.H.D.	Z.f. Naturforschung, 5a, 413, (1950)

S10	Szilard, L. and Chalmers, T.A.	Nature 134, 494, (1934)
T1	Titterton, E.W.	Private communication
T2	Titterton, E.W. and Brinkley, T.A.	Proc. Phys. Soc. A66, 194L, (1953)
T3	Titterton, E.W. and Brinkley, T.A.	Proc. Phys. Soc. A67, 469, (1954)
T4	Tomonaga, S.	Prog. Theor. Phys. 13, 467, (1955)
W1	Weinstock, E.V. and Halpern, J.	Phys. Rev. 100, 1293, (1955)
W2	Weisskopf, V.F.	Nuc, Phys. 3, 423, (1957)
W3	Whaling, W. and Bonner, T.W.	Phys. Rev. 79, 258, (1950)
W4	White, F.A., Collins, T.L. and Rourke, F.M.	Phys. Rev. 97, 566, (1955)
W5	Wilkinson, D.H.	Proc. 1954 Glasgow Conf. 161, (1955)
W6	Wilkinson, D.H.	Physica 22, 1039, (1956)
W7	Wilkinson, D.H. and Carver, J.H.	Phys. Rev. 83, 466L, (1951)
W8	Wilkinson, G.	Phys. Rev. 80, 495, (1950)
W9	Wilson, R.	Proc. Phys. Soc. A66, 638, (1953)
W10	Wilson, R.	Proc. Phys. Soc. A66, 645, (1953)
W11	Wright, I.F.	Private communication

W12 Wright, I.F. and Ophel, T.R. Proc. Phys. Soc. in the press

Y1 Yergin, P.F. and Fabricand, B.P. Phys. Rev. 104, 1334, (1956)

Z1 Zatzepina, G.N., Lazareva, L.E. and Postelov, A.N. J. Expt. Theor. Phys. (USSR) 32, 27, (1957)